Ultra-wideband Synthetic Aperture Radar Imaging: Theory and Applications

by

Daniel Oloumi

A thesis submitted in partial fulfillment of the requirements for the degree of

Doctor of Philosophy
in
Electromagnetics and Microwaves

Department of Electrical and Computer Engineering
University of Alberta

Abstract

Ultra wideband (UWB)- synthetic aperture radars are emerging devices that are ideal for sensing and imaging applications in many special conditions such as monitoring subsurfaces, through-wall imaging, non-destructive characterization of materials, oil reservoir monitoring, weather forecasting, geo mapping, microwave holography for tissue imaging, and breast tomography to identify tumors. The exceptional characteristics of UWB radars, including high spatial resolution, low probability of interfering with other radio frequency (RF) signals, low power spectral density and compact size make them suitable for numerous applications. Moreover, their low power consumption allows them to operate on batteries, lending them to portable applications.

Oil reservoir monitoring using UWB radar is a new trend in the oil and gas industry for reservoir management and improving production. Monitoring perforations' conditions in metal or concrete-cased oil wells can provide valuable information for oil well maintenance and process optimization. Moreover, observing steam chamber growth in a heavy oil reservoir using radar technology will provide feedback to control steam flow to enhance oil extraction in the steam assisted gravity drainage (SAGD) process.

Radar imaging is a developing imaging modality for biomedical applications to study functional and pathological conditions of soft tissue. Radar imaging offers a safe, portable, cost-effective and near real-time imaging supplement for the non-invasive assessment of acute and chronic soft tissue conditions. Microwave imaging may turn out to be a simple and efficient method to perform breast imaging capable of providing adequate image resolutions for diagnosis.

This thesis focused on the applications of UWB-synthetic aperture radar (SAR) systems for oil reservoir monitoring and breast tumor imaging; both applications share a requirement for high image resolution. The theory part investigates the design procedure for UWB-SAR systems with specific range and cross-range resolutions. The effect of the pulse shape,

bandwidth, integration angle, and signal-to-noise ratio (SNR) of the received pulse on the image resolution is comprehensively studied. To enhance the image resolution, pre-processing of the received pulses with envelope detection is proposed. Superluminal phenomenon and UWB pulse propagation in the near-field of an antenna is studied. The apparent superluminal pulse velocity is due to the pulse reshaping of the radiated pulse in the near-field of the antenna. The effect of pulse velocity on the quality of reconstructed images is demonstrated.

The application part looks at the suitability of UWB-SAR for oil reservoir monitoring, such as perforation imaging in concrete- and metal-cased oil wells and steam chamber monitoring in heavy oil reservoir. High-quality images are reconstructed using a combination of UWB radar and SAR processing along with the proposed algorithms to improve image quality. The investigation includes positive image generation to enhance image sharpness, and near-field imaging procedure. Practical considerations for SAGD process monitoring such as power budget and heterogeneity analysis of a heavy oil reservoir using UWB radar are studied.

The application of UWB-circular synthetic aperture radar (CSAR) for breast tumor imaging is also demonstrated. Tomographic image reconstruction was carried out using a time domain global back projection technique adapted to circular trajectory data acquisition. The suitability of this technique for breast tumor detection and imaging is demonstrated through experiments on a 3D printed breast phantom, developed based on a human breast MRI, which emulates the breast in terms of structures and their electrical properties. The measurement results demonstrated the utility of UWB-CSAR for breast tumor imaging.

Preface

This thesis is an original work by Daniel Oloumi.

Chapter 2 is published as:

D.Oloumi, Jui-wen Ting, K.Rambabu,"Design of pulse characteristics for near-field UWB-SAR imaging," IEEE Trans. on Microwave Theory and Techniques. vol.64, no.8, pp.2684-2693, Aug. 2016.

Chapter 3 is published as:

D.Oloumi, K.Rambabu,"Studying the superluminal behavior of UWB antennas and its effect on near-field imaging," IEEE Trans. on Antennas and Propagations, (Accepted with minor revision), ID: AP1510-1634.R2.

Chapter 4 is published as:

D.Oloumi, M.I. Pettersson, P. Mousavi, K.Rambabu," Imaging of oil-well perforations using UWB synthetic aperture radar," IEEE Trans. on Geoscience and Remote Sensing, (TGRS), vol.53, no.8, pp.4510-4520, Aug. 2015.

Chapter 5 is published as:

D.Oloumi, K.Rambabu," Metal-cased oil well perforation detection using UWB radar techniques," submitted to IEEE Trans. on Geoscience and Remote Sensing, (TGRS), ID:TGRS-2016-00933,(Suitable for publication, revision submitted).

Chapter 6 is published as:

D.Oloumi, K-M.Chan, P.Boulanger, K.Rambabu,"SAGD process monitoring of heavy oil reservoir using radar techniques,"IEEE Trans. on Microwave Theory and Techniques, vol. 64, no. 6, pp. 1884-1895, June 2016.

Chapter 7 is published as:

D.Oloumi, A. Kordzadeh, P.Boulanger, K.Rambabu,“ Breast tumor detection using UWB circular-SAR microwave tomographic imaging ,“ submitted to IEEE Trans. on Microwave Theory and Techniques. TMTT-2016-09-1058,(Suitable for publication, revision submitted).

D.Oloumi , P.Boulanger, A. Kordzadeh, K.Rambabu ,“ Breast tumour detection using UWB circular-SAR tomographic microwave imaging,” 37th Annual International Conference of the IEEE Engineering in Medicine and Biology Society (EMBC), Milan, 2015, pp. 7063-7066. (*Selected as finalist paper*)

D.Oloumi, P.Boulanger, K.Rambabu,“ Tracking a biopsy needle inside a breast using UWB circular-SAR,“ IEEE International Symposium on Antennas and Propagation and USNC/URSI National Radio Science Meeting, Vancouver, BC, 2015, pp. 534-535.

I rendered help from the co-authors either in theoretical discussions and or for the measurements.

Dedicated to My beloved Family

Earn as much education as you can: it's wealth that nobody can steal from you

My grandmother, Tahereh, advice to me

RIP

Acknowledgements

First of all, I would like to thank God for the opportunity to achieve one of my most important goals. It was a long journey with many peaks and valleys, however I was very fortunate to have the support and encouragement of those I would like to thank and acknowledge herby.

I would like to extend my gratitude to my Ph.D. supervisor, Prof. Rambabu Karumudi. His limitless support, insight, immense knowledge, and mentorship played a significant role in my success. The timely completion of my thesis would not have been possible without his support and inspiration. In addition to academic support, he has always encouraged me through tough moments, for which I am forever grateful.

I would like to express my honest thanks to my lovely wife, Atefeh, who stayed beside me throughout this journey in all its ups and downs. Unquestionably, without her love and support, this accomplishment would be very difficult if not impossible.

I would like to give my sincere thanks to my parents Maryam and Amir for the continued love and care that they have provided me throughout my life. I also would like to thank my siblings Elahe and Benjamin and along with the rest of my family and friends for their precious support.

I would like to thank my Ph.D. committee members and examiners, Prof. Pierre Boulanger, Prof. Robert Fedosejevs, Prof. Vien Van, and Prof. Mahta Moghadam for insightful comments and encouragement.

I would like to thank my wrestling coach, Owen Dawkins, who inspired me to get on the mat again as well as my teammates for the priceless moments and experiences that we shared over the last few years as varsity athletes representing the University of Alberta.

I would like to thanks, Prof. Hojjat Kashani, my undergraduate supervisor, who inspired me in this field of study.

Thinking of my grandparents and my mother in law, who could not join me on this day, but would have loved to, you're in my heart forever.

Finally, I would like to acknowledge the financial support provided by Killam, Alberta Innovates Technology Future, IEEE Microwave Theory and Techniques, Andrew Stewart Prize as well as Natural Sciences and Engineering Research Council (NSERC) of Canada.

Contents

List of Figures

List of Tables

List of Acronyms

ACS American Cancer Society

ABS acrylonitrile butadiene styrene

CT Computed tomography

CSAR circular synthetic aperture radar

DARPA defense advanced research projects agency

2D two dimensional

3D three dimensional

EM electromagnetic

FCC Federal Communications Commission

FFT fast Fourier transform

FWHM full width at half maximum

GBP global back projection

GPR ground penetrating radar

IFFT inverse fast Fourier transform

IFN impulse forming network

IMF image magnification factor

LSAR linear synthetic aperture radar

MRI Magnetic resonance imaging

NF noise figure

PRF pulse repetition frequency

Radar Radio detection and ranging

RCS radar cross section

RF radio frequency

Rx receiver

SAGD steam assisted gravity drainage

SAR synthetic aperture radar

SNR signal-to-noise ratio

TEM transverse electromagnetic

TRx transceiver

Tx transmitter

UWB Ultra wideband

VNA vector network analyzer

Chapter 1

Introduction to UWB-Synthetic Aperture Radar

1.1 Motivation

UWB-SAR systems have provided a broad range of solutions for applications demanding high resolution. These applications range from geoscience and remote sensing to biomedical usages. A UWB-SAR system is formed by a radar operating on a large fractional bandwidth and synthesized apertures generated by moving the antenna to realize a big aperture. High resolution in the range and cross-range directions is provided using short electromagnetic (EM) pulses, corresponding to a UWB frequency spectrum, and synthesizing the apertures, respectively.

One of the most popular applications of the UWB-SAR is imaging. Unlike other sensor systems, radars demonstrate the ability to work in harsh conditions such as rain, clouds, darkness and also within opaque materials such as concrete, soil and mud, crude oil or even the human body, where light does not exist or cannot penetrate. Operating in the aforementioned conditions is a major advantage of UWB-SAR, particularly for applications such as breast cancer screening or oil well perforation detection and other imaging which is

in demand for high resolution images.

Oil reservoir management control techniques have helped the oil and gas industry to improve the production and maintenance of existing oil reservoirs. Radars have recently been introduced as a monitoring method for oil reservoirs [4]. On the medical side, the demand for a cheap, comfortable and safe breast screening method with decent image quality has been increasing as well. Radar imaging has been proposed for breast cancer screening as a potential future method [5]. Therefore, this thesis is focused on the oil reservoir monitoring and breast cancer imaging using UWB-SAR.

In this thesis, the theory and application of UWB-SAR systems is studied. In the theory part, first I studied the design procedure for a UWB-SAR system to provide a specific range and cross-range resolutions. Since most of the discussed applications require the radar to be very close to the target for effective imaging, I also investigated the UWB pulse propagation in the near-field of a radar. The result of this study is very important for accurate image reconstruction in the near-field of a UWB-SAR system.

In the application part, the suitability of UWB-SAR for oil reservoir monitoring is studied, in particular for perforation imaging in concrete- and metal-cased oil wells and steam chamber monitoring in the SAGD process. Moreover, I developed a UWB-CSAR algorithm and adapted it for breast tumor imaging. In all the above four cases the UWB-SAR could successfully provide quality images and information to be used by field engineers for management and decision-making, and by physicians for treatment planning.

1.2 Radar Systems and UWB Definition

This section provides a brief introduction on radar and its applications. It also covers the definition of UWB radar and its advantages.

(a) (b)

Figure 1.1: (a) Bat echolocation, (b) radar detection.

1.2.1 Radar

The basic idea of radar is taken from nature. Bats use their mouths to create sound and process the reflections of nearby objects to find their way and hunt in the dark. This is called bat echolocation and is shown in Fig.1.1(a). Radio detection and ranging (Radar) is a technique which uses RF signals to detect a target and estimate its distance to the radar. Detection occurs once the reflection/s is received by the radar Rx. The distance is measured in terms of speed of light in the medium of propagation and round-trip time. A radar system is formed by a transmitter to transmit a RF signal and one or more receiver/s to capture the reflections from the target/s. Mono-static radars use a single antenna for both transmission and reception operations. However, bi-static radar uses two separated antennas as Tx and Rx. In cases where the Tx and Rx antennas are located very close to each other, or bundled together, the radar configuration is called quasi-mono-static.

Research on radar development began in World War II for military purposes. Military applications have remained the most important function of radar systems [6]. In addition to military usage, radar systems have found a wide range of other applications [7], such as earth mapping [8] ,civil engineering [9], medicine, [10], weather forecasting [11], and airplane navigation [12]. Basically, radar systems now play vital roles in a variety of aspects of human

lives.

1.2.2 UWB radars

Radar range resolution is defined as the ability to resolve targets in the range direction. Radar range resolution is inversely proportional to pulse bandwidth [6]. Therefore, to achieve higher resolution and resolve close targets, more bandwidth is required. However, there is always a trade-off between radar resolution and target range, as losses increase with frequency.

UWB radars are able to provide high resolution by operating over a wide frequency bandwidth. According to defense advanced research projects agency (DARPA) 1990 [13], a radar is called UWB if it operates on a fractional bandwidth greater than 25%. The fractional bandwidth is defined as:

$$BW_{Frac} = \frac{2(f_h - f_l)}{f_h + f_l} \tag{1.1}$$

Where f_h and f_l are the highest and lowest frequency components of the signal spectrum. By this definition, any signal with fractional bandwidth more than 25 % is a UWB signal. Nowadays, the advancement of electronic and RF technology allows UWB radar systems to operate even over a couple of octave bandwidths [14].

UWB radar operation is governed by the radar range equation given by [15]. UWB radar range depends on various factors. To achieve an optimal performance in a particular medium and for a particular target, the radar has to be tailored to the application with specified characteristics such as antenna type, transmitter power, and system noise floor.

Unique characteristics of UWB radars, including high spatial resolution, low probability of interfering with other RF signals, low power spectral density and compact size with low power requirement, made them suitable for plenty of applications such as detecting trapped victims in complex environments [16], target characterization [17], non-destructive imaging [18], automotive vehicle control [19], and the monitoring of vital signs [10,20]. Because UWB

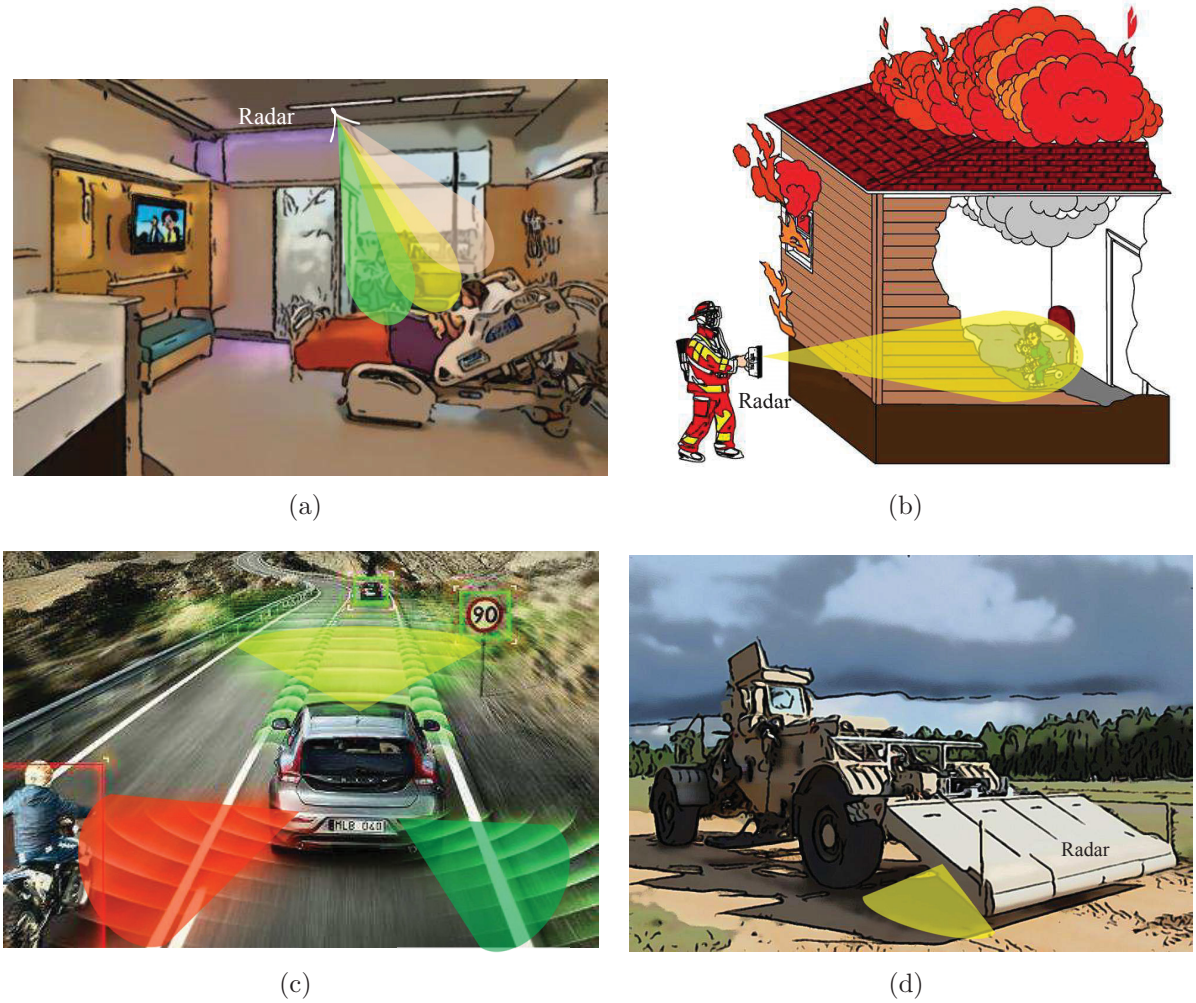

(a) (b)

(c) (d)

Figure 1.2: UWB radar applications for; (a) vital sign monitoring (original photo is taken from www.pinterest.com), (b) through wall radar for human detection [1], (c) anti-collision vehicular system (image is taken from Volvo website), (d) ground penetrating radar as a Mobile Countermine (original photo by Chemring NIITEK).

radar systems have low power consumption, they can operate on batteries [21]. This lends them to portable applications as well [22]. Fig. 1.2 demonstrates UWB radar applications for vital-sign monitoring, life detection in a complex medium, preventing collisions and ground penetrating radar (GPR) detecting mines. UWB radar systems regulations in terms of power level and frequency band are governed by the Federal Communications Commission (FCC) [23].

1.3 SAR Processing

Cross-range resolution is the minimum resolvable distance a radar needs to distinguish two targets at the same range [6]. In particular, two targets at the same range can be resolved only if they are not in the beam of the radar at the same time. This requires a high directive antenna with a big aperture [24]. In general, UWB antennas are not high gain. In this research, cross-range resolution is enhanced by moving the radar and synthesizing the apertures to build up a bigger aperture [25].

Fig. 1.3(a)-1.3(b) demonstrate the SAR data collection in both linear and circular approaches. At each antenna position, radar illuminates the target/s by transmitting RF signals. The radio waves impinge on the target and reflections are received by the radar Rx. Since the target is scanned from different positions, the RF signal experiences different time delays. Figs.1.3(c)- 1.3(d) illustrate the received pulses, generated using Matlab, for two point targets located at (7.5 cm, 0.15 cm) and (22.5 cm, 0.15 cm) for linear synthetic aperture radar (LSAR), and at (-7.5 cm,0 cm) and (7.5 cm, 0 cm) for CSAR. In these two examples, the raw data is generated using the second derivative Gaussian pulse with $10GHz$ of bandwidth from 1 to $11GHz$ as the transmitted wave. The two hyperbolas that appeared in 1.3(c) are the targets' signatures, which show different time delays at each aperture position. However, the time delay profile of CSAR is similar to the shape of a sinus function and therefore is known as a sinogram [26]. The raw data has to be processed to refocus the spread energy over the aperture to obtain higher cross-range resolution.

1.3.1 Time domain global back projection technique

The collected raw data is processed to obtain the image of a target in a spatial domain with higher cross-range resolution. In this research, SAR processing is performed using a time domain technique known as global back projection (GBP) [27, 28], which is best suited for time domain pulses. The GBP is a coherent summation of pulses received at different

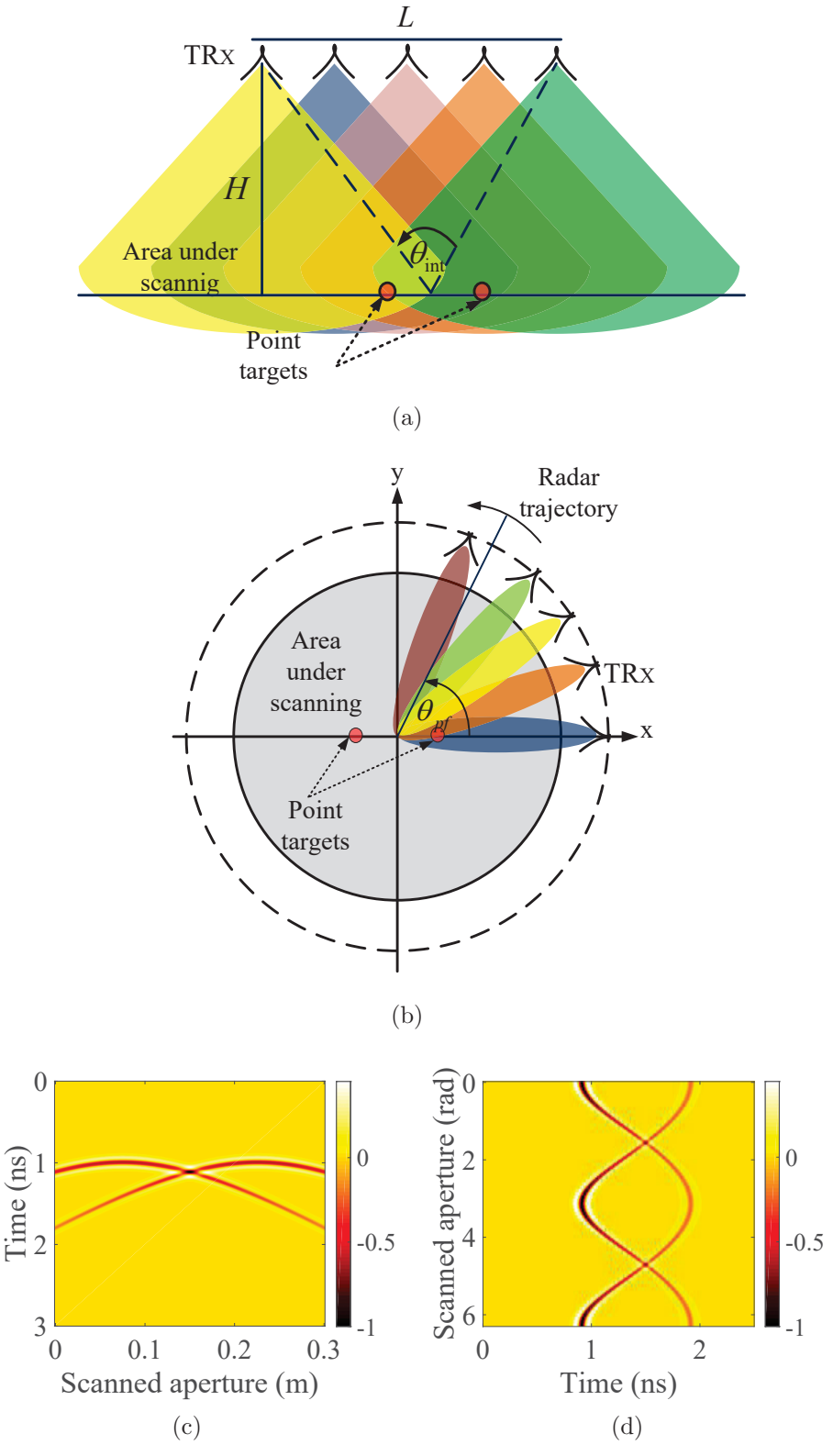

Figure 1.3: Synthetic aperture radar realization; (a) linear-SAR, (b) circular-SAR.

aperture positions in each pixel of the reconstructed image. Coherent summation at each pixel is developed by adding up the pulse's samples received from different aperture positions and combining that with the corresponding time delay to the radar antenna's position.

For data processing, the pulses are stored in a matrix the size of Nx_{data} and Nr_{data}, which are the number of aperture positions and time samples, respectively. Here two dimensional (2D) images are reconstructed. However, 3D images can also be reconstructed using the same method [29]. A 2D image is reconstructed with $M \times N$ number of pixels. To reconstruct an image using GBP, each image pixel is filled with appropriate samples. The appropriate data sample in time, which is related to the pulse round-trip time between each aperture position and image pixel, is found using the following calculations. First, the round trip distance is calculated by:

$$R(M,N) = \sqrt{(X_{pf1} - X_M)^2 + (Y_{pf1} - Y_M)^2 + (Z_{pf1} - Z_M)^2} + \sqrt{(X_{pf2} - X_M)^2 + (Y_{pf2} - Y_M)^2 + (Z_{pf2} - Z_M)^2} \tag{1.2}$$

where X_{pf}, Y_{pf}, Z_{pf} and V_s are the positions of the Tx and Rx antennas, and the signal speed considered for SAR processing, respectively. In the case of mono-static radar X_{pf}, Y_{pf}, Z_{pf} are the same for the transmitter and receiver. X_M, Y_M ,and Z_N are the pixel's location in the reconstructed image. The round-trip time, $t(M,N)$, is found by dividing the round trip distance, $R(M,N)$, by the signal speed, V_s, as shown in Eq. 1.3:

$$t(M,N) = \frac{R(M,N)}{V_s} \tag{1.3}$$

For SAR processing the signal speed is considered to be the same as the speed of light in the medium of propagation. Dividing the round-trip time by Δt, which is the time resolution,

gives the index of the appropriate time sample:

$$index(M,N) = round(\frac{t(M,N)}{\Delta t}) \tag{1.4}$$

The precise sample corresponding to each image pixel is picked using the nearest neighbor method [30]. As shown in Eq. 1.4, a larger sample population results in a smaller time resolution, Δt, increasing the probability of selecting the more accurate sample when the number is rounded to obtain the time index. Moreover, using more samples can result in smoother images and higher quality. If there is an insufficient number of samples, interpolation methods can be applied [29]. The image is rebuilt through:

$$I(M,N) = \sum_{n=0}^{l} [rawdata(l, index)] \tag{1.5}$$

in which, I is the reconstructed SAR image and l is aperture position.

1.3.2 LSAR image reconstruction

Using equations of the GBP, both LSAR, and CSAR or any arbitrary measurement path can be realized. If the radar moves in a straight line, the LSAR is realized. The radar path for LSAR is defined as:

$$\begin{aligned} X_{pf} &= 0 : L_s : L \\ Y_{pf} &= 0 \\ Z_{pf} &= h \end{aligned} \tag{1.6}$$

Where L is aperture length, L_s is the measurement steps and h is the altitude of the radar. To achieve higher cross-range resolution, a longer aperture length or wider integration angle is required. The effects of aperture length on cross-range resolution of a UWB-SAR are explained in detail in Chapter. 2.

This sub-section includes the reconstructed image of point targets shown in Fig. 1.3(c).

The raw data is in the space and time domains, corresponding to the horizontal and vertical axises, respectively. The point target signature appears in a hyperbolic shape. The peak of each hyperbola is the shortest range to the point target and also the horizontal location of the target. The width of the hyperbola is the same as the length of the radar aperture. The image of targets is reconstructed using both received pulses and their envelopes. The pulse envelope is generated using a Hilbert transform [31].

Reconstructed images are shown in Fig. 1.4. The spread energy over the hyperbola is focused to the target location with some bow-shaped artifacts around the targets due to a back projection process which can be reduced by generating positive images as explained later in this chapter. The reconstructed image using the envelope, shown in Fig. 1.4(d) , of the raw data can provide higher resolution even though it is blurred compared to Fig. 1.4(a), as discussed in the next chapter.

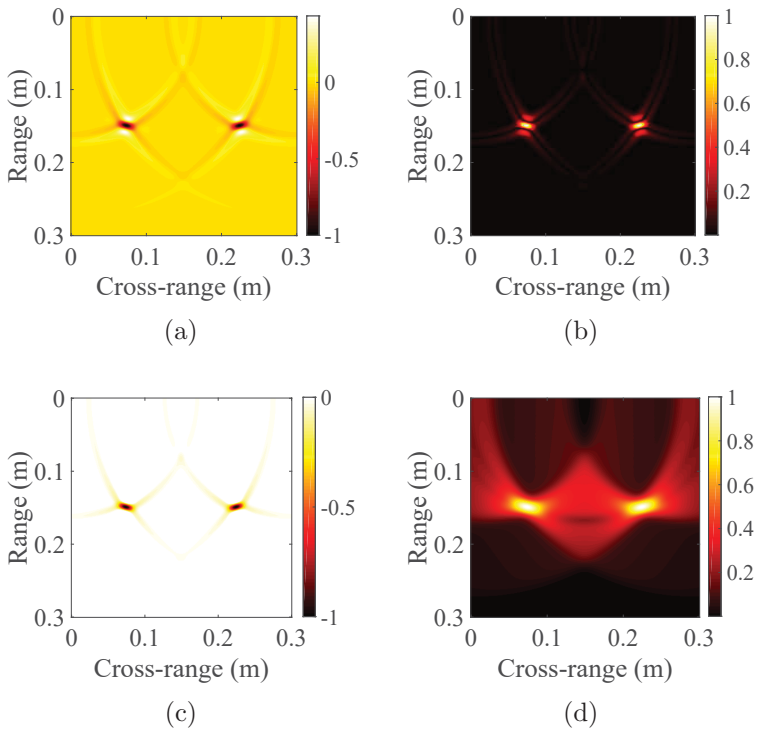

Figure 1.4: Reconstructed LSAR images: (a) real, (b) absolute, (c) positive, (d) envelope

1.3.3 CSAR image reconstruction

The CSAR measurement path is shown in Fig. 1.3(b). To collect the raw data the radar transceiver (TRx) goes around the target, and at each angle transmits a pulse and receives the reflections [32]. The radar path can be defined as:

$$\begin{aligned} X_{pf} &= r\ cos(\theta) \\ Y_{pf} &= r\ sin(\theta) \\ Z_{pf} &= h \end{aligned} \tag{1.7}$$

In which r is the radius of the radar measurement circle and θ is the angle. The range and cross-ranges resolutions are the same for CSAR as the target is scanned from all angles from 0 to 2π and the resolution only depends on the pulse bandwidth. In other words, CSAR does not introduce the bow-shape artifacts as the aperture is a circle. The bow-shape artifact at each angle cancels the other one at the opposite angle, resulting in an image with

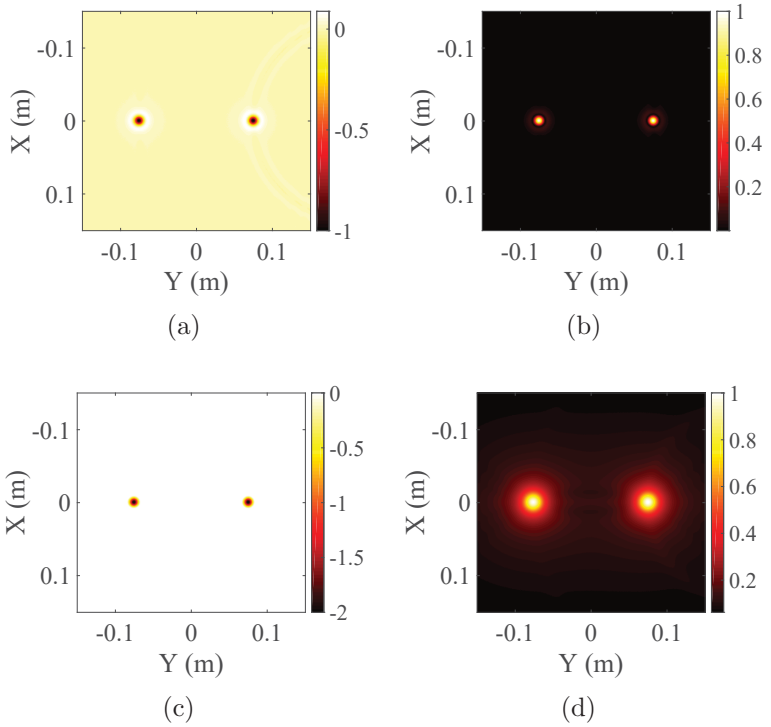

Figure 1.5: Reconstructed CSAR images: (a) real, (b) absolute, (c) positive, (d) envelope

higher clarity and quality. The reconstructed images are shown in Fig. 1.5(a)-1.5(d). The images are reconstructed inside the scanned area, or the measurement circle. As can be seen, a higher cross-range resolution is achieved by the CSAR. Moreover, the bow-shape effects, which appeared in LSAR, do not appear in the CSAR images.

1.3.4 Post processing of reconstructed images

A further post-processing can enhance the quality of the reconstructed image and extract more information. To remove the bow-shape artifacts and improve the image sharpness, a positive image can be generated. The positive image is generated by summing up or subtracting the absolute and real value of a reconstructed image depending on the polarity of the peak of the received pulse.

The positive image is explained in detail in Chapter. 4. The positive images are shown in Fig. 1.4(c) and Fig. 1.5(c). As can be seen, all the bow-shape artifacts in Fig. 1.4(a) are removed. Generating the positive image also cleared up the CSAR image, resulting in more vivid images. The envelope image might provide more information about the targets. The effect of envelope detection is explained in Chapter. 3.

1.3.5 UWB radar configuration

Since radar imaging and remote sensing are the main focus of this research, a lab UWB radar setup was developed to conduct the measurements. The measurement setup contains a UWB radar system and designed antennas customized for a specified applications.

A schematic of a generic UWB radar is shown in Fig. 1.6(a). A UWB radar TRx contains a UWB Tx and Rx units. The TRx unit contains a pulse generator, impulse forming network (IFN) and Tx and Rx antennas. The assembled radar system is shown in Fig. 1.6(b). The pulse generator, AVTECH $AVP-3SA-C$, generates a train of $10V-50ps$ rise-time steps at $1MHz$ pulse repetition frequency. The center frequency of the pulse is $6.5GHz$ with a $-10dB$ bandwidth of $10GHz$. The picosecond rise-time step is shaped into the first

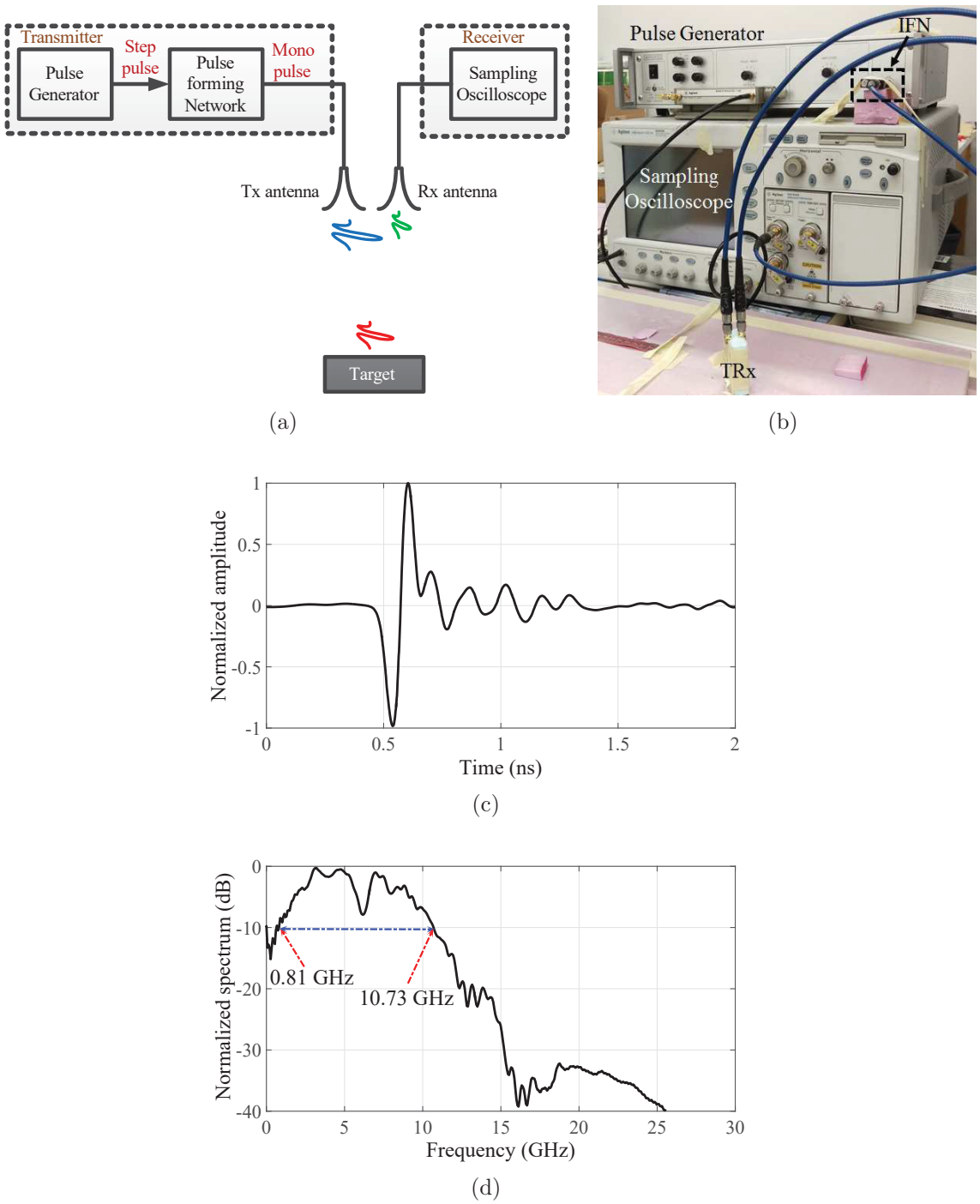

Figure 1.6: (a) UWB radar system schematic, (b) measurement setup, (c) generated Gaussian pulse, (d) Gaussian pulse spectrum.

derivative Gaussian pulse, or a mono-pulse, using two series-connected IFNs. The generated pulse with its frequency spectrum is shown in Fig. 1.6(c)-1.6(d). The UWB radar receiver consists of a Rx antenna and an Agilent DCA 86100B sampling oscilloscope which samples

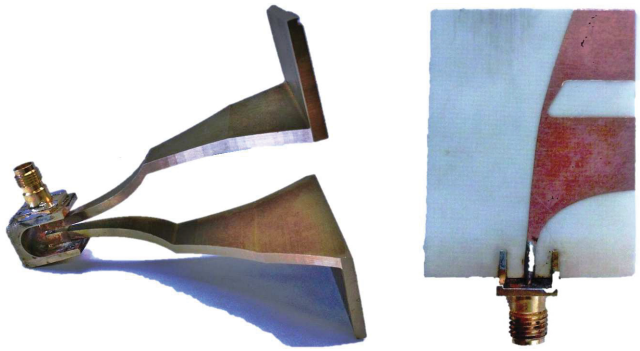

(a) (b)

Figure 1.7: (a) TEM horn antenna, (b) Vivaldi Antenna.

the signal at the rate of $40GS/s$.

UWB radar systems require UWB antenna/s for transmitting and receiving EM pulses. To conduct imaging in an oil well and an oil sand reservoir, and for breast tumor imaging, two customized UWB antennas capable of radiating pulses with a low level of distortion are designed. The antennas are a transverse electromagnetic (TEM) horn [33, 34] and a Vivaldi [35], which are shown in Fig. 1.7(a)-1.7(b), respectively. These antennas are designed to operate in oil mediums such as crude oil and oilsand for oil reservoir monitoring applications, and in vegetable oil for breast tumor imaging. These functions are detailed in Chapters. 4-7.

1.4 Pulse Calibration and Conditioning

Radar detects target/s by illuminating the area of interest by EM pulses and collecting the scattered pulses to acquire target/s characteristics. In a real case scenario, the received pulse is affected by the antennas' transfer functions in both Tx and Rx modes, mutual coupling between the antennas and scattering from the target and nearby objects. For instance, the input pulse is time-differentiated by the Tx antenna while transmitting [36]. In order to extract the target signature, other effects have to be eliminated from the received pulse. The

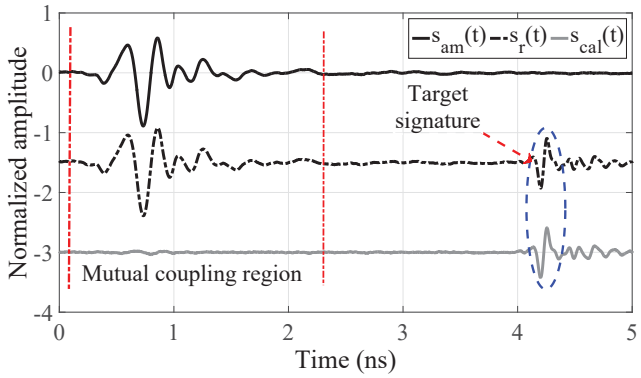

Figure 1.8: Calibration process of the received pulse.

received pulse can be mathematically modeled as follows:

$$s_r(t) = \overbrace{s_t(t) \otimes h_{med}(t) \otimes h_{Tx}(t) \otimes h_{Rx}(t)} + \overbrace{s_t(t) \otimes h_{med}(t) \otimes h_{Tx}(t) \otimes h_{Rx}(t) \otimes h_{tgt}(t)} \quad (1.8)$$

In which $s_r(t)$ and $s_t(t)$ are the Rx and Tx pulses. $h_{tgt}(t)$, $h_{Rx}(t)$, $h_{Tx}(t)$ and $h_{med}(t)$ are the target impulse response, the antenna impulse responses in Rx and Tx modes, and the medium impulse response, respectively. The $\otimes$ represents the convolution operator in the time domain. The first part of Eq. 1.8 is the antenna's mutual coupling in the medium of propagation, which can be unbounded or bounded regions filled with air, oil or any other materials. The second part of the equation is the target signature. To obtain the target signature and calibrate the pulse, $s_{cal}(t)$, the ambient pulse, $s_{am}(t)$, has to be removed as follows:

$$s_{cal}(t) = s_r(t) - s_{am}(t) \quad (1.9)$$

The ambient pulse is the effect of everything, including measurement instruments and surrounding objects, but the target/s. Fig. 1.8 demonstrates the calibration process of a received pulse reflected by a metal plate. These pulses are acquired by the radar experimental setup to detect a piece of metal plate placed in front of the radar transceiver. For illustration purposes, the pulses shown in Fig. 1.8 are offset along the vertical axis. In this case, the ambient pulse is measured by transmitting and receiving a pulse into the air as the medium

of propagation, in the absence of the metal plate. The received pulse and antenna mutual coupling resemble each other up to $2.3ns$. The calibrated pulse only contains the reflected pulse from the metal plate. The raw data collected by radar has to be calibrated before any future signal processing for either detection or image reconstructions.

1.5 The Contributions of this Thesis

This thesis has contributed to the state of the art in the field of UWB-SAR systems in both theory and practice, which is summarized as follows.

In **chapter 2:**

The design of pulse characteristics to achieve the desired image resolution for near-field synthetic aperture radar is presented. Gaussian and chirp pulses, which are the most commonly used pulses for UWB radar applications, were considered in this study. The effect of the pulse shape, bandwidth, integration angle, and SNR of the received pulse on the image resolution was comprehensively studied. To enhance the image resolution, pre-processing of the received pulses with envelope detection or match filtering were also studied. The range and cross-range resolutions achieved by Gaussian and chirp pulses with the same center frequency and bandwidth at various SNR values were compared. This study showed that the Gaussian pulse with envelope detection provides better image resolution, whereas the chirp pulse with match filtering provides more resistance to noise. Closed form equations and design guidelines were developed to enable the input pulse characteristics to achieve the desired image resolution. The antennas' effect on UWB pulses and the developed equation for cross-range resolution are both validated using full-wave simulations and measurements.

In **chapter 3:**

The superluminal behavior of a radiated pulse in the near-field of an ideal dipole and a

UWB antenna is explained and demonstrated through simulations and measurements. The deformation of the radiated pulse in the near-field was also illustrated. The apparent superluminal pulse velocity is due to the pulse reshaping of the radiated pulse in the near-field of an antenna. The superluminal pulse peak velocity of the radiated pulse from a miniaturized Vivaldi antenna was confirmed through measurements in face-to-face and quasi-mono-static radar configurations. The pulse velocity was measured by tracking the pulse peak, pulse envelope peak and also by calculating the pulse centrovelocity. The effect of different values of pulse velocities on the quality of reconstructed images using synthetic aperture radar processing was also demonstrated.

In **chapter 4:**

UWB-SAR as a tool for concrete-cased oil well perforation monitoring is experimentally investigated. Experiments were conducted on a lab prototype that emulated the small section of a concrete-cased oil well. The oil well perforations were scanned using the designed UWB radar system for different experimental conditions. High-resolution images in both the down-range and cross-range were obtained using UWB pulses and post-processing of the raw data. High-quality images were constructed using a SAR processing algorithm along with some proposed modifications. The experiments were carried out for different perforation conditions such as open, partially clogged and fully clogged cases. The experiments showed that the proposed radar technique and the data processing methods are capable of providing more revealing high-quality images. This approach can be applied effectively to monitor a concrete-cased oil well and detect well impairment locations.

In **chapter 5:**

Monitoring of metal-cased oil wells using UWB radar is proposed. The inspection should include the detection and imaging of perforations and the corroded area in a metal pipe. Detecting small anomalies/perforations on the surface of a narrow metal pipe is very chal-

lenging. Here we presented a method for imaging such small anomalies based on the extra time-delay of the reflected pulse, a delay that occurred due to the perforation in the radar near-field. In this work, the necessary concepts for using UWB radar specified for this application were developed based on different measurement and simulation scenarios. The effect of the perforations' size on the time-delay of reflected pulses was experimentally demonstrated. The distance between the perforation and the radar, particularly for the near-field phenomenon, is critical to achieve effective detection and imaging. Therefore, in this chapter, we also studied the optimal distance between the radar and the perforation. Perforations with size diversity of $1cm$ to $3cm$ were considered for the experiments and simulations. The experiments were done both in air and diesel. SAR processing was used to reconstruct the images of the perforations and corroded area. Measurement and simulation results demonstrate the potential of UWB radar systems for metal-cased oil well monitoring applications.

In **chapter 6:**

Practical considerations for SAGD process monitoring using UWB radar are studied. The SAGD process and important factors to monitor its performance were discussed. Several experiments were conducted to evaluate the possibility of using UWB radar for SAGD process monitoring. All the experiments were carried out on a simplified lab prototype, which was a plateau of wet sand covered by dry sand to mimic the steamed area of a heavy oil reservoir. The effect of metal pipe on the pulse shape and propagation inside the reservoir was also experimentally studied. Additionally, a miniaturized Vivaldi antenna capable of radiating within oil-sand was designed, fabricated and verified as a sensor for the radar monitoring system. Power budget and heterogeneity analysis of a heavy reservoir for different grades of Athabasca oil sands were also studied. The results supported the possibility of using UWB radar to detect and image the contour of the steamed area in the SAGD process. The information collected by the UWB radar can be used to optimize steam injection to improve the use of water and energy.

In **chapter 7:**

The suitability of UWB-CSAR as an early diagnosis tool to detect breast tumors is explored. CSAR is a subset of synthetic aperture radar, which uses a circular data acquisition configuration. Tomographic image reconstruction was done using a time domain global back projection technique adapted to circular trajectory data acquisition. The suitability of this technique for breast tumor detection and imaging was demonstrated through experiments on basic and advanced breast phantoms. The basic breast phantom was made of pork fat and the advanced breast phantom was built using 3D printing, based on human breast MRI, filled with liquids that emulate normal and cancerous tissues. The possibility of tracking a biopsy needle inside a breast using this technique was also investigated. The measurement results demonstrated the proficiency of UWB-CSAR for breast tumor imaging and also biopsy needle tracking.

Chapter 2

Design of Pulse Characteristics for Near-field UWB-SAR Imaging

2.1 Introduction

UWB radar technology for imaging applications has been a very popular research topic in industry and academia. UWB signals have an excellent spatial resolution and good penetration into dielectric materials, which makes them the best choice for imaging applications in special mediums. UWB radars have a wide range of uses, not only in military applications but also in commercial tasks such as: data and image acquisition of disaster areas, map building, buried object imaging, search and rescue, as well as in medical imaging [32, 34, 37–43]. A combination of UWB technology with SAR principles is a highly sought-after method for high resolution imaging [15]. Extensive research has been conducted on the UWB-SAR technologies and their applications over the past decade [44, 45]. The research showed that UWB-SAR radar systems are capable of providing high resolution images in both range and cross-range directions [27].

Radar resolution in range and cross-range directions have been defined in different ways [6,15,21,29,46]. However, the design guidelines for pulse characteristics to achieve the desired

resolution, considering the antenna effect on the transmitted and received pulses, have not been discussed in the literatures. Radar image resolution depends on various factors such as: pulse shape, pulse width or frequency bandwidth, pre-processing of the raw data, and the length of the synthesized aperture in case of LSAR.

The effect of various UWB antennas on pulse characteristics during transmission and reception, have been studied in [36]. Almost all of the antennas distort the pulse due to the finite bandwidth and impedance mismatches. In addition, it is shown that most of the antennas, especially aperture ones, time differentiate the input pulse in the transmission mode [47]. Similar effects are also found in antenna arrays of different polarization [48, 49]. In general, the antenna impulse response in the transmission mode is the time derivative of the antenna impulse response in the receiving mode [50]. Hence, for aperture antenna, the antenna does not affect the pulse in the receiving mode. However, the transmitted pulse shape and its frequency spectrum differ from that of the input pulse. Therefore, the antenna effect should be taken into account to design the radar resolution. In addition to antenna's effects, it is also found that the target has an effect on the scattered pulse characteristics; however, these effects are negligible for near-distance measurements [51].

In this chapter, different pulse characteristics for UWB-SAR near-field imaging, and near-distance measurements are comprehensively studied. The effect of preprocessing techniques such as envelope detection [31] and/or match filtering [52] on resolution enhancement is also investigated. The most commonly used radar pulses such as Gaussian and chirp pulses are considered in this study and analyzed for the best possible resolution with respect to frequency bandwidth and integration angles. Closed form expressions for the resolution in the range and cross-range directions for both Gaussian and chirp pulses are presented. The design guidelines to select the pulse characteristics to achieve the desired resolution are also discussed.

2.2 UWB Radar Range Resolution

Range resolution is one of the most important aspects of radar system design, particularly for high-resolution imaging radars. Therefore in this study, the effect of pulse shape, bandwidth and pre-processing of the received pulses on range resolution is considered. Furthermore, the effect of SNR on the received pulse is also studied. In this section, the best achievable range resolution using Gaussian and chirp pulses is investigated and compared. The criterion for range resolution is that the peaks of the overlapped reflected pulses should be separated with at least half of their peak values. The radra range resolution for a square wave is defined as [6]:

$$\Delta_R = \frac{c}{2.BW} \tag{2.1}$$

where c and BW are the speed of light in the medium of propagation and zero-crossing bandwidth of the pulse, respectively. In addition to the frequency bandwidth, the effect of the pulse shape on the range resolution is also considered here. The first derivative Gaussian pulse is the most suited pulse for radar applications due to its zero DC content. The radiated pulse from the transmitting antenna for the first derivative Gaussian input pulse is the second derivative Gaussian pulse [36]. The bandwidth of radiated pulse should be considered for frequency specifications and spectral regulations in case it is required.

2.2.1 Gaussian and chirp pulses

Mathematical representation of the first derivative Gaussian pulse is written as:

$$\frac{d}{dt}(s_g(t)) = \left(\frac{-2t}{\tau^2}\right) e^{-(t/\tau)^2} \tag{2.2}$$

where $s_g(t)$ is the Gaussian pulse, t and τ are the time and the time constant, respectively.

The second derivative Gaussian pulse is written as:

$$\frac{d^2}{dt^2}(s_g(t)) = \left(\frac{2}{\tau^2}\right) e^{-(t/\tau)^2} \left(\frac{2t^2}{\tau^2} - 1\right) \tag{2.3}$$

The chirp pulse is the other commonly used pulse for radar applications and is mathematically represented as:

$$s_c(t) = rect\left(\frac{t}{T_p}\right) e^{j2\pi f_c t + j\pi K t^2} \tag{2.4}$$

where K, $rect$, T_p and f_c are the chirp rate, the rectangular function of time, pulse duration, and center frequency, respectively.

Unlike the Gaussian pulse, the radiated chirp pulse is again a chirp pulse without any change in the pulse shape. For the sake of comparison, the pulse width of the second derivative Gaussian pulse and the frequency band of the chirp pulse are adjusted such that they provide the same bandwidth and center frequency. For instance, the second derivative Gaussian pulse and the chirp pulse with $10GHz$ bandwidth, $-10dB$ crossing points, and their corresponding spectrum are shown in Fig. 2.1. For the study of range resolution, pulses with frequency bandwidths of $5GHz$, $10GHz$, and $20GHz$ are considered.

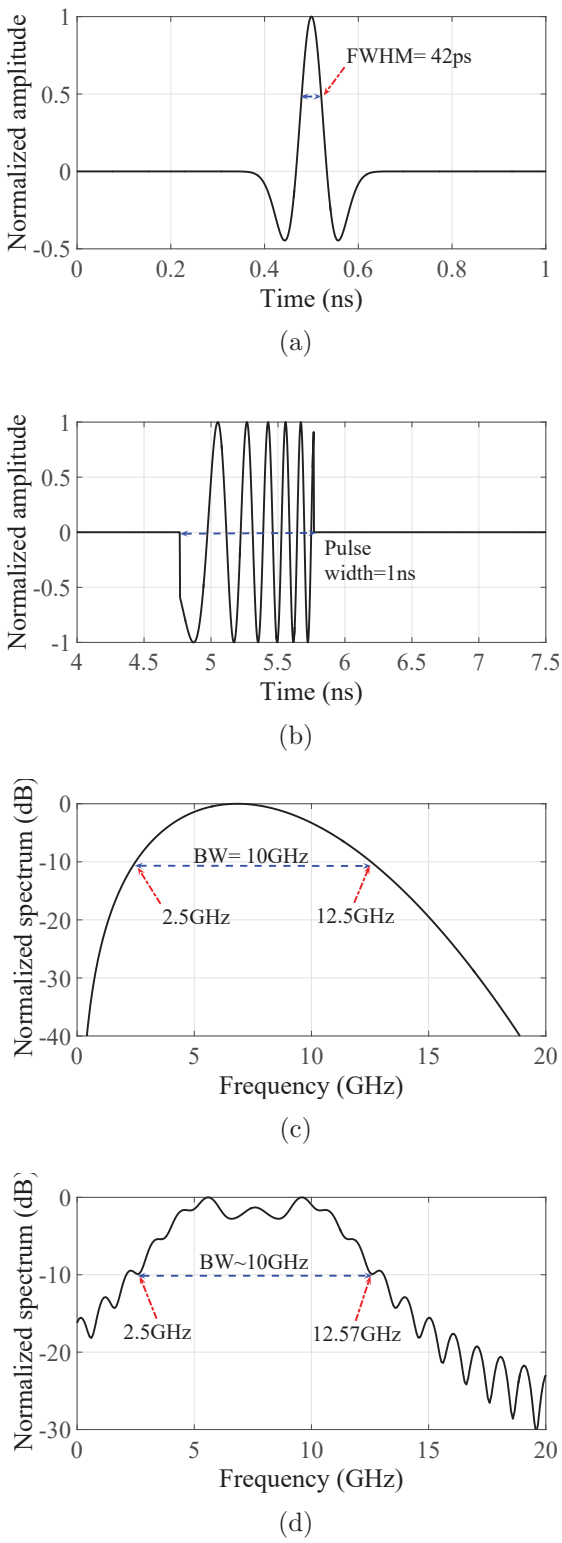

Figure 2.1: EM Pulses; (a) Gaussian pulse, (b) chirp Pulse, (c) Gaussian pulse spectrum, (d) chirp pulse spectrum.

2.2.2 Pre-processing of the received pulses

Range resolution can be improved by pre-processing the received pulses. Match filtering [52] and envelope detection [31] are applied to the received chirp and second derivative Gaussian pulses, respectively. The match filtering technique is also known as pulse compression. Match filtering is defined as:

$$s_m(t) = s_c(t) \otimes s_c(-t)^* \tag{2.5}$$

where $s_m(t)$ is the match filtered pulse, $\otimes$ and $*$ represent the time-domain convolution and conjugate operators, respectively. The compressed pulse of the original chirp pulse, shown in Fig. 2.1(b), is shown in Fig. 2.2(a). Pulse width of the compressed pulse is reduced from $1ns$ to $130ps$. The match filtered chirp pulse reflected by two sequential point targets separated by $8.5mm$ is shown in Fig. 2.2(b). For the chirp pulse of $10GHz$ bandwidth, according to the defined condition for pulse resolution, the best achievable range resolution is $8.5mm$.

The received Gaussian pulse is pre-processed using envelope detection. The Hilbert transform [31] is applied to detect the envelope of the received Gaussian pulse. The envelope of a pulse can be written as:

$$s_{env}(t) = |s_g(t) + j.H\{s_g(t)\}| \tag{2.6}$$

where $s_{env}(t)$ is the envelope of $s_g(t)$, which is a second derivative Gaussian pulse here. The received Gaussian pulse and its envelope reflected by two sequential point targets separated by $7.5mm$ is shown in Fig. 2.2(c). As can be seen after envelope detection these two targets are clearly resolved, whereas they were not in the received Gaussian pulse. It should be noted that using the $10GHz$ second derivative Gaussian pulse, without envelope detection, these two targets can only be resolved if they are separated at least by $9mm$. This shows that pre-processing of the received pulses improves the radar range resolution.

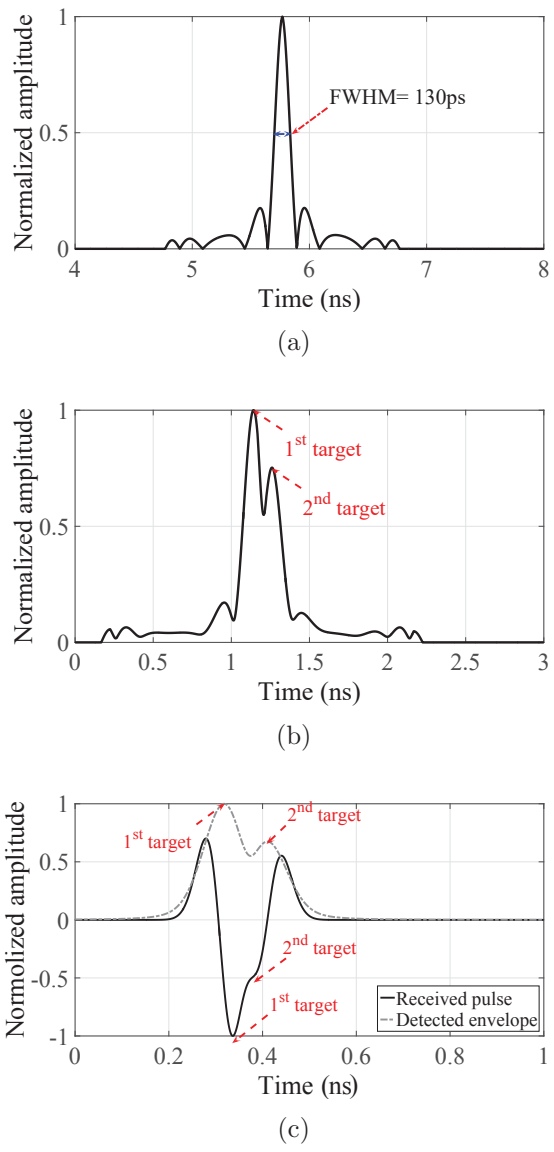

Figure 2.2: Pre-processed pulses; (a) auto-correlated chirp pulse, (b) detected compressed chirp pulse, (c) detected envelope Gaussian pulse.

2.2.3 Achievable range resolution using Gaussian and chirp pulses

In this section, a comparison of maximum achievable range resolution using chirp and second derivative Gaussian pulses is presented. The effect of the SNR on range resolution is also investigated.

The range resolution of second and third derivative Gaussian pulses with different frequency bandwidths for near and far-field measurements are summarized in Tables. 2.1-2.2.

Table 2.1: Second derivative Gaussian pulse range resolution.

Center frequency (GHz)	2.5	7.5	15
-10dB bandwidth (GHz)	5	10	20
$X_{FWHM}[ps]$	83.1	42	20.6
ΔR (mm)	19	9	4.5
$\Delta R_{Envelope}$ (mm)	15	7.5	3.75

Table 2.2: Third derivative Gaussian pulse range resolution.

Center frequency (GHz)	4.1	8.4	16.5
-10dB bandwidth (GHz)	5	10	20
$X_{FWHM}[ps]$	80.6	36.9	30
ΔR (mm)	18	8	4.5
$\Delta R_{Envelope}$ (mm)	14	6.5	3.5

The relationship between a pulse width and range resolution, generally for Gaussian pulses, can be written as:

$$\Delta_R = \frac{cX_{FWHM}}{2} \tag{2.7}$$

where X is the full width at half maximum (FWHM) of the Gaussian pulse. For far-field conditions, the radiated pulse undergoes another time differentiation due to the impulse response of the target [51]; hence the received pulse is the third derivative Gaussian pulse. However, the reflected pulse from a target in near-field measurements is an attenuated version of the incident pulse, or inverted version if the target is made of metal. The range resolution in Tables. 2.1 and 2.2 are comparable. Therefore, for the rest of this study the second derivative Gaussian pulse, which is resulted from near-field measurements, is considered.

Table 2.3: Chirp pulse range resolution.

Center frequency (GHz)	2.5	7.5	15
$-10dB\ BW\ (GHz)$	5	10	20
$\Delta R_{Match\ Filter}\ (mm)$	26	8.5	4.5

The range resolution achieved by the chirp pulse using match filtering, is presented in Table. 2.3. It is a known fact that range resolution improves with bandwidth of the pulse. It is also clear from Tables. 2.1-2.3 that the envelope detected Gaussian pulse provides a better range resolution than the match filtered chirp pulse.

The SNR of the received pulse is another important factor that affects the range resolution. Here, the effect of noise is studied by adding white Gaussian noise to the pulse with a specified SNR. The range resolution of the Gaussian and chirp pulses with various SNR values are summarized in Tables 2.4 and 2.5, respectively. All the range dimensions are in millimeters.

Results show that the range resolution decreases with the SNR of the received pulse, and the chirp pulse has more resistance to the noise compared to the Gaussian pulse. Figs. 2.3(a)-2.3(b) show the second derivative Gaussian and chirp pulse, with $10GHz$ bandwidth and a SNR of $-35dB$, reflected from targets separated by $8.5mm$, respectively. The received pulses are completely merged into noise, and are not detectable. However, the received pulses can be recovered by reducing the noise through averaging/integration of the received pulses [6]. Table 2.4 shows the minimum number of pulses, N, required for averaging to detect the second derivative Gaussian pulse from the noise with respect to the pulse bandwidth. Similarly, Table 2.5 shows the case of the chirp pulse. Furthermore, it is observed that increasing the number of pulses for averaging beyond the values specified in Tables. 2.4 -2.5 does not provide additional improvements in the range resolution.

Table 2.4: Range resolution for various SNR values of Gaussian Pulse.

	-10dB bandwidth (GHz)					
Center frequency (GHz)	5		10		20	
SNR (dB)	ΔR	N	ΔR	N	ΔR	N
10	15	0	7.5	0	3.75	0
5	15	0	7.5	0	3.75	0
0	15	0	7.5	0	3.75	0
-5	15	0	7.5	0	3.75	0
-10	15.5	0	7.5	0	3.75	0
-15	16	0	8	0	3.75	0
-20	16	64	8.5	0	4.25	0
-25	16	80	8.5	64	4.75	0
-30	16	128	8.5	100	4.75	40
-35	16	256	8.5	200	4.75	64

Table 2.5: Range resolution for various SNR values of Chirp Pulse.

	$-10dB$ bandwidth (GHz)					
Center frequency (GHz)	5		10		20	
SNR (dB)	ΔR	N	ΔR	N	ΔR	N
10	26	0	8.5	0	4.5	0
5	26	0	8.5	0	4.5	0
0	26	0	8.5	0	4.5	0
-5	26	0	8.5	0	4.5	0
-10	26	0	8.5	0	4.5	0
-15	26	0	8.5	0	4.5	0
-20	26	0	8.5	0	4.5	0
-25	26	0	8.5	0	4.5	0
-30	26	40	8.5	0	4.5	0
-35	26	64	8.5	40	4.5	30

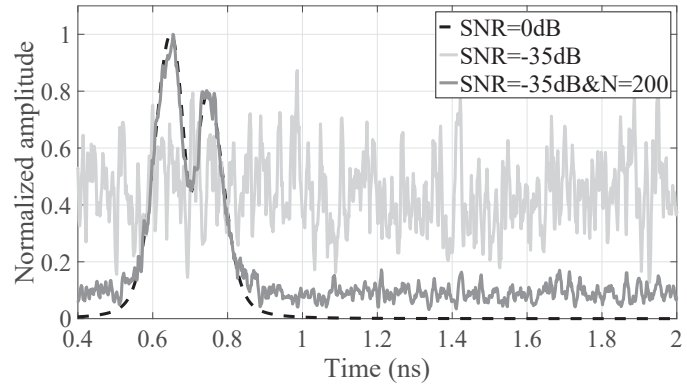

(a)

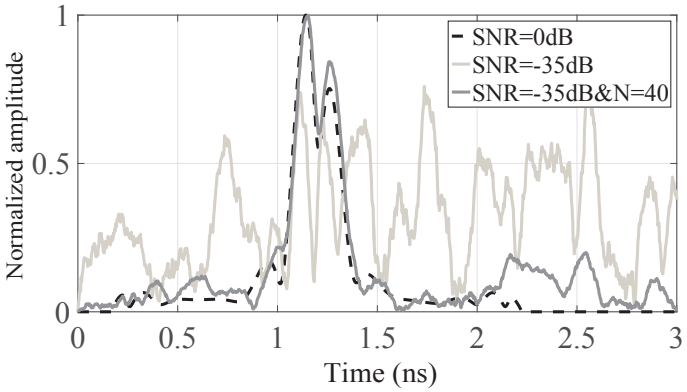

(b)

Figure 2.3: Received pulses with and without Noise; (a) second derivative Gaussian Pulse with envelope detection, (b) matched filtered chirp pulse.

2.3 UWB-SAR Image Resolution

The quality of the radar image depends on both the range and cross-range resolutions of the radar. The effect of the radiated pulse characteristics on the SAR image resolution is studied considering both Gaussian and chirp pulses. The raw data is generated using MATLAB simulations by scanning the point target/s as shown in Fig. 1.3(a). The raw data is collected from two point targets separated by $9mm$ in the range direction using second derivative Gaussian and chirp pulses. The SAR images shown in Fig. 2.4 are generated using compressed chirp pulse and Gaussian pulse with and without envelope detection. Thees images are reconstructed and focused using the time domain GBP method [27, 28]. The reconstructed images are shown in the right column of Fig. 2.4. As can be noted from the images, neither the compressed chirp pulse nor the Gaussian pulse without envelope detection is able to resolve the targets. However, the envelope detected Gaussian pulse is able to resolve the targets.

In Table. 2.1, it is shown that the reflected pulses of same bandwidth, can resolve the inter point target distance of $7.5mm$; however, in the SAR image, the resolution achieved is $9mm$. This is due to image smearing effects. By applying image processing techniques presented in [26,53] on the SAR image, it may be possible to improve the resolution to match that in Table. 2.1.

The cross-range resolution is the minimum distance between two side-by-side targets that can be resolved by a radar. In general, it depends on the antenna beamwidth, i.e., the sharpness of the main beam. Hence, to achieve high cross-range resolution, a physically large antenna is required. However, the SAR processing method has the ability to produce very high cross-range resolution using electrically small antennas. The achievable cross-range resolution by a narrow band LSAR is expressed as [29]:

$$\Delta_{CR} = \frac{H.\lambda}{L} \tag{2.8}$$

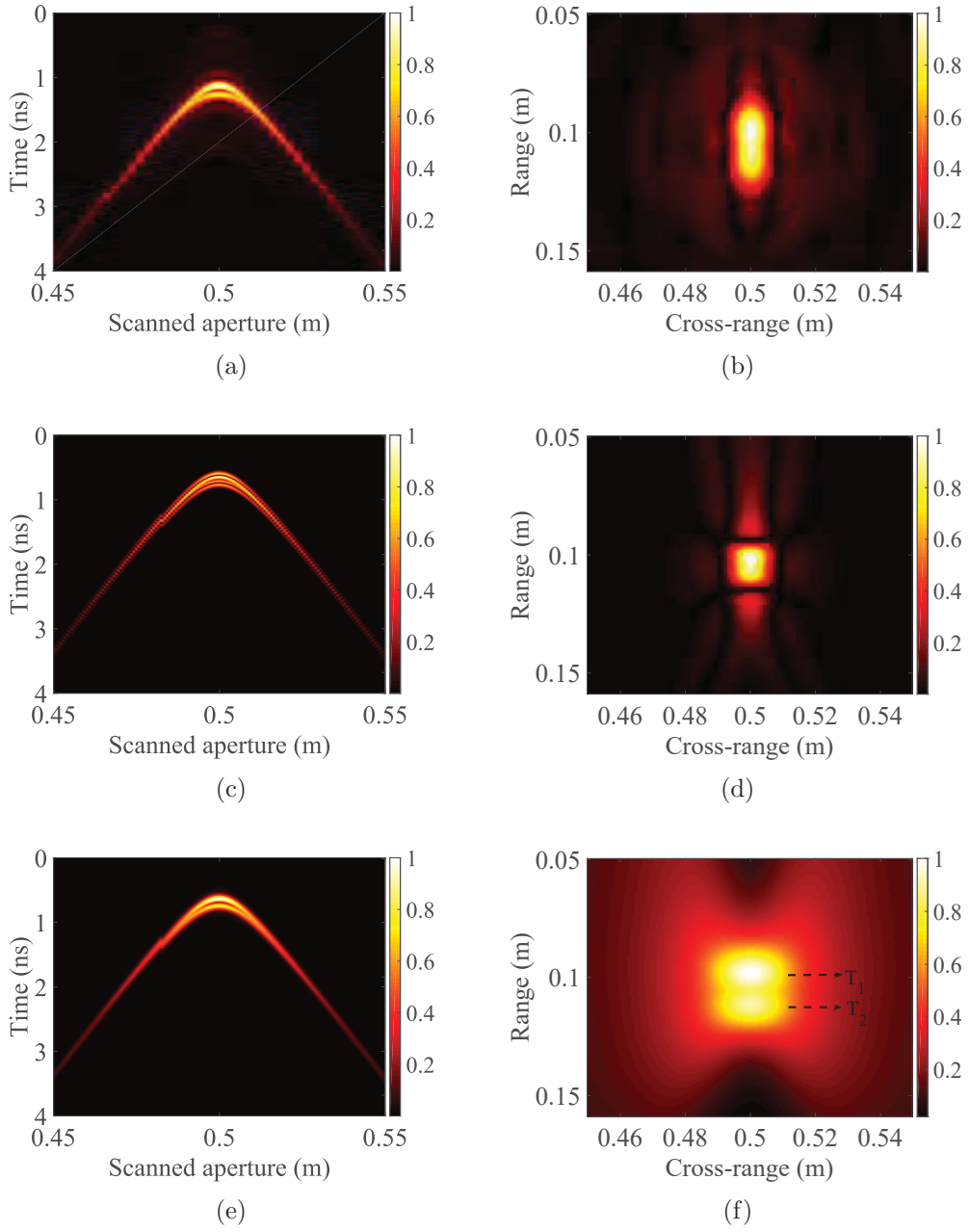

Figure 2.4: SAR image reconstruction of compressed chirp, Gaussian and envelope detected Gaussian pulse; (a) raw data of compressed chirp, (b) reconstructed image of -a-, (c) raw data of Gaussian, (d) reconstructed image of -c-, (e) raw data of envelope detected Gaussian, (f) reconstructed image of -e-.

where H, L and λ are radar altitude, aperture length of the measurements, and wavelength of the radiated signal, respectively. For narrow band LSAR systems, the cross-range resolution depends on the integration angle, i.e., the ratio of altitude to the aperture length, c.f. Fig. 1.3(a). However, the cross-range resolution of UWB-LSAR does not strictly follow Eq. 2.8.

For UWB radar systems, the cross-range resolution depends on bandwidth of the radiated pulse, integration angle, and pre-processing of the received pulses. Here , the cross-range resolution is practically obtained from the reconstructed LSAR images.

The reconstructed image of two point targets separated by $9mm$ in the same slant range is shown in Fig. 2.5. The second derivative Gaussian pulse with $10GHz$ bandwidth, c.f. Fig. 2.1(a), is used to generate the raw data. The targets are not resolved in the raw data; however they are resolved in the reconstructed LSAR image. The cross-range resolution of the LSAR image for various pulse bandwidths and integration angles is also studied. Fig. 2.5(c) shows the maximum achievable cross-range resolution of the matched filtered chirp pulse and the second derivative Gaussian pulse with envelope detection. A closed form expression, Eq. 2.9, is empirically derived to establish a relationship among achievable cross-range resolution, radiated pulse bandwidth, and integration angle.

$$f(\xi,\theta) = p_{00} + p_{10}\xi + p_{01}\theta + p_{20}\xi^2 + p_{11}\xi\theta + p_{02}\theta^2 + p_{30}\xi^3 + p_{21}\xi^2\theta + p_{12}\xi\theta^2 + p_{03}\theta^3 \quad (2.9)$$

where ξ, θ and p are the $-10dB$ bandwidth in GHz, the integration angle in degrees and the coefficients described in Table. 2.6, respectively. This relationship is valid for the pulse bandwidth between $5GHz$ to $20GHz$, and the integration angle between $50°$ to $175°$. The coefficients for the chirp and second derivative Gaussian pulse are presented in Table. 2.6. As can be seen, a higher integration angle and wider bandwidth provide a higher cross-range resolution. It is also observed that the radiated pulse shape has some effect on the range and cross-range resolution. It is showed that the second derivative Gaussian pulse has better performance for image resolution, whereas the chirp pulse shows better resistance to noise at a given SNR value. The chirp pulse is a better choice for the case of low SNR value. Nonetheless, generating a chirp pulse is more complicated than generating a Gaussian pulse, particularly for a wider frequency bandwidth. A Gaussian pulse can be generated using a simple circuit [54], and can provide a higher range and cross-range resolution than other

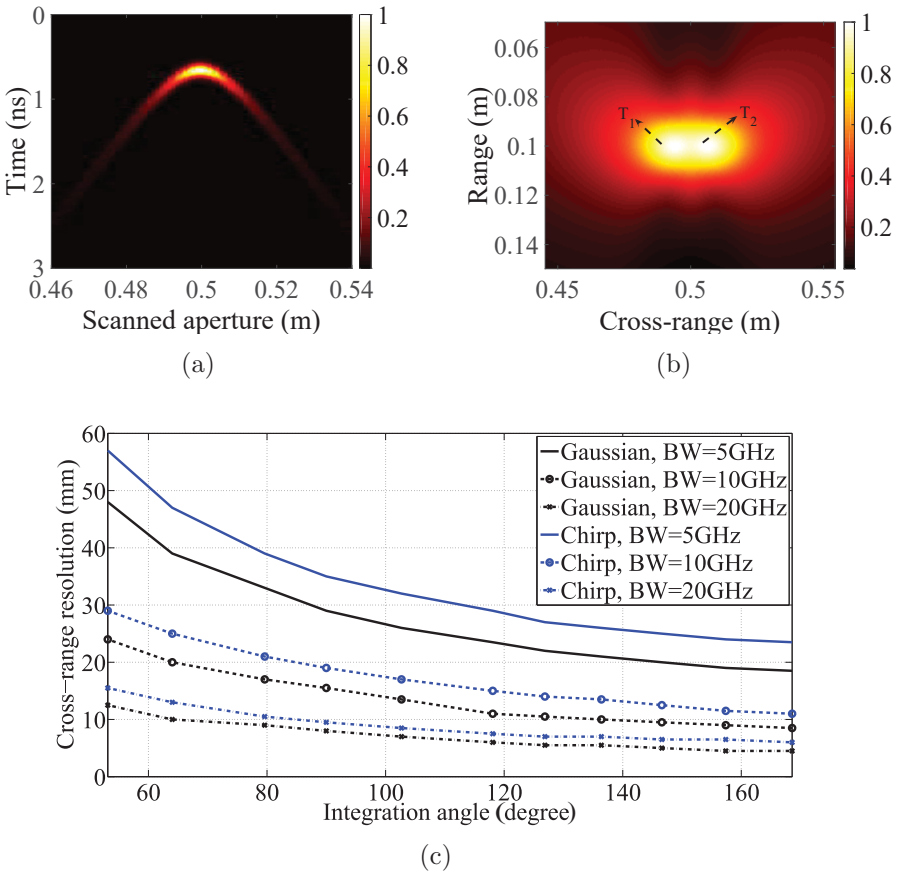

Figure 2.5: (a) Raw data. (b) reconstructed image for two side-by-side targets, $9mm$ distance. (c) UWB SAR cross-range resolution.

practical pulses. To illustrate the range and cross-range resolution the raw data for four point targets separated by $9mm$ using a $10GHz$ bandwidth second derivative Gaussian pulse with envelope detection is generated and shown in Fig. 2.6(a). The reconstructed LSAR image is shown in Fig. 2.6(b). As can be seen all four targets are resolved in both directions, whereas they were merged in the raw data.

In case that the raw data is acquired using the CSAR shown in Fig. 1.3(b), as already mentioned, range and cross-range are the same and a general term resolution is assigned to both. The image resolution for a reconstructed CSAR image can be estimated using:

$$\Delta_R = \frac{c}{\alpha BW} \tag{2.10}$$

Table 2.6: Cross-range resolution equation.

Coefficients	Gaussian	Chirp
p_{00}	122.9	149
p_{10}	-10.45	-11.62
p_{01}	-1.074	-1.456
p_{20}	0.2653	0.2831
p_{11}	0.06678	0.07297
p_{02}	0.00364	0.006544
p_{30}	$-4.121 * 10^{-16}$	$-2.985 * 10^{-16}$
p_{21}	-0.00113	-0.001152
p_{12}	-0.0001308	-0.0001461
p_{03}	$-3.026 * 10^{-6}$	$-1.091 * 10^{-5}$

where, c is speed of light in the medium of propagation. The coefficient α in Eq. 2.10 changes for different pulse shapes, used for data acquisition. It is 3 and 3.5 for a second derivative Gaussian pulses without and with the envelope detection. However α is 2.5 for a chirp pulse. Again the envelope detected Gaussian pulse provides a higher cross-range resolution.

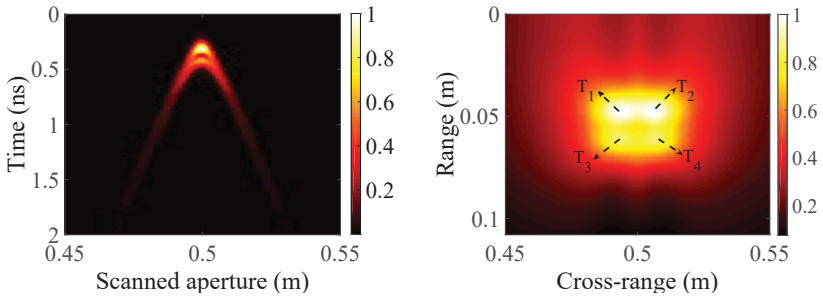

(a) (b)

Figure 2.6: (a) Raw data. (b) reconstructed SAR of four targets separated by $9mm$.

2.4 Guidelines for Design of Pulse Characteristics

Generally for imaging radars, the main design criteria is image resolution. The desired image resolution can be achieved by selecting the optimal pulse bandwidth and integration angle. A trade-off can be made between the pulse bandwidth and integration angle based on either spectral regulations or experimental restrictions. The range resolution depends on the radiated pulse bandwidth or its pulse width. Either a Gaussian or a chirp pulse can be chosen depending on the application. In the case for a Gaussian pulse, the FWHM of the pulse can be estimated. Using Eq. 2.9, it is possible to calculate the required radiated pulse bandwidth for a given integration angle to achieve the desired cross-range resolution of a LSAR system or vice versa. For CSAR systems,the required radiated pulse bandwidth should be estimated by Eq. 2.10. Characteristics of the input pulse for the transmitting antenna to achieve the required bandwidth of the radiated pulse can be calculated. For a second derivative Gaussian radiated pulse, the transmitting antenna should be fed with the first derivative Gaussian pulse. For a second derivative Gaussian pulse, the FWHM of the pulse and $-10dB$ frequency bandwidth are related through the following approximation.

$$\chi = \frac{0.83}{2BW} \tag{2.11}$$

where χ is the FWHM pulse width, and BW is $-10dB$ bandwidth. The accuracy of this approximation is over 95% for all frequency ranges. The corresponding pulse width can be calculated for the radiated pulse. The time constant τ of the second derivative Gaussian pulse can be calculated using Eq. 2.3 and Eq. 2.11.

$$2e^{-(\frac{\chi}{2\tau})^2}\left(1-\frac{\chi^2}{2\tau^2}\right)-1=0 \tag{2.12}$$

Solving Eq. 2.12, the τ value can be calculated. Characteristics of the input pulse, which is the first derivative Gaussian pulse, is estimated using Eq. 2.2 by the value of τ. The peak value of the first derivative Gaussian pulse occurs at $t = \pm\frac{\tau}{\sqrt{2}}$. The FWHM of the first

derivative Gaussian pulse can be calculated by solving Eq. 2.13 for T_1 and T_2.

$$\frac{4.66}{\tau}\left(\frac{\tau}{\sqrt{2}} \pm T_{1,2}\right) e^{\left(\frac{-(\frac{\tau}{\sqrt{2}} \pm T_{1,2})}{\tau^2}\right)} - 1 = 0 \tag{2.13}$$

The pulse width of the first derivative Gaussian input pulse is $T_1 + T_2$.

Unlike the Gaussian pulse design, obtaining the chirp pulse parameters is easier since the antenna does not change the shape of the radiated pulse. The radiated chirp pulse will be in the same shape except for some distortions at the pulse edges. The chirp pulse can be designed using Eq. 2.4. Based on the required bandwidth to obtain the desired resolution, f_c and K can be calculated. In addition to the bandwidth, a higher center frequency provides a higher resolution as well, which has to be considered in the chirp pulse design. The pulse width T_p, does not have a direct effect on the resolution.

2.5 Experimental Verification of the Calculated UWB-SAR Cross-Range Resolution

2.5.1 Measurement setup

In this section, the proposed design procedure for UWB radar cross-range resolution, shown in Fig. 2.5(c), is verified using a set of systematic measurements. The UWB radar demonstrated in Chapter. 1 is used to perform the measurements. Here, the generated first derivative Gaussian pulse with $10GHz$ bandwidth, shown in Fig. 1.6(c)-1.6(d), is used as the transmitted pulse. To improve the SNR of the measured received pulses, pulse averaging/integration is performed.

2.5.2 Imaging of metal strips using UWB LSAR

The shape of the radiated pulse is affected by the radar antennas. These effects have to be considered for estimating the image resolution. As explained earlier, the Tx antenna

differentiates the input pulse while radiating. Moreover, here the antennas return loss limits the bandwidth of the radiated pulse. In this experiment, a pair of Vivaldi antennas with $10dB$ return loss bandwidth from 3.2 to $12GHz$ is used. The Antipodal Vivaldi antenna is one of the most popular UWB antennas. It is an impedance transformer that matches the impedance of the feed line to the impedance of the medium of propagation over a broad range of frequencies. Therefore, an antipodal Vivaldi antenna is a very good candidate for UWB radar applications [55,56]. To estimate the bandwidth and shape of the radiated pulse, full wave simulation using CST microwave studio [57] is carried out. The simulated quasi-mono-static antenna configuration is shown in Fig. 2.7(a). In the simulation, the generated first derivative Gaussian pulse, shown in Fig.1.6(c), is fed to the Tx antenna and the output pulse is measured using voltage probes placed in front of the antennas' aperture at $60mm$, $90mm$, $120mm$, and $150mm$. The shape of the received pulses at various distances and their frequency spectrum are shown in Fig. 2.7(b)-2.7(c), respectively. As can be seen, the shape of the received pulse is the second derivative Gaussian pulse and has $8GHz$ of bandwidth, from 3 to $11GHz$.

LSAR cross-range resolution depends on the characteristics of the radiated pulse and the antenna beam-width. The Vivaldi antenna has about 70° of half-power beam-width. Therefore, cross-range resolution is calculated based on integration angles up to maximum 90°. To verify Eq. 2.9, and error calculations, cross-range resolutions for integration angles of 50°, 60°, 70°, 80° and 90°, for a Gaussian pulse with $8GHz$ bandwidth, are experimentally investigated. The near-field radar imaging setup is shown in Fig. 2.8. Radar transceiver (TRx) is realized by bundling two Vivaldi antennas, separated by a $0.5inch$ thick foam. The copper metal strips dimensions are $4mm \times 15mm$. The distance between the metal strips and the first point of mutual coupling between the antennas is $5cm$. The aperture length is calculated based on the integration angle and distance to the metal strips as follow:

$$L = 2h\left(tan(\frac{\theta_{int}}{2})\right) \tag{2.14}$$

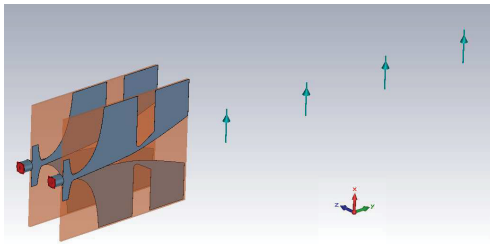

(a)

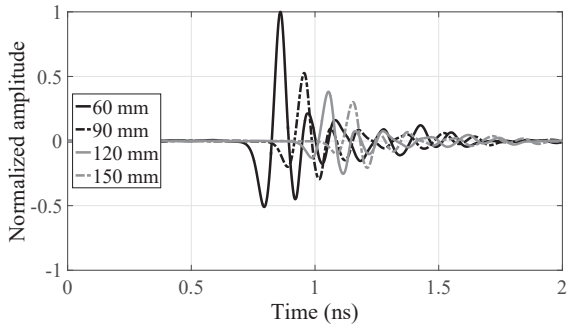

(b)

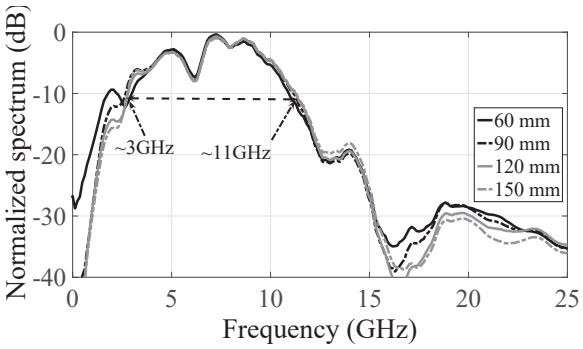

(c)

Figure 2.7: (a) Simulated structure. Antenna output pulses; (b) time domain, (c) frequency domain.

where L, h, and θ_{int} are aperture length, distance to the target and integration angle respectively. The calculated aperture length and the minimum resolvable distance between targets which satisfies Eq. 2.9 are summarized in Table. 2.7. Raw data for different integration angles is measured by moving the TRx over the metal strips for different aperture lengths. The measured raw data and reconstructed SAR image for 50° integration angle is shown in Fig. 2.9(a) and Fig. 2.9(b). As can be seen the merged targets in the raw data are resolved in the reconstructed image. By observing the intensity of the image, two metal strips can be identified. The edge to edge distance between the metal strips is about 31.3mm,

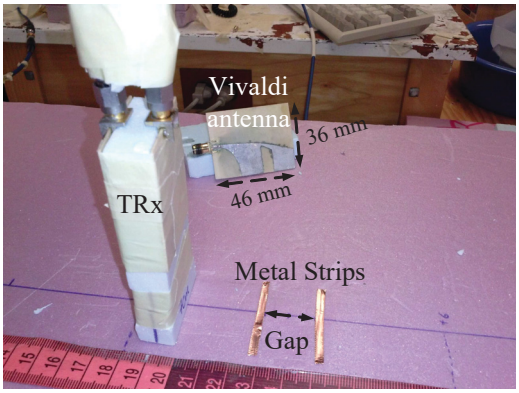

Figure 2.8: Near-field radar imaging setup

which is very close to the calculated value. The measurement results for other integration angles are shown in Table. 2.7. The measurement results confirmed the calculated values for the cross-range resolution with a minimal error, which are also shown in the table.

Table 2.7: Experiment scenarios, measurement results and errors.

Integration angle (degrees)	50	60	70	80	90
Aperture length (mm)	46.6	57.7	70	83.9	100
Calculated cross-range resolution from eq. (2.9) (mm)	31.8	28.2	25.1	22.4	20
Measured cross-range resolution from images (mm)	31.3	28	25.5	22.7	20.3
Error (%)	1.57	0.71	1.59	1.34	1.5

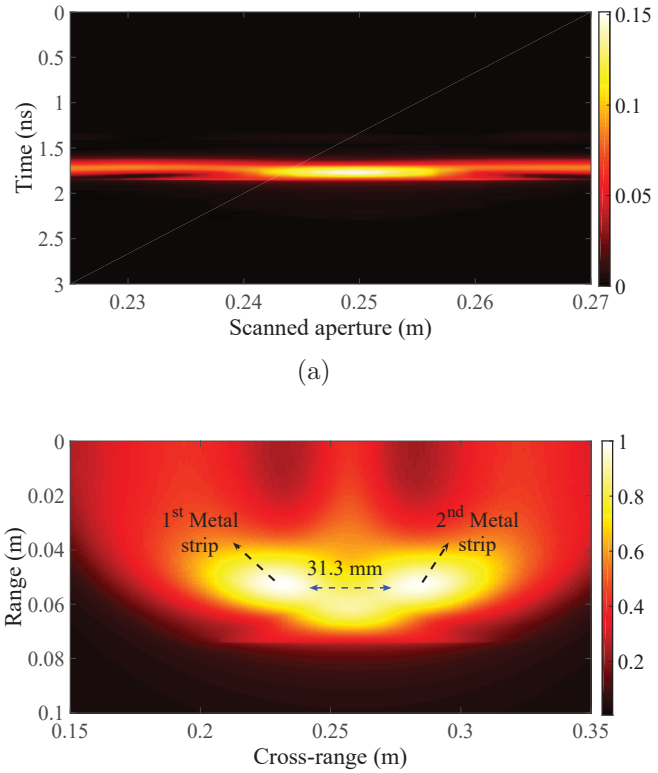

Figure 2.9: (a) Raw data for 50 degrees integration angle, (b) reconstructed image of metal strips.

2.6 Conclusion

The antenna effect on the radiated pulse and its pulse characteristics on the SAR image resolution were studied. Radar range and cross-range resolution as a function of radiated pulse characteristics, integration angle, and SNR were presented. Closed form expressions for range and cross-range resolutions were developed. It was shown that a Gaussian pulse with envelope detection can provide better resolution than a chirp pulse with match filtering at higher SNR values. However, the chirp pulse has more resistance to the noise at the given SNR value. A design guideline for radar image resolution for near-field SAR radars was provided. The designed guide line for cross-range resolution was verified using full-wave simulations and measurements.

Chapter 3

Studying the Superluminal behavior of UWB Antennas and its Effect on Near-Field Imaging

3.1 Introduction

Superluminal wave propagation refers to the phenomenon whereby an electromagnetic wave appears to propagate faster than the speed of light (c_o) in the vacuum. The superluminal behavior of the electromagnetic wave, where the pulse velocity is greater than c_o, can be associated with one of the following wave interaction mechanisms: anomalous dispersion [58, 59] , evanescent propagation [60–62], or wave interference [63–65]. It has been reported in the literature that the electromagnetic fields very close to the antenna, inside the near-field region, show the evanescent wave properties, and also exhibit superluminal behavior [66–68]. In [66], it is analytically shown that near-field of an infinitesimal dipole shows superluminal velocity. However, no experimental validation or explanation for this behavior is presented. The possibility of observing superluminal behavior in the propagation of localized microwaves over a distance of tens of wavelengths is also demonstrated in [63].

In this chapter, we first discuss the superluminal phase and group velocities of an infinitesimal dipole antenna from both frequency and time domain radiation perspectives. The pulse deformation and superluminal propagation of a radiated pulse in the near-filed of a dipole antenna and a UWB antenna are explained theoretically, numerically and experimentally. The superluminal behavior of a UWB antenna and its effect on the near-field radar imaging are also demonstrated.

3.2 Group and Phase Velocities in the Near-Field of a Dipole Antenna: Frequency Domain Perspective

The most general way to obtain the expression of group velocity is the stationary-phase method. The main idea of this method is based on the cancellation of sinusoids with rapidly varying phase. If many sinusoids have the same phase and are added together constructively, the peak of a wave packet or pulse is formed. If, however, these same sinusoids have phases which change rapidly as the frequency changes, they will add incoherently, varying between constructive and destructive additions at different times, which results in pulse deformation. Group velocity is defined as the velocity of the peak of the pulse, where most of the energy of a wave packet or pulse is concentrated. Therefore, at the location of pulse peak, the phase variation with respect to frequency is zero and its gradient is the group velocity. In general, a field quantity $\phi(r,t)$ can be expanded as the superposition of different frequency components:

$$\phi(r,t) = \frac{1}{2\pi}\int_{-\infty}^{\infty} F(\omega)e^{-j(\omega t - kr)}d\omega \tag{3.1}$$

Let $\varphi = (\omega t - kr)$ be the phase of the signal, which depends on the time and location. According to the stationary-phase method, the group velocity (v_g) and phase velocity (v_p)

can be written as:

$$v_g = -(\frac{\partial^2\varphi}{\partial t\partial k})/(\frac{\partial^2\varphi}{\partial r\partial k}) \tag{3.2a}$$

$$v_p = -\omega/\frac{\partial\varphi}{\partial r} = -c_o k/\frac{\partial\varphi}{\partial r} \tag{3.2b}$$

Assume that an electric dipole is oriented along the z-axis, extending from $z = -\frac{l}{2}$ to $z = \frac{l}{2}$ and $l << \lambda$. The non-zero components of electromagnetic fields radiated by the dipole are [24]:

$$H_\varphi = \frac{jkI_0 l sin\theta}{4\pi r}\left[1 + \frac{1}{jkr}\right] e^{j(\omega t - kr)} \tag{3.3a}$$

$$E_r = \frac{\eta I_0 l cos\theta}{2\pi r^2}\left[1 + \frac{1}{jkr}\right] e^{j(\omega t - kr)} \tag{3.3b}$$

$$E_\theta = \frac{j\eta k I_0 l sin\theta}{4\pi r}\left[1 + \frac{1}{jkr} + \frac{1}{(kr)^2}\right] e^{j(\omega t - kr)} \tag{3.3c}$$

These field components Eq. 3.3 are valid everywhere, except on the antenna surface. I_0 is the antenna excitation current, r is the distance from the antenna, k is the free space propagation constant, η is the free space intrinsic impedance, ω is the radian frequency and θ is the angle between the direction of observation and the polarization direction of the electric dipole. The field components have different terms: as $\frac{1}{r^3}$, $\frac{1}{r^2}$ and $\frac{1}{r}$. The $\frac{1}{r^3}$ term is called the electrostatic field; the $\frac{1}{r^2}$ term is the inductive field, which can be predicted from Biot-Savart's law as well, and the $\frac{1}{r}$ term is called the far-field or radiation field.

For mathematical simplicity, and to show the phase variation with respect to space-time coordinates, the field equations have been rewritten by ignoring the far-field term, which is negligible in the near-field ($kr << 1$). To study the superluminal behavior in the near-field,

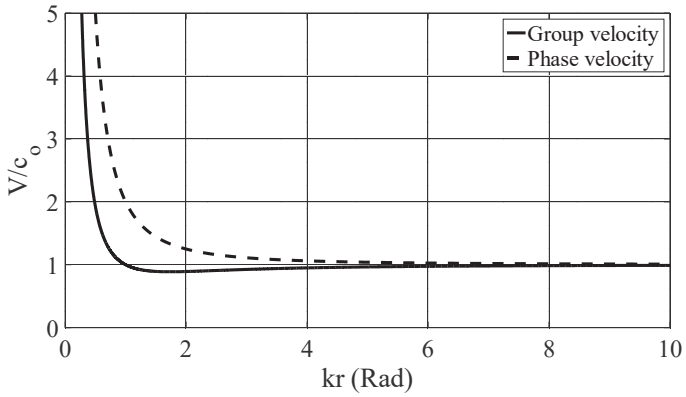

Figure 3.1: Calculated phase and group velocities of an infinitesimal dipole

the following components of the electric fields are considered:

$$E_r = E_1 \frac{cos\theta}{r^2}[1 + \frac{1}{jkr}]e^{j(\omega t - kr)} = |E_r|\, exp(j(\psi + C_1)) \tag{3.4a}$$

$$E_\theta = E_2 \frac{sin\theta}{jkr^2}[1 + \frac{1}{jkr}]e^{j(\omega t - kr)} = |E_\theta|\, exp(j(\psi + C_2)) \tag{3.4b}$$

Here E_1 and E_2 are either pure real or imaginary, where $\psi = \omega t - kr + tan^{-1}(-\frac{1}{kr})$, and C_1 and C_2 are the initial phases of the electric field components. The group and phase velocities can be calculated based on the ψ value and Eq. 3.2 as shown below:

$$v_g = c_o[\frac{(kr)^4 + 2(kr)^2 + 1}{(kr)^4 + 3(kr)^2}] \tag{3.5a}$$

$$v_p = c_o[\frac{1 + (kr)^2}{(kr)^2}] \tag{3.5b}$$

Fig. 3.1 shows the phase and group velocities of the radiated signals in the near-field of an infinitesimal dipole antenna. Both the phase and group velocities show the superluminal behavior in the near-field. We further analyze the phase and group velocities of an infinitesimal dipole using time-domain analysis.

3.3 Dipole Antenna Radiation: Time Domain Perspective

Radiation from a dipole can be derived by means of the time-retarded Hertz vector as proposed in [69, 70]. The radiated electric and magnetic field components can be written as:

$$E(r,t) = \frac{1}{4\pi\epsilon_0}\left\{\hat{\theta}\frac{sin\theta}{r^2}\left[\frac{p(\hat{t})}{r} + \frac{1}{c_o}\frac{dp(\hat{t})}{dt} + \frac{r}{{c_o}^2}\frac{d^2p(\hat{t})}{dt^2}\right]\right\} + \hat{r}\frac{2cos\theta}{r^2}\left[\frac{p(\hat{t})}{r} + \frac{1}{c_o}\frac{dp(\hat{t})}{dt}\right] \quad (3.6a)$$

$$H(r,t) = \hat{\phi}\frac{sin\theta}{4\pi r^2}\left[\frac{dp(\hat{t})}{dt} + \frac{r}{{c_o}^2}\frac{d^2p(\hat{t})}{dt^2}\right] \quad (3.6b)$$

where $p(t)$ is the time varying dipole moment, which is related to the excitation current of for the antenna as $i(t) = (1/l)(dp(t)/dt)$, where l is the length of the dipole and $\hat{t} = t-(r/c_o)$. The radiated pulse is the superposition of various pulse components, Eq. 3.6, which are propagating with the speed of light. The pulse deformation occurs due to the superposition of various terms in the radiated fields, which changes the shape of the radiated pulse in the near-field with respect to distance r. The speed of the radiated pulse's peak exhibits superluminal behavior even though individual terms are luminal. However, the front-runner of the radiated pulse is always luminal. Hence, it can be argued that the superluminality is due to the pulse reshaping and does not violate the principles of causality. The superluminal phenomenon of the radiated pulse in the near-field of a dipole antenna can be demonstrated as follows: The radiated pulse is the superposition of various terms, including $1/r^3$, $1/r^2$ and $1/r$. However, in the far-field, $1/r$ term dominates the radiated fields. The radiated electric field has two field components: transverse ($\hat{\theta}$) and radial ($\hat{r}$). The radial field component die-off as the pulse propagates into the far-field region. Here we analyze various terms of the transverse field component with respect to space-time coordinates. Various terms of the

transverse field component for a Gaussian dipole moment, i.e., a first derivative Gaussian current excitation, and for $\theta = 90^\circ$ are:

$$E_1 = \frac{1}{4\pi\epsilon_0 r^3} exp\left(-\left(\frac{t-\frac{r}{c_o}}{\tau}\right)^2\right) \tag{3.7a}$$

$$E_2 = \frac{1}{4\pi\epsilon_0 r^2 c_o}\left(\frac{-2(t-\frac{r}{c_o})}{\tau^2}\right).exp\left(-\left(\frac{t-\frac{r}{c_o}}{\tau}\right)^2\right) \tag{3.7b}$$

$$E_3 = \frac{1}{4\pi\epsilon_0 r^2 c_o}\frac{2}{\tau^2}\left(\frac{-2(t-\frac{r}{c_o})^2}{\tau^2} - 1\right).exp\left(-\left(\frac{t-\frac{r}{c_o}}{\tau}\right)^2\right) \tag{3.7c}$$

where τ is the pulse width and r/c_o is the retarded time. The individual terms (E_1 to E_3) and superposition of all three terms (E_T) at a given location with respect to time are shown in Figs. 3.2(a)-3.2(c). Here the dipole is excited by the first derivative Gaussian current pulse with a $20GHz$ of bandwidth. For illustration purposes, the time is offset by $0.1ns$ and the amplitude is offset along the vertical axis. This figure illustrates the pulse deformation and apparent superluminal behavior of the radiated pulse. The radiated pulse (E_T) has different pulse shapes at various distances from the radiating source. In the near-field, the pulse peak is ahead of the individual terms of the radiation components, whereas in the far-field the radiated pulse propagation becomes luminal, as the contribution from E_1 and E_2 becomes negligible compared to E_3. The velocity of the pulse is calculated using the pulse peak, pulse envelope peak and pulse centrovelocity.

The pulse peak velocity is calculated based on the difference in space and time coordinates for the actual radiated pulse, and for the envelope of the pulse generated using the Hilbert transformation, which was explained in Chapter. 2. The Hilbert transform analysis provides

a method for determining the instantaneous power of a pulse [71]. Squaring the pulse envelop obtains a time dependent expression for the instantaneous power. Therefore, the peak of the envelope tracks the peak power of the radiated pulse.

The pulse centrovelocity is calculated through [72]:

$$v = \left| \nabla \left(\int_{-\infty}^{\infty} t E_T^2(r,t) dt \right) / \int_{-\infty}^{\infty} E_T^2(r,t) dt \right|^{-1} \tag{3.8}$$

The calculated pulse centrovelocity along with pulse peak and pulse envelope velocities are plotted in Fig. 3.2(d). All three velocities are superluminal in the source near-field and become luminal far from the source. Moreover, there is a good match between calculated pulses velocities in Fig. 3.1 and Fig. 3.2(d) from the perspectives of frequency and time domain. This study also found that the value of the pulse velocity and extent of superluminality from the antenna changes with the bandwidth of the excitation pulse. For example, a pulse of infinite bandwidth will not show any superluminal behavior.

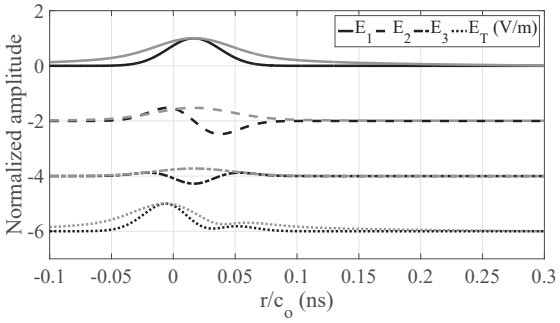

(a)

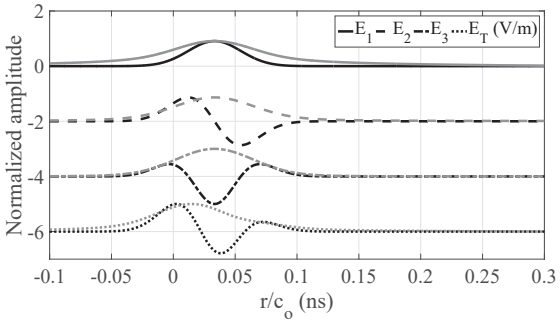

(b)

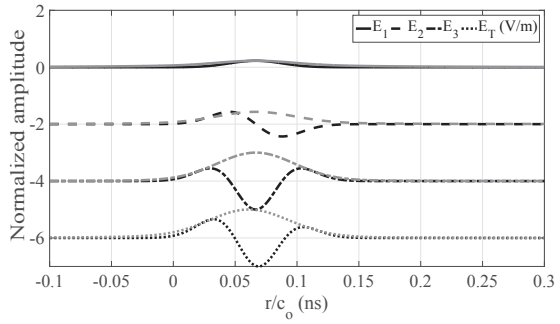

(c)

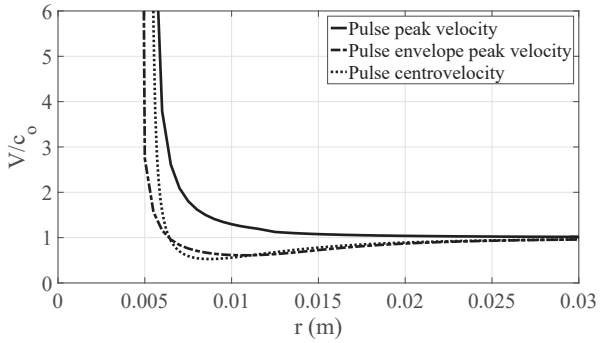

(d)

Figure 3.2: Pulse shaping of the radiated pulse at various distances; (a) pulses at $5mm$, (b) pulses at $10mm$, (c) pulses at $15mm$, note: the envelope of the pulses are plotted in gray, (d) calculated velocity of the radiated pulse in different forms.

3.4 Miniaturized Vivaldi Antenna to Conduct Simulations and Measurements

Radar near-field imaging technology is used for applications such as imaging inside a narrow pipe to study corrosion, microwave holography for tissue imaging, monitoring subsurface conditions, breast tomography to identify tumors, and inspecting wood quality. High resolution near-field imaging requires wide bandwidth and miniaturized antennas. UWB antennas provide the required bandwidth for efficient pulse radiation.

Here the antipodal Vivaldi antenna shown in Fig. 1.7(b), which operates from 3.2 to 15GHz in free space, is used to carryout simulations and measurements. The antenna is miniaturized so that it can be used for applications with space limitations. The antenna size is miniaturized by introducing a slot over the antenna flare which increases the current path. The conventional and miniaturized Vivaldi antennas and their dimensions are shown in Fig. 3.3. More explanations about this antenna can be found in chapters. 5 and 6.

Derivation of an analytical solution for time-domain radiation of a practical antenna such as Vivaldi is much more complicated. Hence, we study the superluminal behavior of the miniaturized UWB Vivaldi antenna using full-wave simulations and measurements. The

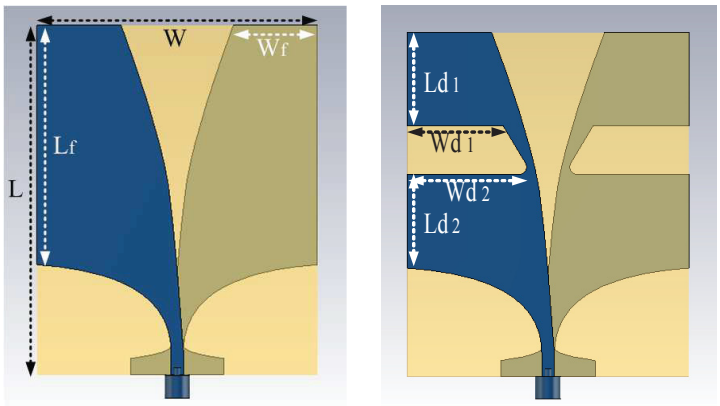

(a) (b)

Figure 3.3: Antipodal Vivaldi antenna, (a) conventional antenna with cutoff frequency of 4.9 GHz, (b) miniaturized antenna with cutoff frequency of 3.2 GHz. $L = 46mm$, $W = 36mm$, $Lf = 31.5mm$, $Wf = 10.8mm$, $Ld1 = 12.5mm$, $Ld2 = 12.5mm$, $Wd1 = 12.3mm$, $Wd2 = 14.3mm$.

effect of superluminal pulse velocity on SAR image reconstruction for near-field applications is also experimentally demonstrated.

3.4.1 Pulse deformation and superluminality study of the UWB Vivaldi antenna using simulation

The effects of the UWB Vivaldi antenna on pulse radiation and deformation, which result in superluminality in the near-field, have been numerically studied using the full-wave simulation tool, CST Microwave Studio [57]. The radiated pulses have been recorded by placing ideal voltage probes at various distances from the antenna. Fig. 3.4(a) shows the recorded radiated pulses at $5mm$ to $15mm$ from the antenna. Experimental errors and the effect of the receiving antenna have not been presented in the simulations, as the ideal voltage probe is used to record the received pulses. The excitation current pulse is the first derivative Gaussian pulse shown in Fig. 1.6(c)-1.6(d). The radiated pulse resembles the time derivative of the excitation pulse, i.e., the second derivative Gaussian pulse. Fig. 3.4(b) shows the fidelity factor of the received pulses with the second derivative Gaussian pulse. The fidelity factor studies the pulse deformation which is defined through a correlation function [73]. The fidelity factor varies by distance from the antenna aperture. The radiated pulse changes its shape in the near-field; however, its pulse shape is consistent in the far-field. A high fidelity factor, about 95 %, after $20mm$ shows the radiated pulse is a second derivative Gaussian pulse. Fig. 3.4(c) shows the pulse velocities with respect to the distance from the antenna. The velocities are calculated based on the time interval between the peaks of the radiated pulses at various distances. The pulse peak velocity is $1.8c_o$ very close to the antenna, and $1.2c_o$ between the distances of $5mm$ and $10mm$ from the antenna. However, it reaches c_o after $60mm$. The pulse envelope peak velocity and centrovelocity are calculated as well and shown in Fig. 3.4(c). The pulse centrovelocity is also superluminal close to the antenna and become luminal far from the antenna. However, the pulse envelope peak velocity shows only luminal behavior, unlike the infinitesimal dipole. This could be due to different radiation

mechanisms of the Vivaldi antenna and the infinitesimal dipole antenna. The velocity traces are smoothed using the moving average filter [74].

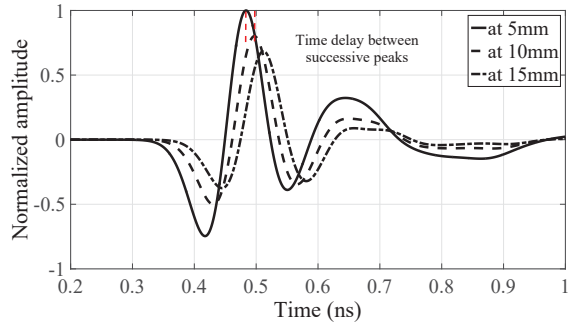

(a)

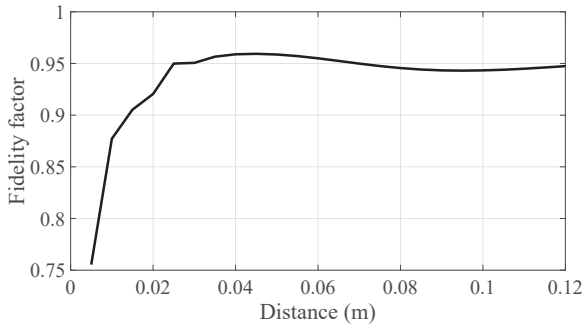

(b)

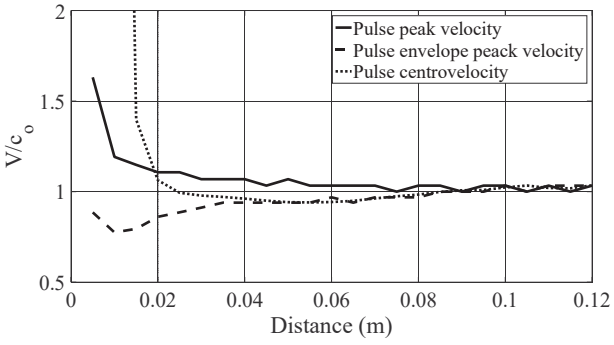

(c)

Figure 3.4: Full-wave simulated results; (a) recorded pulses at various distances, (b) correlation between the received pulse and the second derivative Gaussian pulse, (c) calculated pulse velocities.

3.5 Evaluating Pulse Peak and Phase Velocity using Measurements

In this section, the pulse peak and phase velocity in the vicinity of the UWB Vivaldi antenna is evaluated through different measurements scenarios. The phase velocity can be measured using the phase difference between the waves' oscillations observed at two different points in the plane wave at a given time. The pulse velocity, in different forms as mentioned already, is calculated based on the location of peaks of the pulse over a time interval.

3.5.1 Measurement setup

The pulse peak and phase velocities, based on different definitions, in the near-field of a UWB antenna are studied in face-to-face and quasi-mono-static radar configurations with two identical UWB Vivaldi antennas. The experimental setup for pulse velocity measurements in time domain is shown in Fig. 1.6(b) and Fig. 3.5(a) and with the generated Gaussian pulse shown in Fig. 1.6(c) as input. In this experimental setup, the minimum time interval that can be measured using the sampling oscilloscope is $0.5ps$. Hence, the maximum possible error in time measurement would be $0.25ps$. The pulse propagation time between the Tx and Rx includes the delay that occurs in the connecting cables, the group delay of the antennas, and the propagation delay in air. However, the time delay due to cables, antennas, and the receiver system is calibrated by considering the difference in the time delay between the peak of received pulses at two different locations of the receiving antenna. Phase velocity measurements have been carried out using the vector network analyzer (VNA) (Agilent $E8362B$) shown in 3.5(b), by measuring the phase of the received signal at various frequencies in face-to-face configuration.

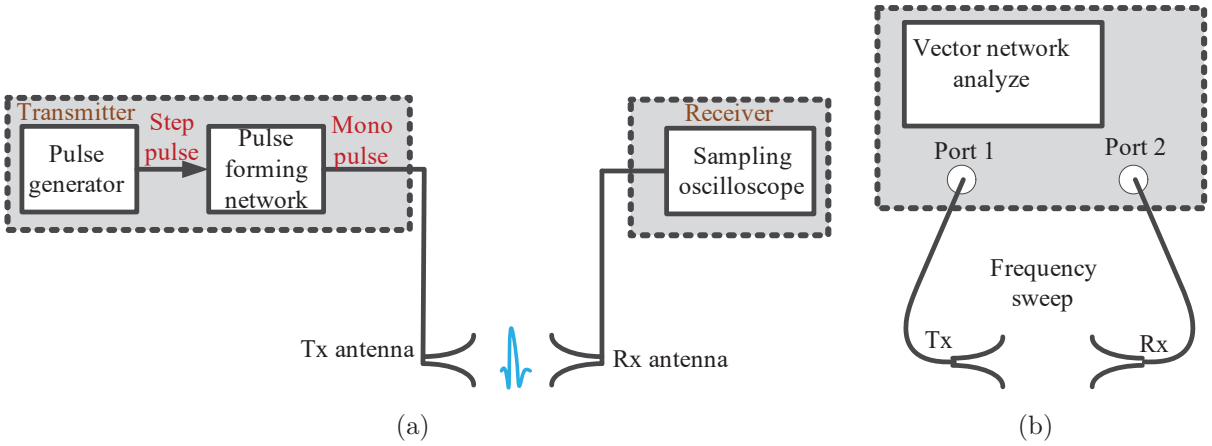

Figure 3.5: (a) UWB radar setup for time domain measurements; (b) vector network analyzer for frequency domain measurements.

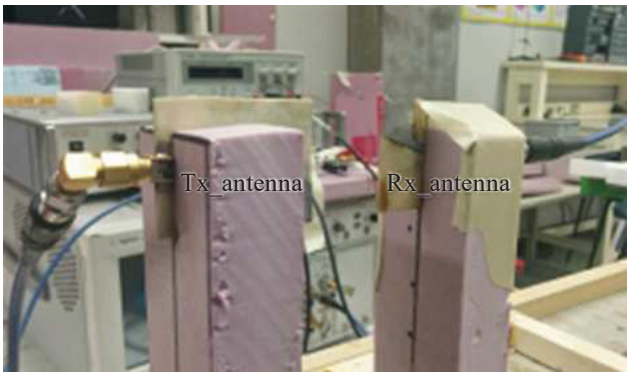

(a)

(b)

Figure 3.6: Experimental setup for the pulse velocity measurements for; (a) face-to-face configuration, (b) quasi-mono-static radar configuration.

3.5.2 Pulse velocity measurements in face-to-face antenna configurations

In face-to-face antenna configurations, as shown in Fig. 3.6(a), the transmitted pulses are received at various locations of the receiving antenna. Fig. 3.7(a) shows the received pulses recorded at $5mm$, $10mm$ and $15mm$ from the aperture of the transmitting antenna.

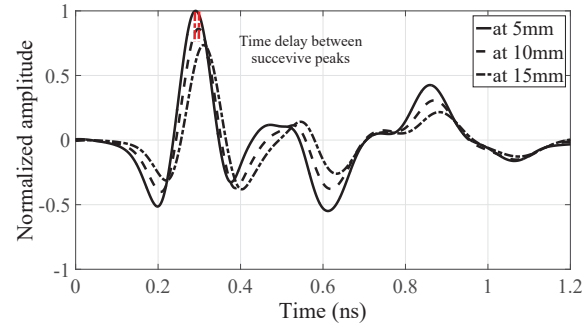

(a)

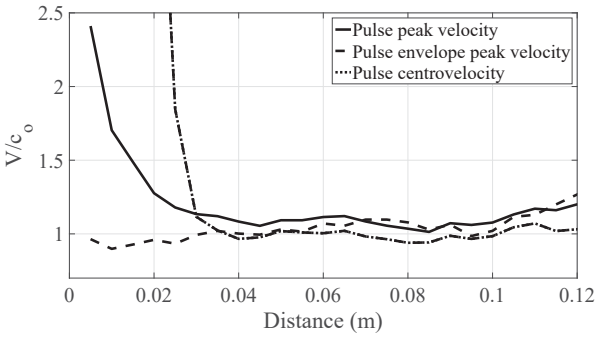

(b)

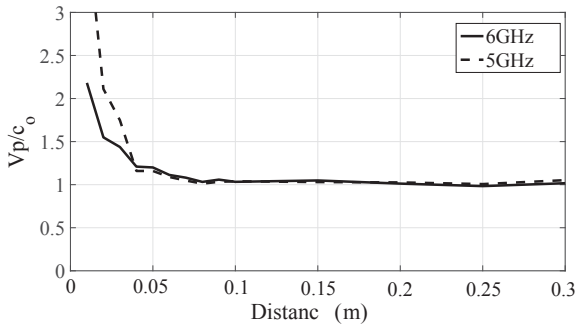

(c)

Figure 3.7: Face-to-face configuration measurements; (a) measured received pulses, (b) calculated pulse velocities of the received pulse, (c) phase velocity at $5GHz$ and $6GHz$.

The transmitting antenna differentiates the input pulse. Hence, the received pulse is a second derivative Gaussian pulse with some ringing that can be due to the input pulse itself or finite bandwidth and impedance mismatching of the antennas. Fig. 3.7(b) shows the measured pulse velocities calculated based on the time difference between the peaks of the received pulses and their corresponding antenna positions. The error in pulse peak velocity measurements, including errors that occur in both the time and distance measurements, is about 8%. The phase velocity is calculated based on the phase difference between the two positions of the antenna measured using the VNA at $5GHz$ and $6GHz$, and is shown in Fig. 3.7(c).

3.5.3 Pulse velocity measurements in quasi-mono-static radar configuration

In this section, the pulse velocity is obtained based on the received pulses measured in a quasi-mono-static configuration. The experimental setup for a quasi-mono-static radar configuration is shown in Fig. 3.6(b). It consists of a radar TRx and a metal reflector. The transmitted pulses are reflected by the metal reflector positioned at various distances from the radar. The recorded reflected pulses at $5mm$ to $15mm$ from the radar are shown in Fig. 3.8(a). The transmitting antenna excitation pulse is the same as the pulse shown in Fig. 1.6(c) . The received pulse in quasi-mono-static configuration is affected by the antenna transfer function, nearby objects and the targets, and mutual coupling between the antennas. This effect is more complicated for near-field imaging. In this configuration, the pulse couples to the receiving antenna before it is reflected by the targets. Therefore to detect the target signature other effects have to be removed. The pulse calibration procedure is explained in detail in Chapter. 1.

The effect of the metal reflector on the shape of reflected UWB pulse is well studied in [51]. As mentioned earlier, the shape of the transmitted pulse changes with the distance. Moreover, the shape of the reflected pulse also changes with the distance from the reflector.

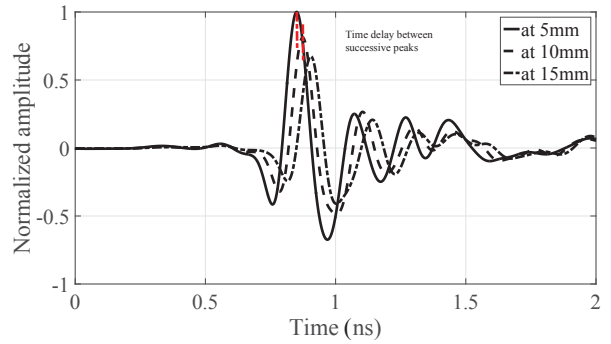

(a)

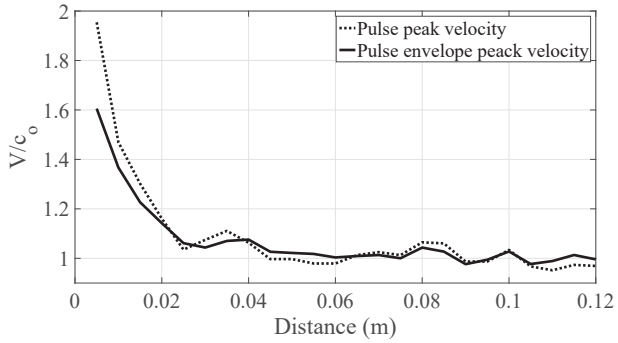

(b)

Figure 3.8: Quasi-mono-static configuration measurements; (a) measured received pulses, (b) calculated pulse velocities of the received pulse.

Hence, the shape of the received pulse changes with the distance between the reflector and the receiving antenna. Fig. 3.8(b) shows both the measured pulse peak and envelope peak velocities of the radiated pulse in quasi-mono-static radar configuration. The pulse centrovelocity is not considered for quasi-mono-static configuration as the receiver location is not changing during the measurements. Both the experiments show the superluminal behavior of the radiated pulse in the near-field of the antenna.

3.6 Effect of Pulse Velocity on the Quality of Reconstructed Image in SAR processing

Pulse velocity plays a significant role in image reconstruction using SAR processing. On the other words, the quality of the reconstructed image directly depends on the accuracy of the pulse velocity used in SAR processing. In SAR systems, the target is viewed from various positions along the synthetic aperture as explained in the first chapter. The information about the target appears in the time domain at an instant of time that depends on the target distance from the radar position and velocity of the pulse. In image reconstruction process, the energy in the received pulses will be refocused to the right location. For accurate image reconstruction, the signal speed used for the SAR processing and the actual pulse velocity of the electromagnetic pulse, or the average velocity of the pulse in the round-trip time, should be the same. Any mismatch in these quantities will degrade the quality of the reconstructed image due to the defocussing of the energy in the received pulse. It is a common practice to assume that the speed of the signal in the SAR process is the same as speed of light in the medium. However, in the previous sections it was demonstrated that the pulse velocity of the radiated pulse can be superluminal in the near-field of the radar transceiver. Pulse velocity and the extent of superluminality depend on the size of the antenna, pulse frequency bandwidth, and the target size.

The following subsections investigate the effect of pulse velocity on the quality of the reconstructed image for both LSAR and CSAR. For this study, the raw data is generated using Matlab for a point target. A second derivative Gaussian pulse with $10GHz$ of bandwidth, $-10dB$ crossing-points, is used as the radiated pulse.

3.6.1 LSAR

Raw data for LSAR is generated by scanning a point target located $3cm$ away from the radar over an aperture length of $20cm$ with a pulse peak velocity of $6 \times 10^8 m/s$, and is shown in

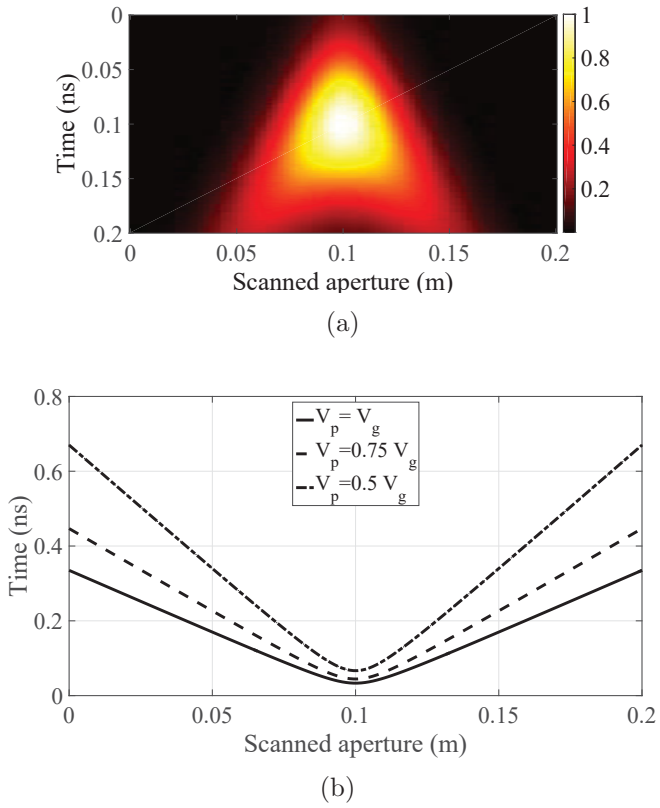

Figure 3.9: (a) Point target raw data, (b) a set of time delay profiles for image reconstruction.

Fig. 3.9(a). Due to the short distance between the target and radar, and relatively large pulse width compared to distance, the raw data is appears as a triangular shape instead of a hyperbolic shape. As the raw data is generated in the time domain, the image is reconstructed using the GBP method in the time domain [27, 28].

In the GBP method, the image is reconstructed based on the time delay profile over the synthesized aperture. For instance, a set of time delay profiles calculated based on different pulse velocities is shown in Fig. 3.9(b). The solid black line is the time delay calculated using the pulse peak velocity of $6 \times 10^8 m/s$, and the other two dashed lines are calculated for pulse peak velocities of $4.5 \times 10^8 m/s$, and $3 \times 10^8 m/s$ respectively. Different pulse peak velocities result in different time profiles, which results in different levels of image distortion. The images reconstructed using different pulse peak velocities are shown in Fig. 3.10(a)-3.10(c). The image reconstructed with the right pulse peak velocity is fittingly reconstructed to the

right location, and is sharply focused. However, the other two images reconstructed with lower pulse velocities are not focused properly and the image became elongated.

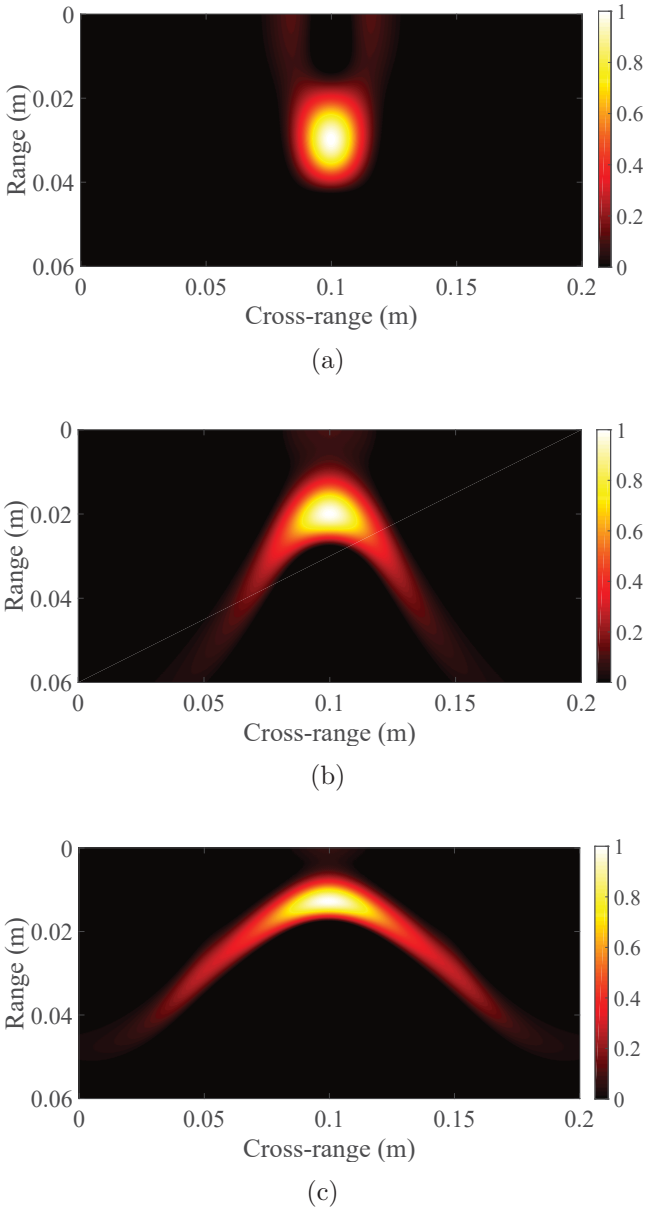

Figure 3.10: Effect of pulse velocity on LSAR reconstructed images: (a) V= $6\times10^8 m/s$, (b) V = $4.5\times10^8 m/s$, (c) V = $3\times10^8 m/s$.

3.6.2 CSAR

The effect of pulse peak velocity on the reconstructed image is even more significant in CSAR. The time domain CSAR method is described in Chapter. 1 and [29,32]. As mentioned in [32] as well, the CSAR image can be focused only if the processing speed is equal to the pulse peak velocity in the medium. The raw data is generated on a circular path with $3cm$ radius. The target is scanned at 72 equally spaced angles from 0 to 2π. The raw data is shown in Fig. 3.11(a). The reconstructed images are shown in Figs. 3.11(b)-3.11(d). The target image is accurately reconstructed in Fig. 3.11(b), with the processing speed of $6 \times 10^8 m/s$. Reconstructed images with a lower pulse peak velocity are shown in Fig. 3.11(c)-3.11(d), which resulted in diverged circles in CSAR images. However, in LSAR images this effect is seen as a vertical offset in the location of the target. The study of pulse velocity effects on

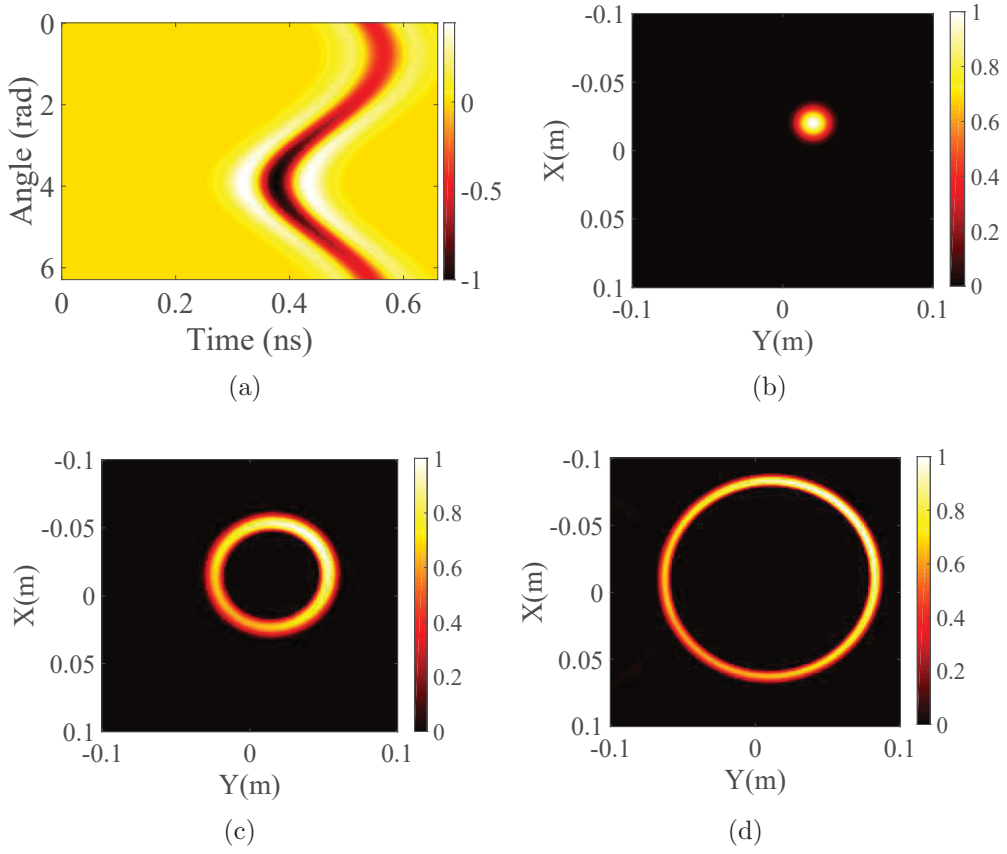

Figure 3.11: (a) Point target raw data. Effect of pulse velocity on CSAR reconstructed images: (b) V= $6 \times 10^8 m/s$, (c) V = $4.5 \times 10^8 m/s$, (d) V = $3 \times 10^8 m/s$.

SAR images demonstrated the necessity of using an accurate value of the pulse velocity for the SAR image reconstruction.

3.7 Experimental Validation of the Effect of Pulse Velocity on Image Reconstruction

This section experimentally validates the effect of pulse velocity on image reconstruction in SAR processing. A target of a small metal strip that measures $2mm$ wide and $12mm$ long, shown in Fig. 3.12(a), is considered in the near-field of the quasi-mono-static UWB radar. The distance between the radar antennas and the metal strip is $5mm$. The detection and imaging of the metal strip is studied through systematic measurements. The radar setup in Fig. 3.12(b) is used to carry out the measurements. The raw data is recorded by scanning the metal strip over an aperture length of $40mm$. The raw data is calibrated by removing the ambient reflections from the received pulses. Further processing of the data for near-field imaging is required which is explained in the following subsection.

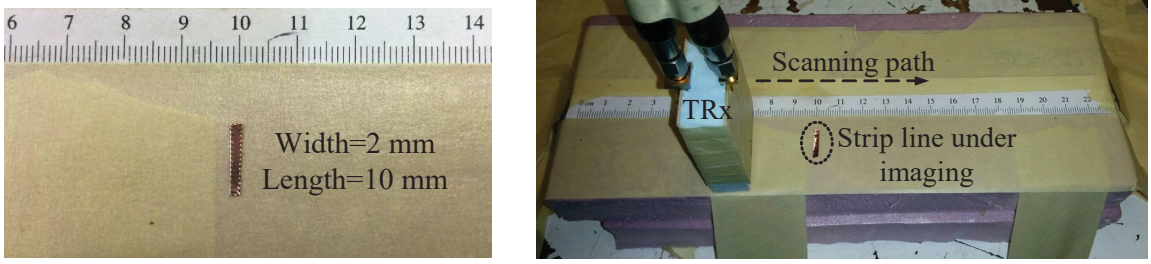

(a) (b)

Figure 3.12: Near-field imaging of a single strip as a small object; (a) single metal strip, (b) radar imaging setup.

3.7.1 Extraction of target signature from the received pulse

The received pulse in the near-field of a radar system is very complicated. It contains the reflected pulse from the target, the mutual coupling between the radar antennas, and the ambient reflections. The transceiver of the quasi-mono-static radar, shown in Fig. 3.13(a), contains a pair of miniaturized antennas separated by $0.5-inch$ thick foam. Mutual coupling between the antennas is analyzed using both simulations and measurements. The electric field coupling between the antennas is shown in Fig. 3.13(b). The simulations have shown that the initial point of coupling along the antenna structure is $14.5mm$ away from the antenna port. The total length of the antenna is $46mm$. Therefore, the point of reference for time delay calculations is $31.5mm$ from the aperture. The location of initial mutual coupling is required to correct the target location in the range direction.

The pulse peak velocity of the pulse is measured by comparing received pulses at different locations very close to antenna, one at the antenna aperture, $SM_{0mm}(t)$, and the other $5mm$ away from the aperture, $SM_{5mm}(t)$. The pulse peak velocity is measured using both the simulations and experiments for the first derivative Gaussian pulse as the input, and is shown in Fig. 3.13(c)-3.13(d) in black and gray dashed lines. The ambient pulse is also measured for calibration and is shown by the solid blue line. The calibrated pulses are shown in solid black and gray lines, $SM_{0mm-cal}(t)$ and $SM_{5mm-cal}(t)$. The pulse peak velocity is also measured by considering different reference points on the pulse, as marked using numbers, and is summarized in Table. 3.1.

Table. 3.1 shows the values of the pulse peak velocity are slightly different for different reference points on the pulse, which is due to the pulse reshaping in near-field. The range of the simulated and measured pulse peak velocities is between $3.37\times10^8 m/s$ and $4.09\times10^8 m/s$. It demonstrates a good agreement between simulations and measurements. To observe the effects of pulse peak velocity, the image is reconstructed by varying the pulse peak velocities between $3.0\times10^8 m/s$ and $4\times10^8 m/s$.

Table 3.1: Pulse peak velocity of Gaussian pulses as input ($V \times 10^8 m/s$)

Location	1	2	3	4	5	6
Simulation	3.4130	3.6364	4	4.09	...	...
Measurement	3.3784	3.4722	3.6996	3.6996	3.8023	3.7037

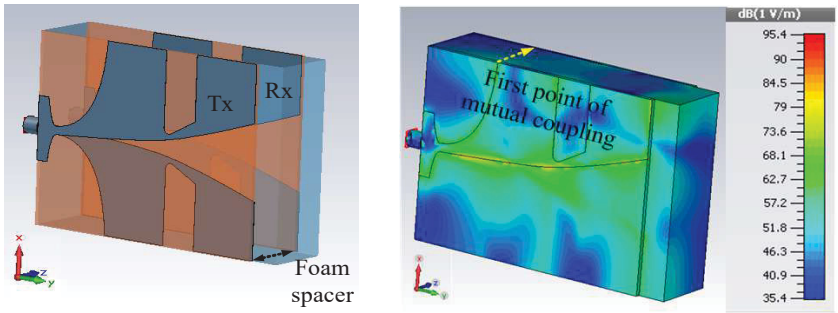

(a) (b)

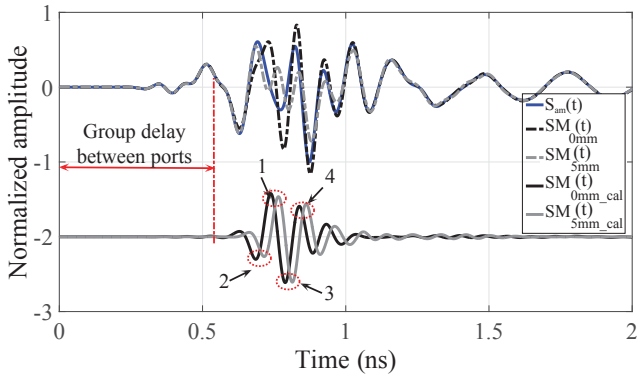

(c)

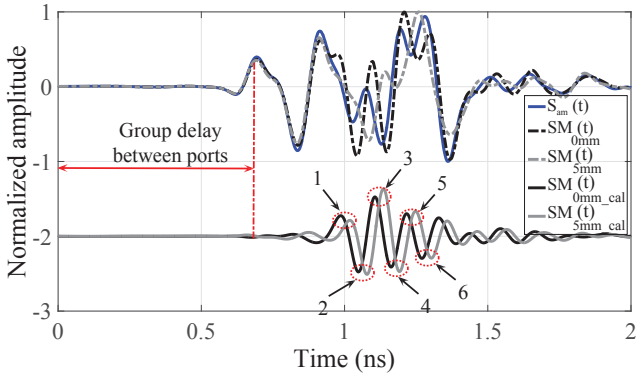

(d)

Figure 3.13: Pulse-timing calibration for image reconstruction; (a) simulated structure, (b) electric-field coupling between Tx and Rx showing the location of first mutual coupling, (c) simulation; first derivative Gaussian pulse, (d) measurements; first derivative Gaussian pulse.

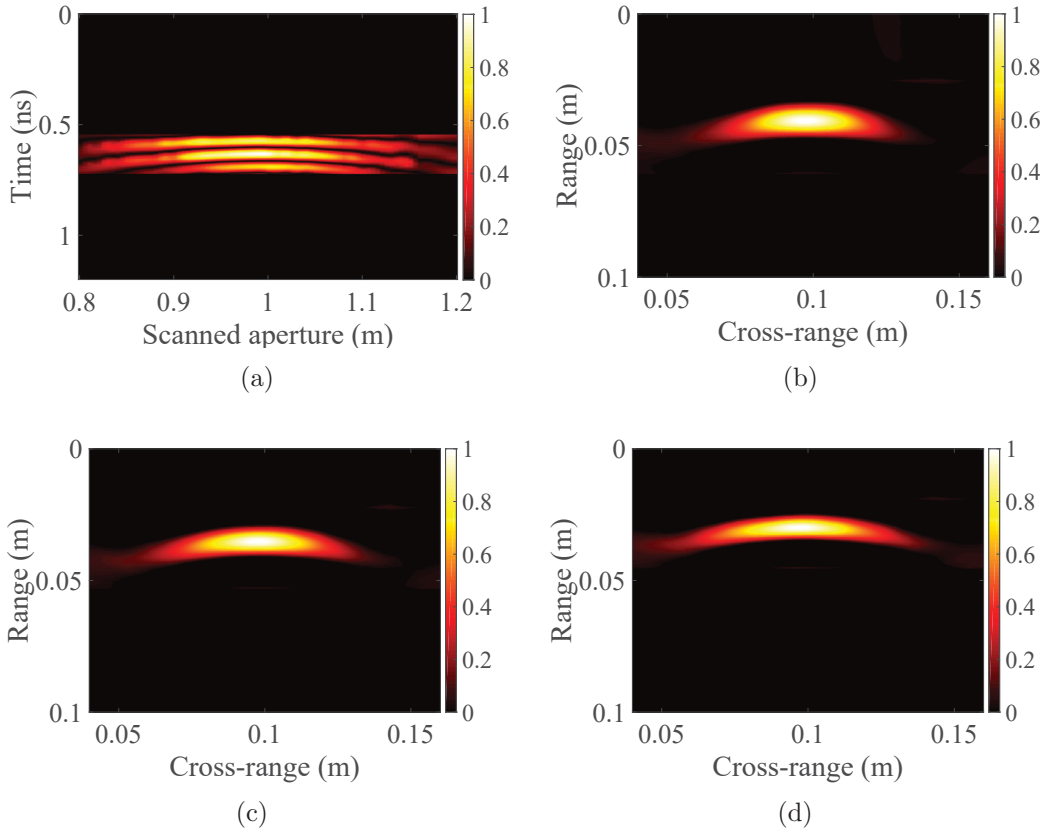

Figure 3.14: LSAR: (a) raw data. The effect of pulse velocity on the reconstructed image: (b) V= 4×10^8 m/s, (c) V= $3.5 \times 10^8 m/s$, (d) V= $3 \times 10^8 m/s$.

3.7.2 Reconstructed images using different pulse peak velocities

The image of the metal strip is reconstructed using different pulse peak velocities and is shown in Fig. 3.14(b)-3.14(d). The raw data, shown in Fig. 3.14(a), is time-gated to eliminate the undesired reflections in the reconstructed image. The reconstructed images suggest that the pulse peak velocity of 4.0×10^8 m/s is more accurate than other pulse velocities as it reconstructs the more focused image. The target appeared at $36.5mm$ as expected in Fig. 3.14(b) which is reconstructed with the right pulse peak velocity. The other two images, reconstructed with lower pulse peak velocities, are distorted and defocused in the cross-range direction.

3.8 Conclusion

This chapter studied the pulse velocity of an electromagnetic pulse radiated by an infinitesimal dipole and UWB antenna. The pulse peak velocity of the radiated pulse, calculated based on the peak, peak envelope and centrovelocity of the pulse, is superluminal in the near-field of the antenna; however, it is luminal in the far-field. The superluminality is verified through the simulations and measurements. Our results showed that the apparent superluminality was due to the pulse shaping of the radiated pulse which does not contradict the casualty. Pulse shaping occurs due to the superposition of different terms of the radiated pulse. This study also included the effect of pulse superluminality on image reconstruction for near-field synthetic aperture radar applications.

Chapter 4

Imaging of Oil-well Perforations using UWB Synthetic Aperture Radar

4.1 Introduction

Oil well monitoring has become an essential approach for oil and gas companies to obtain information about formation evaluation, which is a key indicator in oil well and reservoir management [75]. Aging of oil fields and increasing the cost of drilling new wells demand efficient techniques for monitoring the oil wells to maintain and extend the life of existing wells under operation. Hence the identification and evaluation of novel techniques for oil well monitoring have become an important research topic.

Porous media of the well allow the crude oil into the well along with various byproducts such as water, gas and the other organic materials in the oil sands. Any impairment that affects the permeability of the well adversely affects the production of an oil well. Formation damage of an oil well is indicated by different signs such as well permeability impairment, skin damage, and reduction in oil well performance. Since formation damage is an irretrievable process [76], oil well monitoring on a regular basis should be carried out to avoid deterioration of the oil well performance.

Several techniques have been proposed and developed mainly by oil and gas companies for borehole imaging since 1958. The borehole imaging has started with photography using different lenses [77], ultrasounds [78], micro-resistivity methods [79], and oil based mud imaging tools [80]. Unfortunately, most of these techniques and devices are not able to provide high resolution images to the required depth in the oil well environment. However, it is shown in the literature that GPR can be used effectively to image and characterize the subsurface conditions up to few meters [38, 81–83]. Image resolution of a GPR depends on the bandwidth and the frequency range of the radar system. Borehole imaging radars, a subset of ground penetrating radars, have been extensively used to measure and characterize the physical properties of the formations and layer structures in the neighborhood of a borehole [84–90]. Oil well imaging using borehole radar has been introduced as a promising method to monitor the reservoirs [91–94].

Short pulse radars have been proposed for the high resolution imaging of cracks in concrete casing of a bore well [93, 94]. A combination of UWB-GPR and SAR principles were also proposed in [27] to generate high resolution images of oil wells.

In this chapter we propose a UWB-SAR to image the oil well casing to determine the impairments that leads to the perforation clogging, which reduces the oil well production. Perforation monitoring by periodic scanning of oil well provides the status of asphalt and other organic material filling in perforations, hence the problem can be localized and mitigated using solvents [95] at early stages to save the oil well. Indeed, imaging of oil well perforations is very complicated due to the narrow diameter of the bore well [96]. Imaging in near-field along with the effect of oil well curvature on signal propagation made the task even more challenging.

In this chapter the concrete cased oil well construction details, measurement setup and pulse calibration in the oil well is presented first. Then the group velocity of the pulse propagating inside the concert cased oil well is investigated. The imaging of pipe perforation in air, a proposed modifications method for reconstructing high quality images and imag-

ing of perforations in oil well in the presence of sand, oil and other objects is presented, subsequently.

4.2 Oil well Structure and Measurement Setup

In this section the details of the oil well structure and the UWB radar system for oil well monitoring are described.

4.2.1 Oil well structure with concrete casing

An oil well is a relatively deep borehole into the ground to reach the underground oil and gas reservoirs. The typical oil well diameter decreases as oil well gets deeper. It starts from $100cm$ at the ground surface and reduces to $20-25cm$ at the deepest region of the oil well, called the production zone. The oil well depth depends on the nature of the mine, and it can vary from hundreds of meters to a few kilometers. Oil well casing can be metallic or concrete, or combination of the both depending on the subsurface conditions and depth of the oil well. Casing fortifies the well wall and at the same time prohibits oil contamination with the sub-surface water resources. In this case study, we considered the oil well whose

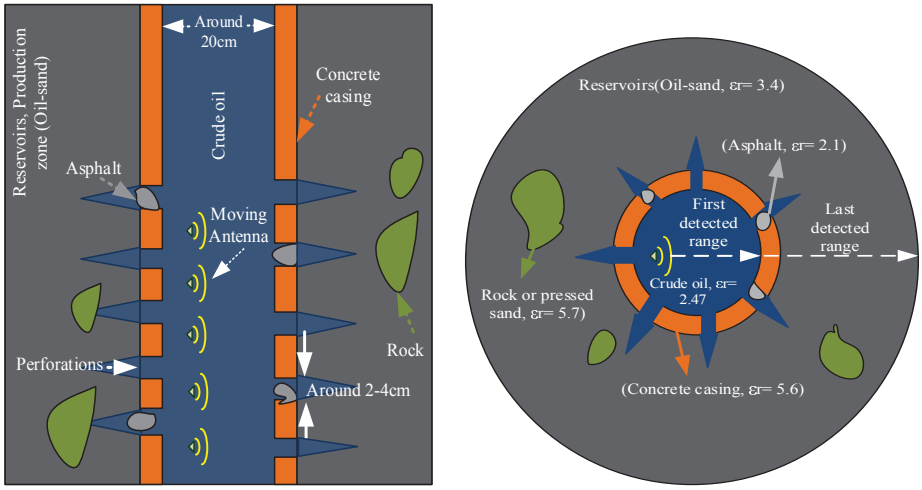

Figure 4.1: Concrete cased oil well model; (a) side view, (b) cross section.

production zone is cased with concrete. In the production zone, concrete casing is perforated to allow the oil and gas flow into the oil well as shown in Fig. 4.1. Perforation diameter varies from $2cm$ to $4cm$ depending on the depth and type of oil well [96].

As shown in Fig. 4.1, oil well production zone contains different materials such as asphalt, rocks, sand, and some organic materials. Near to the bore hole is the porous media that lets the oil flow into the well. One of the materials that are always found in the oil well is asphalt or bitumen that can be problematic in case of choking off the perforations as shown in Fig. 4.1. Different perforation conditions such as open, partially or completely clogged are also shown in this figure. In case of clogging, the oil well production decreases dramatically. Therefore periodic monitoring of oil well is crucial for oil well maintenance and extending the oil production.

Different materials found in the reservoir have different dielectric constant that makes them electrically distinctive. The discontinuity in electrical properties can be exploited by radar principles. To scan the oil well production zone in three dimensions the medium should be scanned along the well axis and azimuth plane. To do this, the radar has to be moved upward or downward along the well axis in one angle to provide the scan for a well slice, then by rotating the radar to other angle and moving up or down another slice is scanned as demonstrated in Fig. 5.1. Arranging all the slices corresponding to different angles provides the oil well image in three dimensions.

In this work, the oil well is scanned only for one slice to create 2D image. Due to the narrow diameter of the oil well, imaging has to be done very close to the antennas, in antenna near-filed, which makes data interpretation more challenging. To investigate the capability of radar imaging technology for oil wells, extensive experimental studies have been conducted in this chapter and next one.

4.2.2 Measurement setup

The measurement setup contains a UWB radar and a concrete pipe to emulate the oil well as shown in Fig. 4.2(a). The UWB radar systems demonstrated in chapter. 1 is used to carry out the measurements. Two TEM horn antennas customized for oil well monitoring on a wooden holder [33,34] as shown in Fig. 4.2(b) are used for this experiment. These antennas operate in the frequency range of 2.2 to 18GHz in air; however, due to the loading of crude oil the operating frequency of the antenna shifts to 1.4 to 11GHz. The UWB operation of these antennas from low frequencies to high frequencies provides high-resolution in the range direction and at the same time good penetration depth.

The oil well is modeled by a concrete pipe with diameter of 17cm and thickness of 2.5cm with couple of perforations along its wall as shown in Fig. 4.2(a). Radar position in the

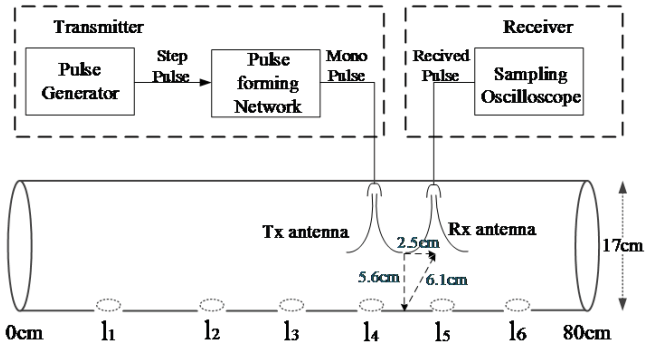

(a)

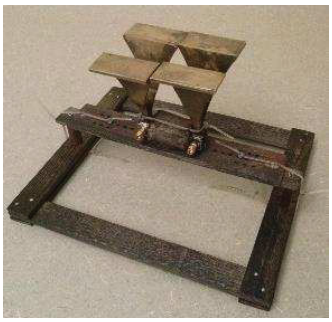

(b)

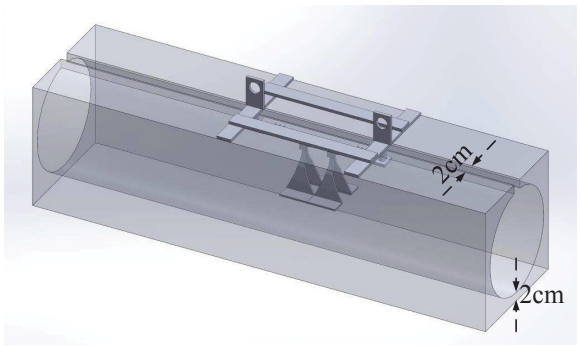

(c)

Figure 4.2: (a) Measurement setup and pipe perforation locations, (b) Tx and Rx antennas on a wooden holder, (c) concrete pipe and radar position.

concrete pipe is shown in Fig. 4.2(c). To make the measurement setup simpler, a slot is cut in the concrete pipe to support antenna holder move along the axis of the pipe. The distance between the antennas and the wall surface is $5.6cm$. The Tx and Rx antenna center to center distance is $5cm$ which makes the distance between the antenna aperture and point of reflection on the wall $6.1cm$ as shown in Fig. 4.2(a). Dimensions and locations of the pipe perforations are shown in the Table. 4.1.

Table 4.1: Concrete pipe perforations dimensions

Perforation number	P_1	P_2	P_3	P_4	P_5	P_6
Perforation diameter (cm)	$d_1 = 3$	$d_2 = 3$	$d_3 = 3.4$	$d_4 = 4$	$d_5 = 3$	$d_6 = 3.5$
Perforation location (cm) from one end	$l_1 = 7$	$l_2 = 20$	$l_3 = 32$	$l_4 = 45$	$l_5 = 55$	$l_6 = 68$

4.2.3 Calibration of the received pulses

In order to obtain the target information, which is the concrete pipe shown in Fig. 4.2(c), other effects have to be eliminated from the received pulse as explained in the Chapter. 1. The calibration procedure to calibrate pulses reflected by the concrete pipe is shown in Fig. 4.3. The ambient pulse is measured by transmitting and receiving the pulse into medium of propagation, which is air here, with no object in front of the antennas. As can be seen from Fig. 4.3 , for illustration purpose the pulses are offset along vertical axis, the received pulse and antenna mutual coupling resemble each other up to $1.4ns$, where the target signal has not appeared yet. The calibrated pulses is used for signal processing and image reconstruction as described in the following sections.

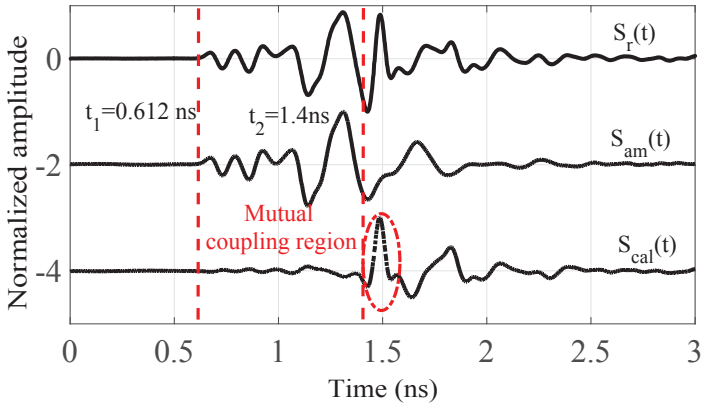

Figure 4.3: Calibration process of the received pulse

4.3 Group Velocity of the Pulse in Concrete Pipe

Group velocity of the pulse plays a crucial role in radar signal processing and image reconstruction methods specifically in range determination. Depending on the dielectric constant of the wall and operational frequency, the concrete pipe may behave like a waveguide. Consequently electromagnetic wave propagating inside the concrete pipe could have different group velocity than in free space. To evaluate the group velocity, wave propagation in the concrete pipe is studied in this section. Group velocity was evaluated by full wave simulation as well as from the measurement data. Both approaches are described here.

The full wave simulations for group velocity calculation inside the concrete pipe are carried out by CST microwave studio [57]. The dielectric constant of the pipe is assumed as 5.6, as it is a dry concrete [57]. The simulated pipe structure is shown in Fig. 4.4(a). The Rx antenna receives the signal due to mutual coupling and the reflected pulse from the concrete pipe. The group velocity can be calculated as follows:

$$G_v = \frac{R_t}{t_2 - t_1} \tag{4.1}$$

where t_1 and t_2 are time references for Rx antenna starting to receive energy due to antenna mutual coupling and concrete pipe reflections respectively. Therefore round trip time can be calculated by subtracting t_1 from t_2.

Since the bi-static distance, R_t, between first location of mutual coupling point along the antenna and the concrete surface is known, the group velocity can be evaluated by having the round-trip time. Round-trip time is defined as time taken by the pulse from the Tx antenna to hit the concrete surface and to be received by the Rx antenna. Since the target is very close to the antennas, a reference location for mutual coupling point has to be taken into account in the round trip path calculation. The mutual coupling between the Tx and Rx antennas, due to the nature of TEM horn antennas, is not only through the antenna apertures but also through the antenna structure.

To estimate the location of initial mutual coupling, the radar transceiver shown in Fig. 4.4(b) is analyzed. The coupled electric field and power flow at $7GHz$ ate also shown in Fig. 4.4(c)-4.4(d). The mutual coupling starts while the wave is still being guided by the TEM antenna flares. Studying the electric field and power flow configuration between Tx and Rx antennas demonstrates that mutual coupling started before the antenna aperture, about $2cm$ after feed point. Hence the round trip distance is estimated by:

$$R_t = 2\sqrt{(l_e + d)^2 + (\frac{p}{2})^2} \tag{4.2}$$

where l_e, d and p are mutual coupling length, distance from antenna aperture to target, and center to center distance between Tx and Rx antenna apertures respectively. The simulated received and mutual coupling pulses are plotted in Fig. 4.4(e), where t_1 and t_2 are marked on the graph. For the values of $d = 5.8$ cm, $p = 5$ cm and $l_e = 5.6$ cm from simulated structure, R_t became $23.34cm$. Therefore, the estimated group velocity is $2.9142 \times 10^8 m/s$. It is observed from the simulation results that the concrete pipe affects the group velocity. The group velocity is also calculated from measurements inside the concrete pipe.

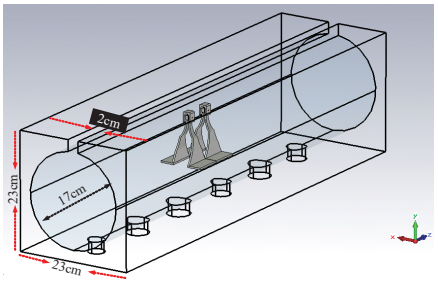

(a)

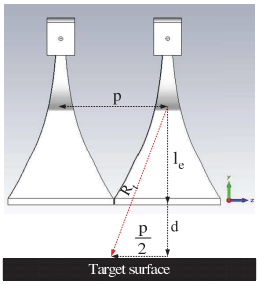

(b)

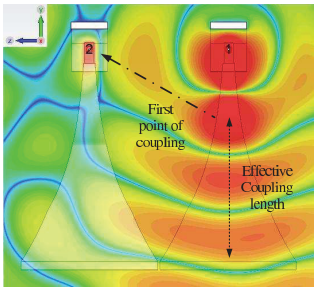

(c)

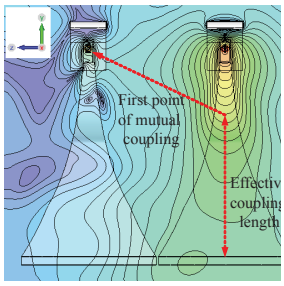

(d)

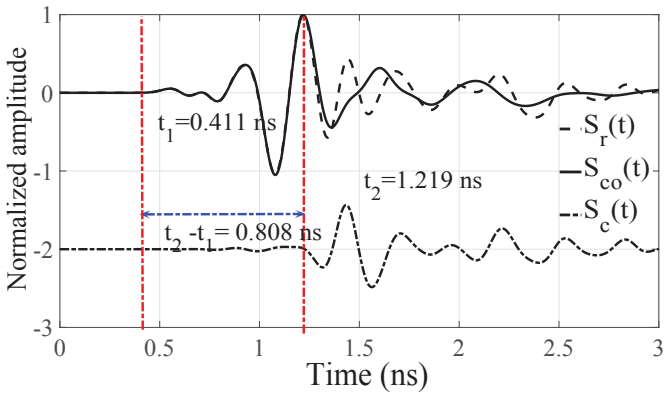

(e)

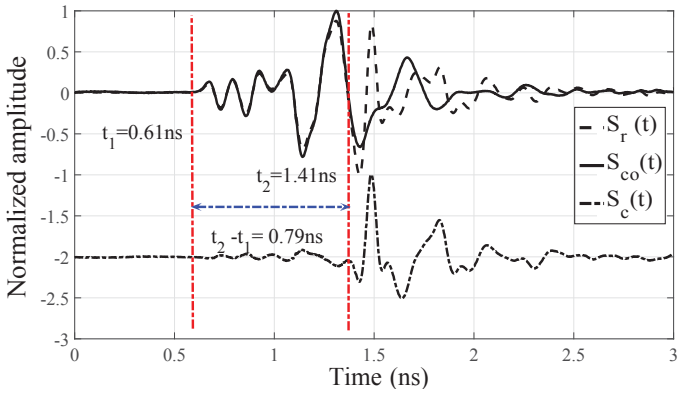

(f)

Figure 4.4: (a) Simulated oil well pipe, (b) Tx and Rx antennas, (c) electric field coupling between Tx and Rx antennas, (d) power flow between Tx and Rx, (e) simulated received and calibrated pulses, (f) measured received and calibrated pulses.

Measured pulses are plotted in Fig. 4.4(f). Considering the dimensions of measurement setup and the measured pulses, the group velocity is calculated as $2.9376 \times 10^8 m/s$. As can be observed there is a very close agreement between measured and simulated group velocities. The group velocity calculated from the measurement results has been used for signal processing in the next section.

4.4 Imaging of Perforations in Air

Different measurement scenarios have been considered to examine the ability of UWB radars for imaging pipe perforations in a concert cased oil well. Measurements are started with a simple case, which is imaging of concrete pipe in the air. The measurement setup shown in Fig. 4.2(a) was used to scan the pipe in the air. Fig. 4.5(a) illustrates the pipe interior and antennas position inside the pipe. The raw data was acquired by moving the antennas along the pipe axis facing towards the perforations as shown in Fig. 4.5(a). Scanning was done for every $0.5cm$ over the length of the pipe. To improve the signal to noise ratio of the received pulse, time averaging over 60 pulses was applied. The received pulses, raw data, is plotted and shown in Fig. 4.5(b). The raw data after calibration is shown in Fig. 4.5(c). The horizontal red line in Fig. 4.5(c) shows the run-time taken by the pulses to hit the inner concrete surface. The detected perforations appear as shallow dents and are marked in the raw data. To acquire further information about the scanned structure, the calibrated raw data was processed. An image of the concrete pipe is reconstructed with LSAR method and is discussed next.

4.4.1 SAR processing of the measured data

The calibrated raw data is processed by LSAR technique to obtain a 2D image in spatial domain. The image is reconstructed in x and z directions along the well axis and depth, correspondingly. Here M and N are selected as 1300 and 800 for number of pixels in the

reconstructed image.

(a)

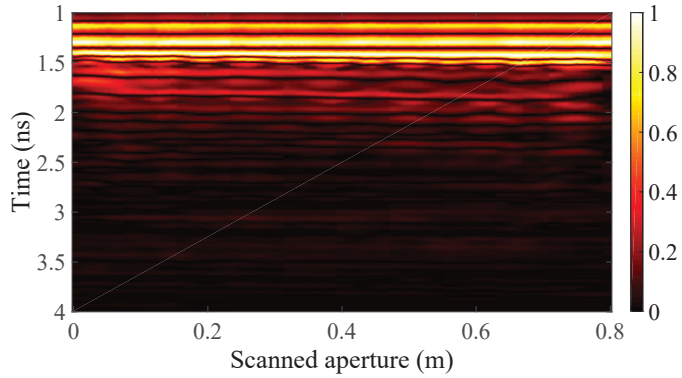

(b)

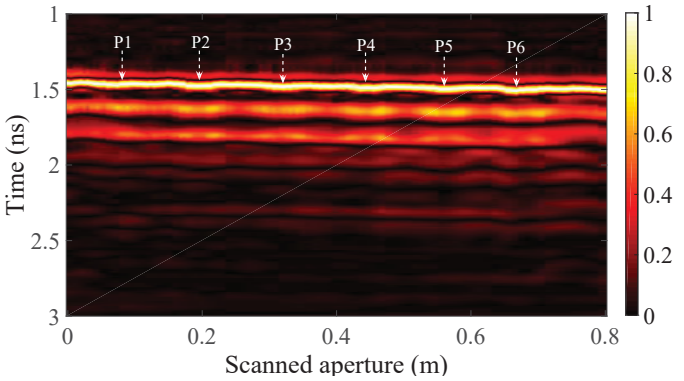

(c)

Figure 4.5: Pipe imaging in free space; (a) concrete pipe interior view, (b) measured raw data, (c) calibrated raw data.

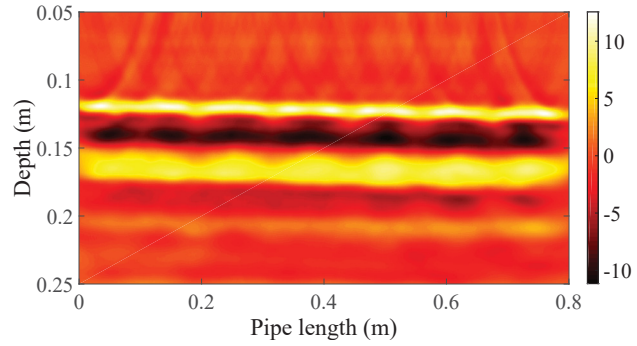

(a)

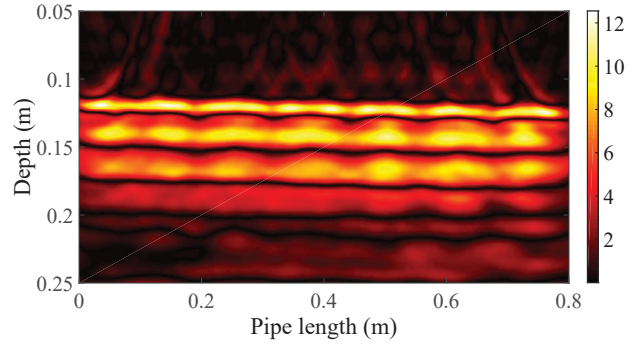

(b)

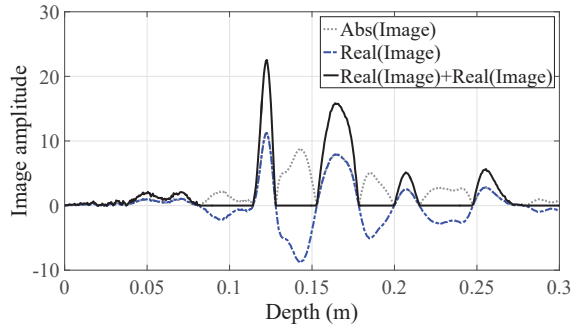

(c)

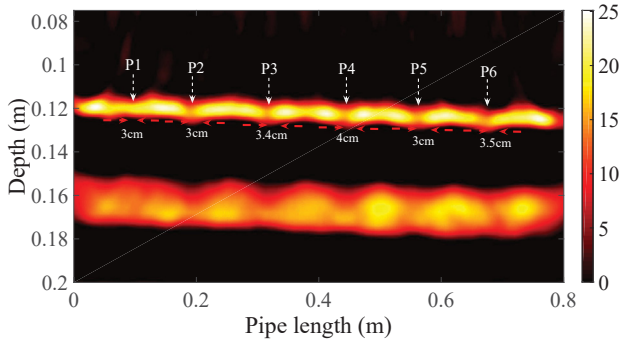

(d)

Figure 4.6: (a) Image real (instant) value, (b) image absolute value, (c) positive image method, (d) modified positive image imaging.

The real and absolute quantity of the constructed image is shown in Figs. 4.6(a)-4.6(b), respectively. It is known that concrete pipe thickness is about $2.5cm$. As can be seen, significant reflections appeared around $12cm$ and $15cm$ in the image, where the pulse hits the concrete surface and leaves the concrete wall as shown in Figs. 4.6(a)-4.6(b). By comparing these two figures, it appears that there are some reflections during the time the pulse is propagating through the concrete across its thickness. It is a known fact that there should not be any reflections as there is no discontinuity within the concrete wall. These reflections appeared due to the negative cycle of the transmitted pulse. The reconstructed image has contributions from both positive and negative parts of the pulse which can be separated. By considering this fact, we extracted the image that corresponds to the only positive part of the pulse, which improves the image sharpness. The positive image was generated by keeping the positive values of the image and setting its negative values to zero or by summing up the real and absolute value of the image as follows:

$$Image_{Positive} = Re(Image) + Abs(Image) \tag{4.3}$$

The summation of the real and absolute value of each vertical row (along the depth direction) of image is added to achieve positive image. Fig. 4.6(c) demonstrates the procedure for one of the rows of the positive image. After the summation, the negative part of the image is cut and the positive part got doubled. Since the negative cycle of Gaussian mono pulse is removed in the positive image, the proper time delay which is half of pulse width should be considered in the image reconstruction process for correct target location. The positive image is shown in Fig. 4.6(d). It can be observed that by this procedure the image quality is highly improved and all perforations except the first one, which is $7cm$ from the edge, are detected in the reconstructed image.

4.4.2 Magnification of images by increasing signal speed in SAR processing

In the previous section, SAR processing of the raw data to detect the perforations was demonstrated. The effect of signal speed on image quality constructed by SAR processing is studied here. In this experiment the distance between the antenna aperture and target is very short, which limits the antenna illumination area on the concrete surface. Hence entire target (all perforations) cannot be scanned from the radar position. Therefore the advantage of synthesized aperture could not be exploited to the fullest extent.

Magnification of the reconstructed image may provide more details and better resolution about the target. Here we propose a technique for magnification of the reconstructed image by artificially increasing the signal speed in processing. According to Eq. 1.3 the time interval between picked samples, from the received signal, can be altered by changing the signal speed in SAR processing.

The image magnification procedure by increasing the signal speed is illustrated in Fig. 4.7(a). For a given number of pixels and spacing between them, there would be a corresponding sample on the received pulse from each aperture position. In other words, every sample on the received pulse corresponds to an arc on the image space. For a fixed pixel size (Δz and Δx) in image reconstruction, increasing the signal speed results in picking samples in shorter time intervals ($\Delta t_2 < \Delta t_1$). In this process the reconstructed images get stretched and more samples would be included. For example as shown in Fig. 4.7(a), information of the image increased from 6 pixels to 10.

Further magnification, i.e. increasing the signal speed to higher values to reconstruct an image of a given size may look bad due to overspreading. This processed has been verified by selecting various signal speeds. It was shown that for this data set, imaging of concrete pipe in air, the signal speed of $3.5 \times 10^8 m/s$ is an optimal value to acquire a better image quality.

The reconstructed images with measured group velocity and increased signal speed are il-

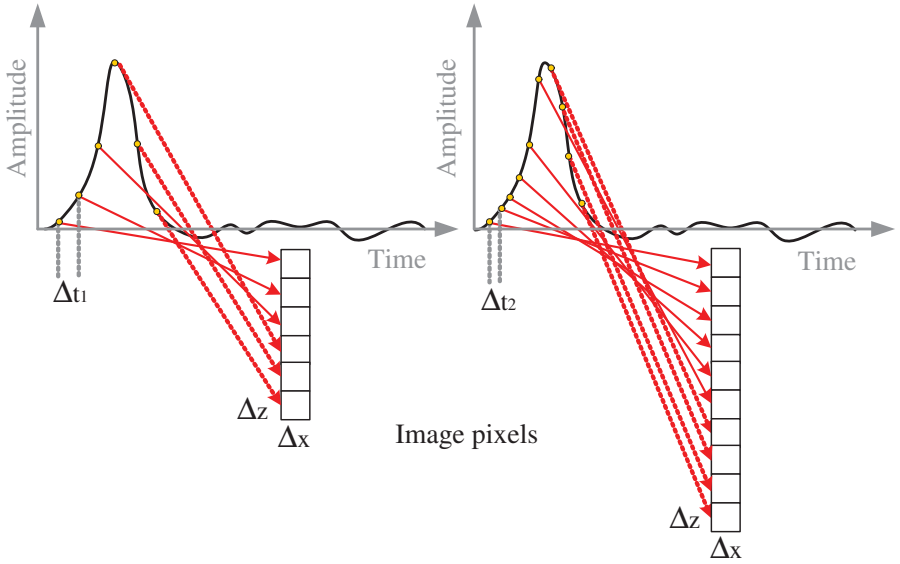

(a)

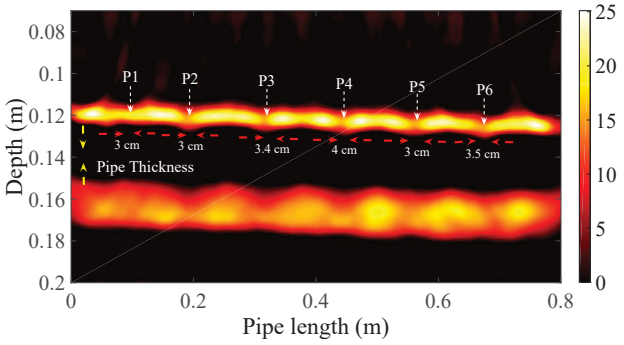

(b)

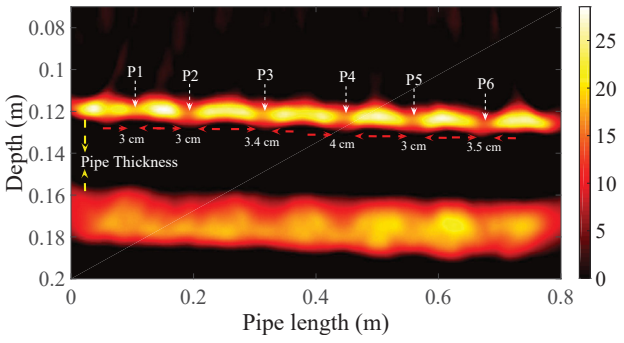

(c)

Figure 4.7: Reconstructed image; (a) $G_v = 2.9376 \times 10^8 m/s$, (b) $V_s = 3.5 \times 10^8 m/s$.

lustrated in Fig. 4.7. As can be seen in Fig. 4.7(c), the pipe perforations are clearer in

comparison with Fig. 4.7(b). The image magnification factor (IMF) is defined as:

$$IMF = \frac{V_s}{G_v} \tag{4.4}$$

For a signal speed of $V_s = 3.5 \times 10^8 m/s$ and $G_v = 2.9376 \times 10^8 m/s$ the magnification factor is 1.19. This is clearly illustrated in Fig. 4.7. For example the thickness of the concrete wall, at $10cm$ location, from Fig. 4.7(a) is 2.65 cm while in Fig. 4.7(b) it is $3.22cm$ which confirms the magnification factor. It is shown that increasing the signal speed, even though it is not practical, in time domain SAR processing for image reconstruction can generate more informative images.

4.5 Imaging of Pipe Perforations in the Presence of Sand, Oil, and Other Objects

Different measurement scenarios are considered here to investigate the effect of nearby media such as sand and oil on imaging of pipe perforations.

4.5.1 Imaging of pipe perforations in the presence of dry sand

Here it is considered a concrete pipe is placed in a plastic container filled with dry sand of depth $8 - 9cm$ as shown in Fig. 4.8(a). The side gaps between the concrete pipe and the plastic container is also filled with dry sand. Due to the dimensions of antenna holder and plastic container the measurements are carried out from $6cm$ to $73cm$ from the left end of the pipe. The raw data after calibration is shown in Fig. 4.8(b). The raw data is processed as explained in the previous section. The signal speed of $3.5 \times 10^8 m/s$ resulted in better image for this data set as well. The reconstructed image is plotted in Fig. 4.8(c) . As can be seen all perforations are detected in the image. The image in Fig. 4.8(c) can be compared with the image in Fig. 4.7(c). It proves that pipe perforation can be imaged in the presence

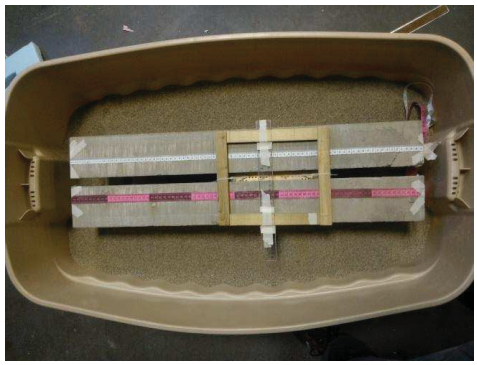

(a)

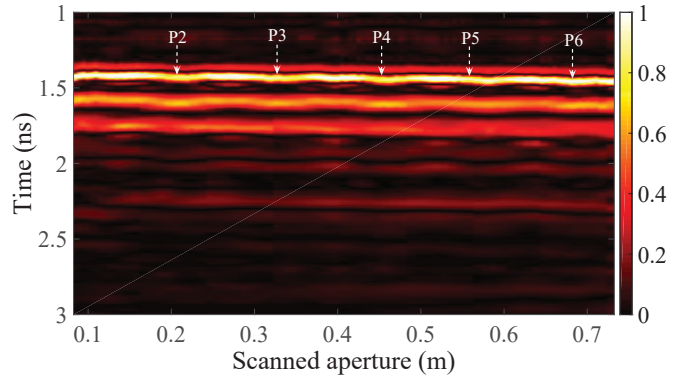

(b)

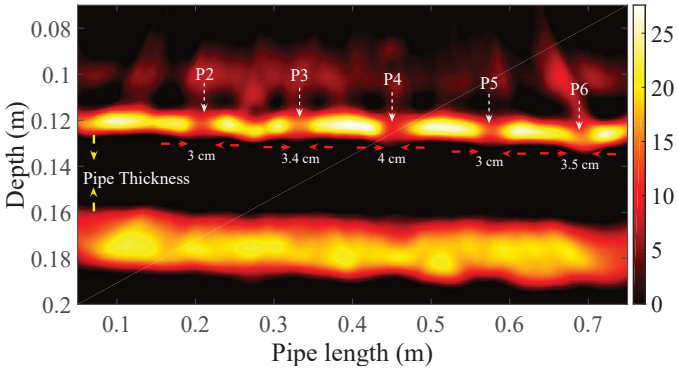

(c)

Figure 4.8: (a) Pipe being imaged in presence of sand, (b) calibrated raw data, (c) reconstructed image.

of sand as well.

The objective of this study is to explore the feasibility of using UWB-SAR for oil well perforation monitoring. Therefore we have considered different scenarios starting from a simple case and extended it by adding different aspects. In this experiment oil is added to

the container to emulate the oil well production zone as shown in Fig. 4.9(a). The oil mix in the container is a combination of crude oil and diesel, 40 liters of crude oil and 25 liters of diesel, as crude oil was not sufficient to fill the container. The crude oil permittivity, measured with the Agilent probe, is 2.47 while white diesel permittivity is 2.5 [57]. Hence, adding diesel would not affect the crude oil electrical properties.

For the final stage of this study two scenarios were considered during the measurements, one with all perforations open and the other with some perforations partially and some completely clogged. The measurement in the second scenario was carried out by placing the objects shown in Figs. 4.9(b)-4.9(d) inside the perforations. The second perforation (P_2) was partially clogged by asphalt powder from outside, Fig. 4.9(b), which was packed in a plastic bag. The fourth perforation (P_4) was partially clogged and fifth perforation (P_5) was completely clogged with slim and fat Teflon cylinders, shown in Figs. 4.9(c)-4.9(d), respectively. The ambient pulse in oil could not be measured with our lab facilities. Ambient pulse measurement in small container is not accurate due to the reflections from the boundaries. Therefore, time gating is applied to remove the ambient pulse or antennas'mutual coupling in oil . Using time gating of the raw data, strongest part of antenna mutual coupling which occurs before the first reflection from the concrete surface was removed. The raw data after time gating is shown in Figs. 4.10(a)-4.10(b). The red line shown in these plots is due to the reflection from the concrete surface, therefore to eliminate the mutual coupling the data before this time step is replaced with zeros.

It can be seen from the raw data, Figs. 4.10(a)-4.10(b), the perforations appears as shallow dents. However, comparing Figs. 4.10(a)-4.10(b), some changes in perforation conditions can be identified. The most significant change appeared at the P_5 location in Fig. 4.10(b) compared to Fig. 4.10(a), there is a dent in Fig. 4.10(a) and no dent in Fig. 4.10(b). It indicates that P_5 is clogged. The group velocity in oil is less than in air, which is $1.857 \times 10^8 m/s$ for oil permittivity of 2.47.

Quality images are generated for magnification factor of 1.6. The reconstructed images

(a)

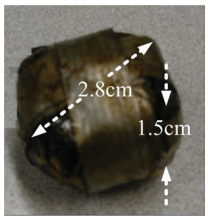

(b)

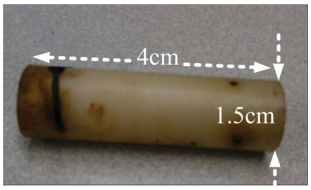

(c)

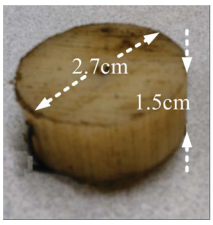

(d)

Figure 4.9: (a) Emulated Oil well, (b) packed asphalt, (c) slim Teflon cylinder, (d) fat Teflon cylinder.

for these two experiments are shown in Figs. 4.10(c)-4.10(d). As can be seen P_5 is shown clogged in the reconstructed image. There are some other changes around P_2 and P_4, due to asphalt and pieces of Teflon which were placed inside the perforations. However these are not as clear as P_5. The close observation of the images shown in Figs. 4.10(c)-4.10(d) suggests that there might be an obstruction on the outer side of the pipe perforations P_2 and P_4. Another way of investigating the condition of pipe perforation is studying the pulses across the perforation. The pulses over these two perforations are shown in Figs. 4.11(a)-4.11(b). As it can be seen in Fig. 4.11(a), pulses for the open and clogged scenarios are almost the same except around the time where pulses hit the perforation which is highlighted by the red circle. The measured dielectric constant and loss tangent of the asphalt are 2.1 and 0.05 respectively [27]. The reflected pulse from P_2, in the clogged condition, is almost the same as the pulse from open condition; however the difference shown in the circle, in Fig. 4.11(a), is due to the high loss of asphalt.

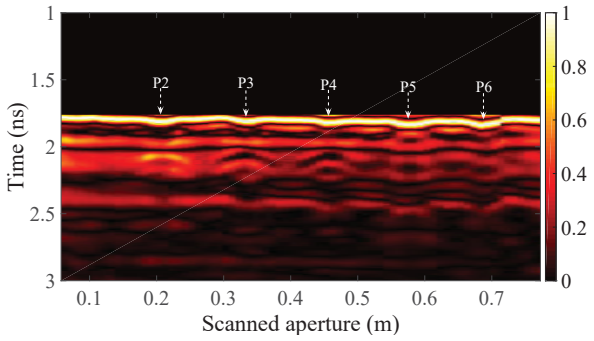

(a)

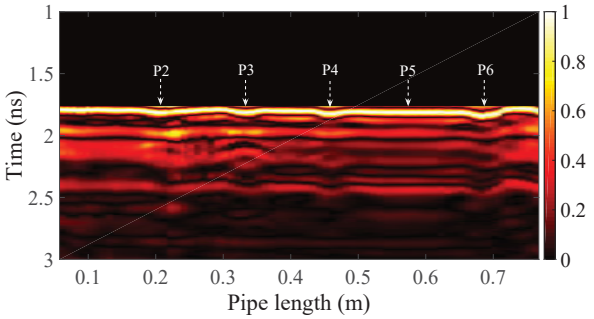

(b)

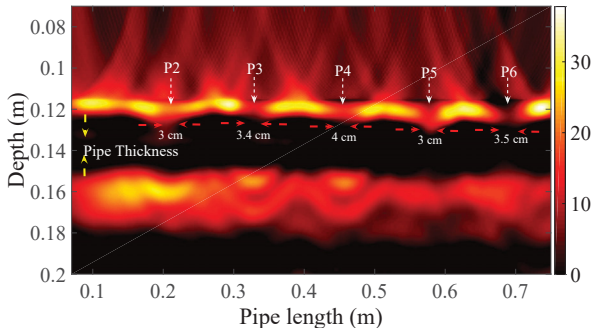

(c)

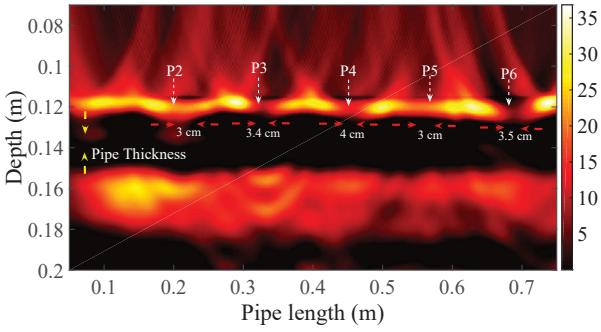

(d)

Figure 4.10: Time gated raw data; (a) open perforation, (b) partially and fully clogged perforation. Reconstructed images; (c) open perforations, (d) partially and clogged perforation.

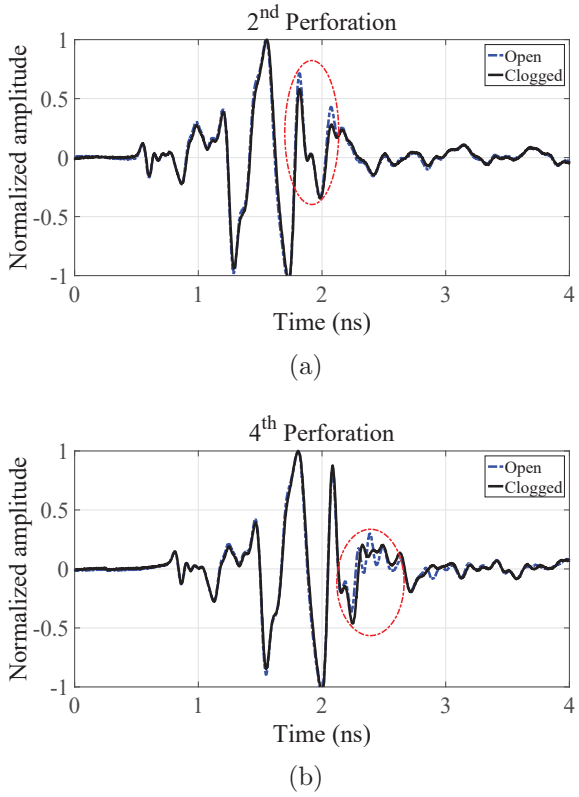

Figure 4.11: Comparing pulses at the center of perforation for open and clogged states; (a) 2^{nd} perforation, (b) 4^{th} perforation.

The difference in the reflected pulses from the perforation P_4, shown in Fig. 4.11(b), is due the dielectric material in the perforation. These experiments demonstrate the ability of UWB radar technology for oil well monitoring.

4.6 Conclusion

The capability of UWB synthetic aperture radar imaging for monitoring concrete-cased oil wells was demonstrated in this chapter. The raw data was acquired by the UWB radar system and processed using LSAR algorithm for image reconstruction; and ways of extracting the information of the oil well perforation in different conditions were studied. The method was evaluated through different experimental conditions which resulted in very useful and informative images. Regular scanning of oil wells by the introduced method will provide

necessary information for oil well management and maintenance.

Chapter 5

Metal-Cased Oil Well Inspection using Near-Field UWB Radar Imaging

5.1 Introduction

Radar imaging has recently been adapted for oil well monitoring applications [41, 93, 97]. In our previous work [41], introduced in the previous chapter, we investigated the possibility of using UWB-SAR systems to image the perforations of a concrete-cased oil well. The UWB-SAR system could effectively image the perforations, and estimate the clogging level of perforations due to the presence of asphalt or other organic materials.

In this chapter we have extended the application of the UWB-SAR for inspection of th metal-cased oil wells. This inspection includes imaging of the oil well perforations, and identifying fractures and breakouts caused by stress. Indeed, it is considered very challenging to use radar principles to detect and image a small anomaly, such as perforation or corrosion, on the surface of a metal-cased oil well. The challenges include strong reflections from the metal case that masks the small anomalies, and also the narrow diameter of the oil well [96], which forces the imaging to be done in the near-field of the radar system. We have investigated the pulse propagation in the near-field and its characteristics in the presence

of metallic surfaces with and without perforations. Pulse characteristics and its speed, corresponding to time delay, in the radar near-field [98] are effectively used to detect and image small perforations on the surface of a metal-cased oil well. We have observed both numerically and experimentally that the presence of an anomaly in a metal background creates an extra time delay, in addition to the round trip time, which is a key for detection of a small anomaly.

This chapter first describes the metal-cased oil well structure and the proposed UWB radar system with an automated scheme for data collection inside oil well. The antenna structure used to perform these experiments and it's radiated pulse characteristics in the oil medium is also explained in the same section. Next section presents the study of characteristics of the reflected pulse, such as pulse shape, pulse arrival time, and time delay, in the radar near-field for different scenarios of metal plates and perforations. Detection and imaging of oil well perforations of different diameters, and anomalies due to corrosion on the emulated oil well surface are studied in the following sections. The imaging is carried out for the cases with and without the presence of oil/diesel.

5.2 Metal-cased Oil well Structure and UWB Radar System

5.2.1 Metal-cased oil well structure

Most of the Oil wells are reinforced with both concrete and metal casings as shown in Fig. 5.1. The oil well casing is perforated in the production zone to let the oil into the bore-hole. The oil well diameter in the production zone is about 20 cm, or less, and the perforations' diameter varies from $1cm$ to $4cm$ for different oil wells [96]. The condition of the perforations changes over time and the information about perforations' condition, such as breakouts due to stress, clogging, and corrosion, is extremely valuable for oil well maintenance. Here we

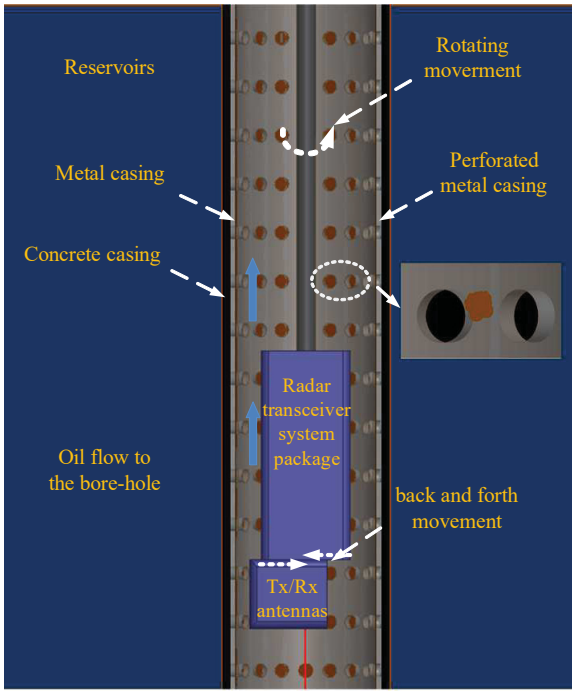

Figure 5.1: Metal-cased oil well production zone.

study the possibility of using UWB radar to monitor metal-cased oil well perforations and corrosion. The data collection scheme in an oil well is shown in Fig. 5.1 as well. To acquire the data from an oil well, the radar system can be screwed to the shaft to be taken down the borehole to the perforation zone.

To obtain raw data at different depths and angles, rotational and vertical moves are required. The transceiver distance to the well wall shall be adjusted by horizontal movement. The radar transceiver should be packaged, to prevent unwanted interferences, with limited dimension that fits inside the oil well. The radar system will be capable of operating on battery as the distance to the target is very short. The oil well monitoring can be done in either off-line or near-real time scenarios. In the first case, the raw data is collected by radar and stored in a memory, taken up, and processed. In the second case, the raw data is sent to the ground station through data cables and processed in a near real-time mode.

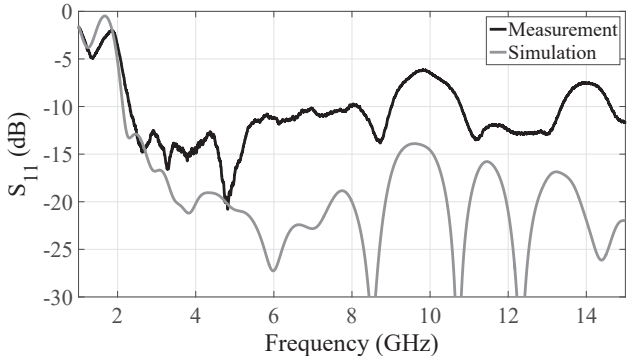

Figure 5.2: Antenna return loss measurement and simulation inside diesel.

5.2.2 UWB radar system and miniaturized antipodal Vivaldi antenna as the EM sensor

To conduct the experiments, the UWB radar system shown in Figs. 1.6(a)-1.6(b) along with the Vivaldi antenna, shown in Fig .1.7(b) and dimension are given in Fig. 3.3, customized to operate within the medium of a dielectric constant of 2.5 [35], are employed. The antenna is characterized in both frequency and time domain within the medium of crude oil and diesel. Crude oil with a dielectric constant of 2.33 [57] is used during the simulations; however, the dielectric constant of crude oil can range from 2.2 to 2.6 [27]. Since crude oil is not easily accessible, measurements are completed using diesel. Diesel has dielectric properties very similar to that of crude oil, measured by Agilent dielectric, as already mentioned in the previous chapter and is about 2.5 over the operational bandwidth.

For antenna characterization, the antennas are completely immersed in diesel. The frequency domain measurements are done using an Agilent VNA $8362B$. Antenna return loss for both the simulations and measurements is shown in Fig. 5.2. Both the simulated and measured reflections follow the same trend; however, the measured return loss is degraded at higher frequencies which can be due to the smaller size of the container ($30cm \times 30cm \times 25cm$). However, the measured return loss is below $10dB$ for most of the frequencies, 2 to $9GHz$. The designed antenna has realized gain of 4 to $8dBs$ from lower frequency band to the higher frequency band.

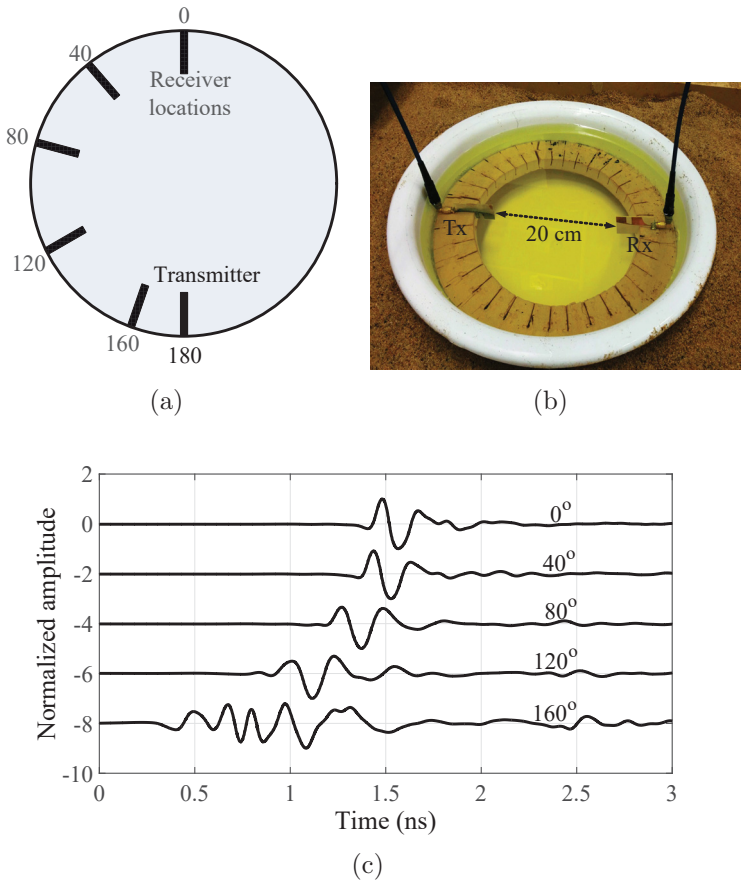

Figure 5.3: (a) Pulse measurement schematic, (b) pulse measurement setup, (c) measured pulse at different angles.

Time domain measurements of the radiated pulse are performed to evaluate pulse distortion at various angular positions. Since the antenna is intended to operate in an oil well, facing the well wall, the measurements are done on a circular path as shown in Fig. 5.3(a)-5.3(b), where antennas are positioned face-to-face. The transmitter is located at 180° and the receiver is moved from 0° to 160° for every 40° step. Up to 40° , the pulse shape is very well preserved. At 80° and 120° , the pulse shape is slightly degraded but still in a decent shape, suitable for imaging applications. However, at 160° , the pulse shape is harshly distorted. To study the radiation pattern symmetry, measurements are also performed for negative angles, 0° to −160°. The received pulses at the negative angles are the same as those at the positive angles. The measured characterizations of the antenna shows that the designed Vivaldi antenna is suitable for oil well imaging applications.

5.3 The Effect of the Metal Plate and Perforation on the Characteristics of the Received Pulse

To develop the concepts and mechanism for imaging inside a narrow metal pipe, we have investigated the interaction of UWB pulses with metals in different scenarios. In this section, we have studied the effect of size a the metal plate and perforations on the characteristics of the reflected pulses, particularly the time delay and pulse arrival time. It is very important to understand these characteristics for radar imaging of small anomalies in metal backgrounds. In the first experiment the effect of the metal plates' size on the arrival time of received pulses is studied. Then the effect of different sizes of perforations in a metal plate is experimentally investigated. We also studied the effect of the distance between the radar and the metal plate to determine the optimum distance to effectively detect small anomalies in a metal background.

The first experiment was done with square metal plates that varied in size from $1cm$ to $28cm$ as shown in Fig. 5.4(a). The radar transceiver for the measurements is shown in Fig. 5.4(b). During these measurements the distance between the radar transceiver and metal plate was kept constant at $4cm$ using a foam spacer, as illustrated. The received pulses were calibrated by eliminating the ambient pulse. For the first experimental scenario, the ambient pulse was measured by transmitting and receiving a pulse into the air. Therefore, the received pulse is mainly due to the antennas' mutual coupling. The calibrated received pulses are shown in Fig. 5.5(a). The envelope of the calibrated pulses is generated by applying a Hilbert transform, which is explained in the chapter. 2 and [99]. The envelope of the pulse shows the location of the pulse peak [99], and is illustrated in Fig. 5.5(b). The amplitude of the reflected pulse at the peak location increased as the size of the square metal patch increased from $1cm$ to $5.5cm$.

However, the amplitude of the reflected pulse was constant and lower for the cases of $12cm$, $18cm$ and $28cm$ square patches. The pulse amplitude drops for the last three patch

sizes since the location of the radar transceiver, which is $4cm$ from the metal patch, falls in the near-field of the metal plate and changes/distorts the pulse shape. The reflected pulse is a superposition of reflections from various locations on the metal plate or an object. Hence the amplitude of the received pulse depends on the time delay of the individual reflections. In far-field, where the observation point is far from the targets, the reflected pulses approximately experience the same time delay. However, in the near-field of the antenna/metal plate or both, the time delay is not the same. Varying time delay in the near-field may lead to

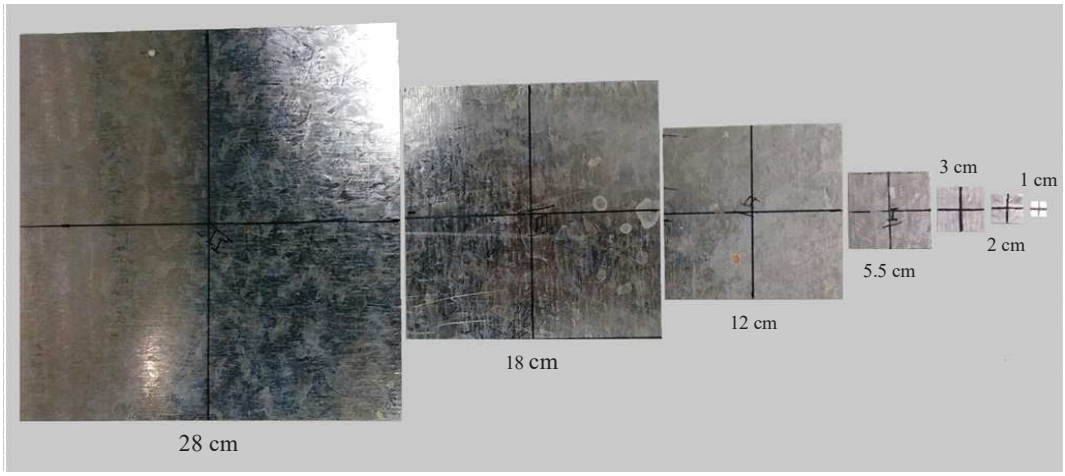

(a)

(b)

Figure 5.4: (a) Square metal plate with different sizes, (b) radar transceiver distance to the target using a half-inch-thick foam spacer.

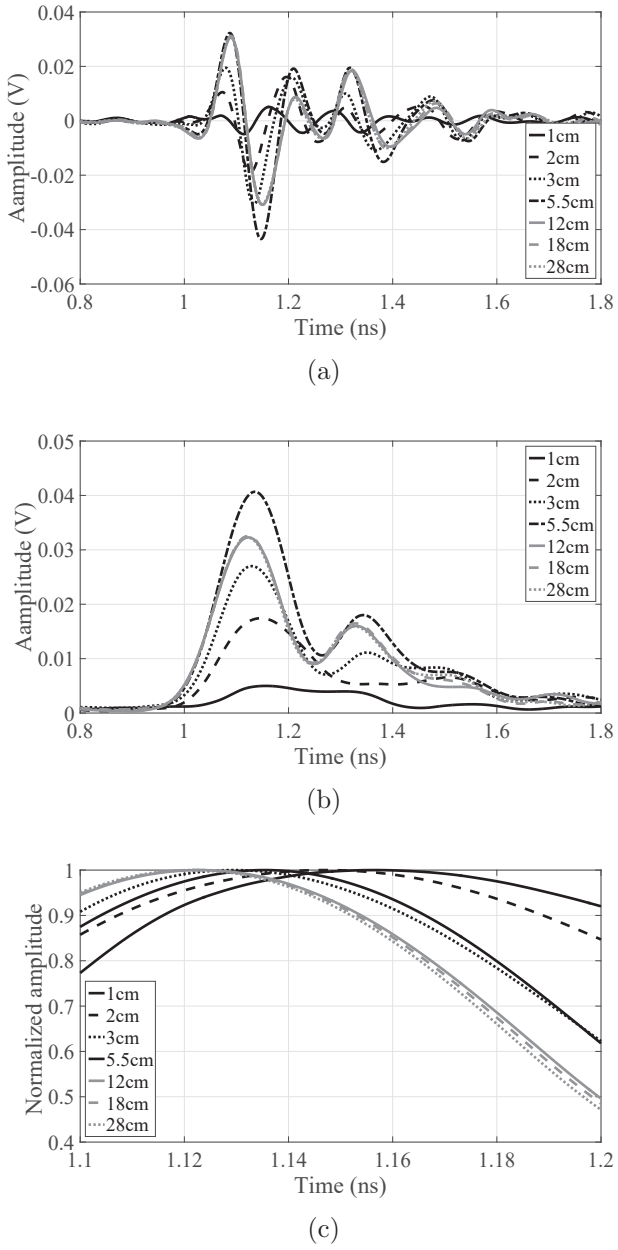

Figure 5.5: Reflected pulses by different sizes of square metal plates: (a) calibrated pulses, (b) enveloped of calibrated pulses (c) zoomed and normalized version of -b-.

destructive interference, which results in distorted pulse shape with lower amplitude. As a result of the pulse shape change in the near-field, the peak of the pulse appears sooner in time as the size of square patch increases. This phenomenon can be observed in more detail in Fig. 5.5(c), which is the normalized and zoomed version of Fig. 5.5(b). These results indicate that the pulse peak propagates faster in the near-field region. It has already been

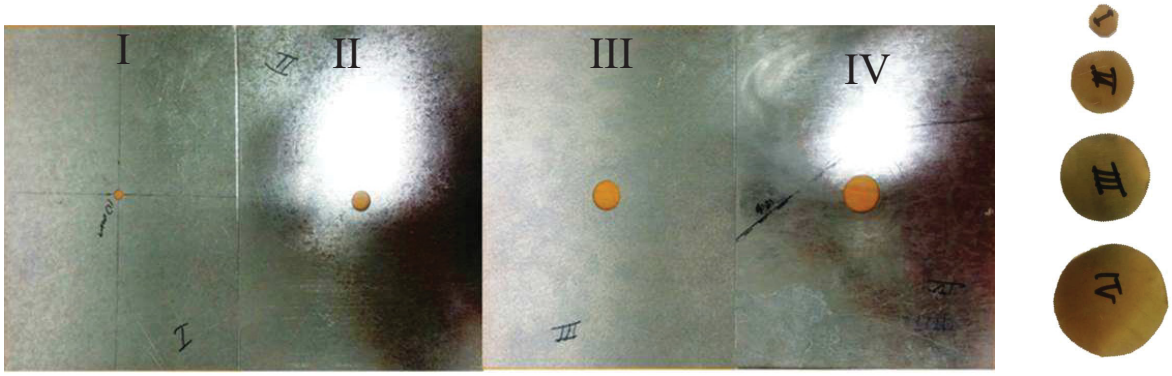

(a) (b)

Figure 5.6: (a) Metal plates with different size perforations, (b) metal patches.

demonstrated, in Chapter. 3 , that the pulse propagation in the antennas' near-field can be superluminal due to pulse reshaping [98].

In the next experiment we focused specifically on detecting a perforation in a metal plate. The perforated metal plates are shown in Fig. 5.6(a). The perforation sizes are $1cm$, $2cm$, $3cm$, and $3.8cm$. For comparison purposes, we have measured the reflected pulses off metal patches with the same size as those of the perforations. The corresponding metals patched are shown in Fig. 5.6(b). To calibrate the received pulses, the ambient pulse is measured differently for each of these cases. Received pulses reflected by the metal patches were calibrated by measuring the antennas' mutual coupling in air as described in the first experiment, whereas pulses reflected by perforated metal plate were calibrated by measuring the reflected pulse of the metal plate with no perforation in it, which is mathematically modeled as follows:

$$s_{ambi}(t) = s_t(t) \otimes h_{Tx}(t) \otimes h_{Rx}(t) \otimes h_{plate}(t) \tag{5.1}$$

where $h_{plate}(t)$ is the impulse response of the metal plate without any perforation in it. The calibration procedure is explained in Chapter. 1 and mathematically modeled by Eq. 1.8. Different measurements are conducted to evaluate the optimal distance between the

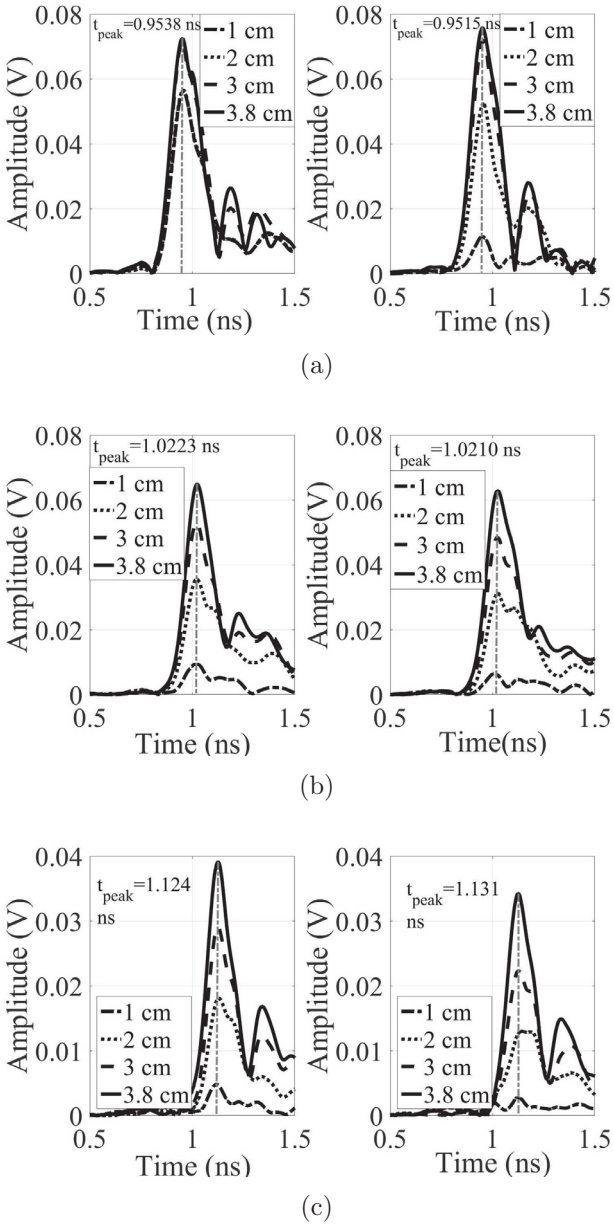

Figure 5.7: Right column; reflected pulses by metal patches (c.f. 5.6(b)). Left column; reflected pulses by perforation in metal plates (c.f. 5.6(a)). Distance between radar transceiver and object; (a) $1cm$, (b) $2cm$, and (c) $4cm$.

radar transceiver and the metal plate to effectively detect all perforations with a diameter ranging from $1cm$ to $3.8cm$. The selection of this distance plays a critical role in extracting the signature of the perforation for a given pulse characteristics and mutual coupling between the radar antennas. The measurement results are shown in Fig. 5.7. Since the envelope of the pulse is more illustrative and informative in terms of target signature and peak location, the

envelopes of the calibrated pulses are shown here. The right column encloses the signature of the metal patches and the left column has the signature of perforations in the metal plate. It can also be observed that the $1cm$ perforation is detected more clearly at shorter distances. The amplitude of reflected pulses is not related to the distance where the transceiver is very close to the perforations or metal patches, since the reflection and transmission occur in the near-field of the transceiver and target. To detect a perforation as small as $1cm$, the distance between the radar and metal plate has to be about $1cm$ for this UWB radar system. The near-field effect on pulse shaping is not very problematic here, since the received pulse is calibrated with an ambient pulse measured at the same distance that captures the near-field effects. Furthermore, here the objective is to detect the anomalies, perforation and/or corrosion; hence, the pulse shape of the target signature is not very important as long as the pulse is detected.

5.4 Metal-cased Oil well Perforation Detection and Imaging

The previous sections laid the foundation for the detection of the anomalies in a metal background, including near-field effects. In this section and the next one, detection and imaging of perforations and corrosion in a metal pipe using UWB radar are studied through simulations and measurements. First of all, the method of calibration is explained using simulation data, and then measurements are done to detect and image the perforations in air and diesel. The calibration procedure is the same as perforation detection in a metal plate. However, here the ambient pulse is measured inside a metal pipe without any perforations or anomalies. The ambient pulse expression is as follows:

$$s_{ambi}(t) = s_t(t) \otimes h_{Tx}(t) \otimes h_{Rx}(t) \otimes h_{pipe}(t) \tag{5.2}$$

where $h_{pipe}(t)$ is the impulse response of the metal pipe with no perforation. A metal pipe with a diameter of $10cm$, shown in Fig. 5.8(a), is considered for the simulations and experiments. For this simulation the diameter of perforation in the pipe is $1cm$. The ambient pulse measures the effect of everything except for the perforation in the pipe. The antenna distance to the perforation is $1cm$, since it was found to be the optimum distance in the previous measurements. Since the radar transceiver is very close to the pipe surface, the cutoff frequency of the waveguide does not affect the detection procedure. CST Microwave studio is used for full wave simulations [57]. The transmitting and receiving antennas are in a side-by-side configuration, with a half-inch gap. The received pulse (gray line), the ambient pulse (dashed gray line), and the calibrated pulse (black line), are shown in Fig. 5.8(b). As can be seen, the received and ambient pulses are very similar and have the same amplitudes. However, the received pulse is slightly delayed due to the perforation. To demonstrate it in more detail, the main lobe of these two pulses is enlarged and shown in Fig. 5.8(c). The only difference in the pulses' main lobe is the time delay caused by the perforation.

The perforation signature has been derived by subtracting the ambient pulse from the received pulse. Here the ambient and received pulses are second derivative Gaussian pulses. It is due to the fact that transmitting antenna time differentiate the input pulse [36]. Hence the radiated pulse should be second derivative Gaussian pulse as the transmitting antenna is fed with the first derivative Gaussian pulse. A metal plate differentiates the incident pulse if the measurement is performed in the far-field, and merely inverts the pulse if it is in the near-field [51]. Therefore, it is expected that both the ambient and the received pulses are shaped like second derivative Gaussian pulses, and the shape of the perforation signature pulse depends on the time delay between the ambient and received pulses. In the following subsections, pipe perforation imaging in air and diesel is explained.

5.4.1 Metal pipe perforation imaging in air

In the next step the radar imaging of a metal pipe perforation in air was performed. The measurement setup is shown in Figs. 5.9(a)-5.9(c). As shown in Fig. 5.9(c), the metal

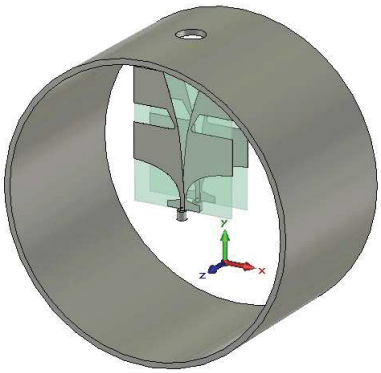

(a)

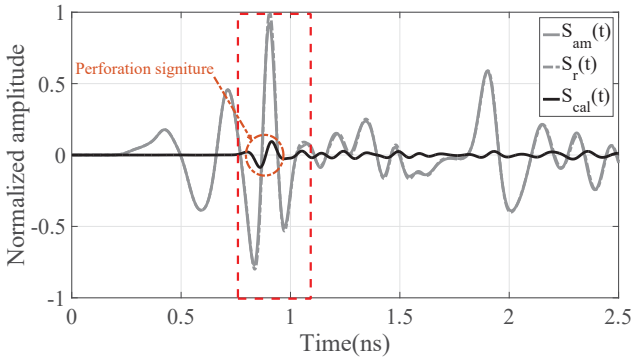

(b)

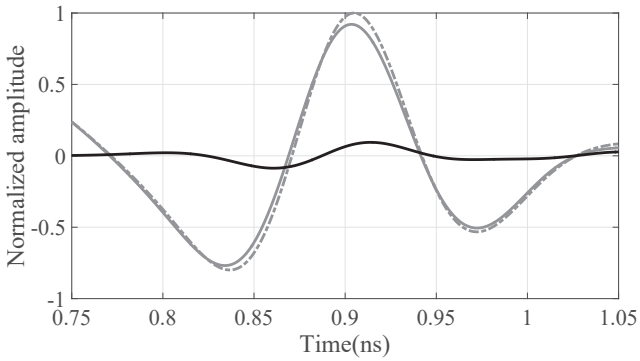

(c)

Figure 5.8: (a) Perforated metal pipe in simulation setup, (b) calibration procedure for perforation detection in oil metal pipe, (c) zoomed version of Fig. 5.8(b).

pipe has three perforations with diameters of $1cm$, $1.9cm$ and $2.45cm$. Different perforation diameters are considered to cover the diversity in size of real perforations in oil wells, which are usually around $1cm$ to $3cm$. The radar transceiver was set inside the pipe through a slot in the pipe, at a distance of $1cm$ from the metal wall, shown in Fig. 5.9(b). As the time delay between the received and ambient pulses is very minimal, the measurements have to be very accurate to be able to extract the signature of the perforation. The pipe was held by two pieces of Styrofoam and moved every $5mm$ to acquire the raw data. The raw data and its envelope are shown in Figs. 5.9(e)-5.9(f). The location of the $1.9cm$ and $2.45cm$ perforations can be seen; however, the signature of the smallest perforation is not detected in the raw data. The horizontal straight lines in Figs. 5.9(e)-5.9(f) are reflections due to the metal pipe surface. The calibrated raw data and its envelope are shown in Fig. 5.10(a)-5.10(b). After the calibration, the perforations' signatures are clearly detected and imaged.The calibrated raw data of the perforations' signatures are shown in separate windows so that the $1cm$ perforation signature can be seen clearly as well. The perforation locations are marked by the dashed rings, which match the locations of the perforations in the pipe. The size of the perforation can be estimated based on the intensity of the signals at the aperture position. The bigger perforation has bigger reflection intensity, as seen in the illustration.

Even though the signatures of perforations are clearly detected in the calibrated raw data, the reconstructed image of these raw data can provide more information or a better representation of the perforations. The GBP technique explained in Chapter. 1 and [27, 41], was used to reconstruct the image. As mentioned earlier, image reconstruction in time domain requires the peak velocity of the pulse in the medium. The pulse peak velocity can be found using a calibration procedure, which is explained in detail in Chapter. 3 and [98]. Since the radar imaging is done very close to the radar transceiver, superluminal effects will appear [98]. To find the velocity of the pulse peak in this scenario, two measurements are conducted by placing a flat metal plate on the antenna aperture and $1cm$ away from the antenna aperture as the measurements are performed within this distance.

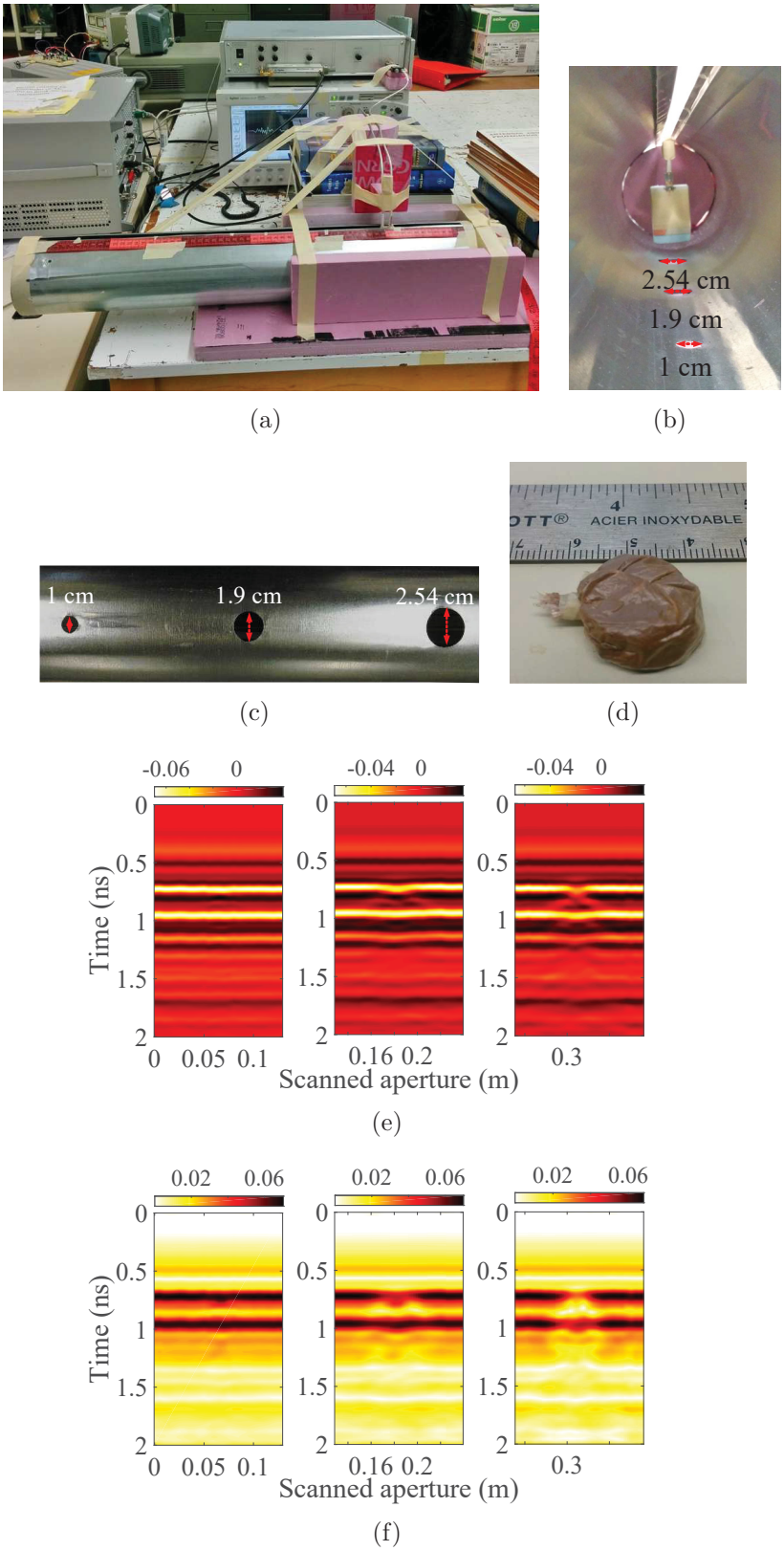

Figure 5.9: (a) Metal pipe perforation imaging in air, (b) metal pipe interior, (c) metal pipe exterior, (d) iron rust, (e) raw data, (f) envelope of the raw data.

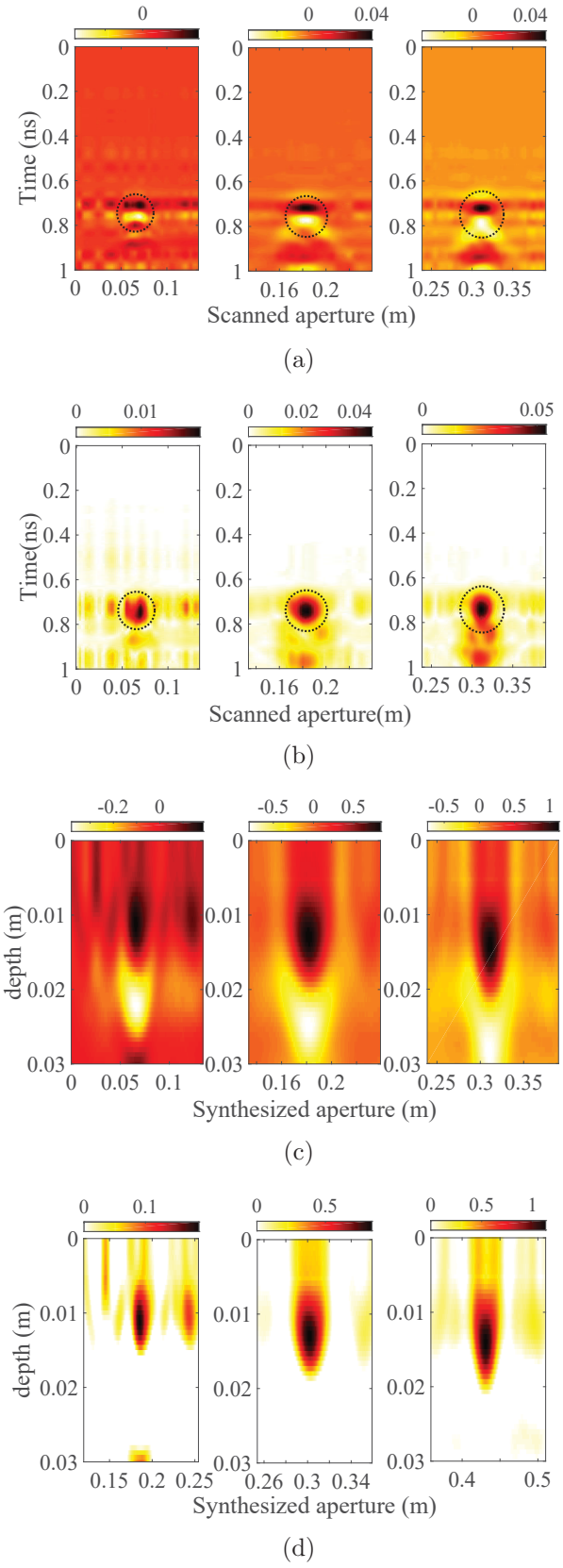

Figure 5.10: Pipe perforation imaging in air; (a) calibrated raw data, (b) envelope of the calibrated pulse, (c) real image, (d) positive image.

Comparing the location of the peaks of these two pulses with respect to the round-trip distance results in the velocity of the peak of the pulse. Average velocity might be considered if the pulse has multiple peaks. Here the average pulse peak velocity is $1.4c_o$, where c_o is light velocity in the vacuum. The reconstructed image based on measured calibrated raw data is shown in Fig. 5.10(c). A positive image, explained in Chapters. 1 and 4 and [41], is generated to enhance the image sharpness. The positive image is generated by adding up the real part of the reconstructed image to absolute of it. The positive image is shown in Fig. 5.10(d). The perforations' location is shown in reconstructed images. The perforation size can be estimated based on the image amplitude. The biggest perforation has an image amplitude of about 0.7, whereas the image of the first perforation, which is $1cm$ in diameter, has an amplitude of 0.13.

5.4.2 Metal pipe perforation in diesel

This subsection looks at imaging pipe perforations within diesel. As shown in Fig. 5.1, usually there is concrete casing behind the metal casing. However, radar cannot see behind metal, so we did not include the concrete casing in the measurement setup. The measurement setup is shown in Fig. 5.11(a). A wooden box sealed with plastic covers was used to enclose the metal pipe and diesel for accurate measurements. Similar to measurements in air, the data was collected at $5mm$ intervals, and the reflections were recorded. The calibrated raw data and its envelope are shown in Figs. 5.11(b)-5.11(c). The perforations' signatures are detected and imaged in the raw data.

The images are reconstructed in the same way, using the measured pulse peak velocity, which is described in the previous subsection. Since this measurement is done in diesel, the pulse peak velocity is divided by the square root of 2.5, which is the electric permittivity of the diesel. The reconstructed images are shown in Figs. 5.11(d)-5.11(e). These images demonstrate that the perforations are clearly imaged, particularly in the positive image.

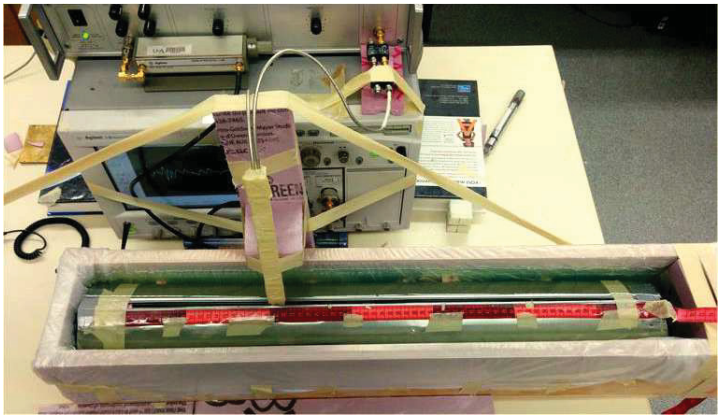

(a)

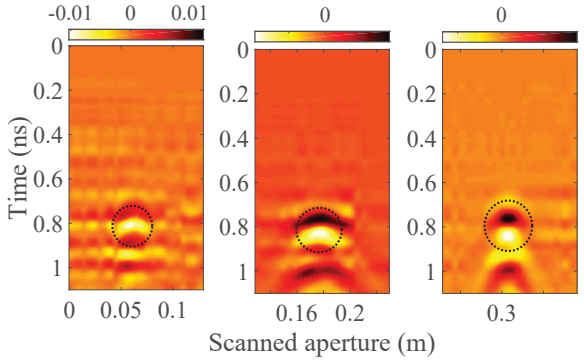
-0.01 0 0.01
0
0.2
0.4
0.6
0.8
1
Time (ns)
0 0.05 0.1
0
0.16 0.2
0
0.3
Scanned aperture (m)

(b)

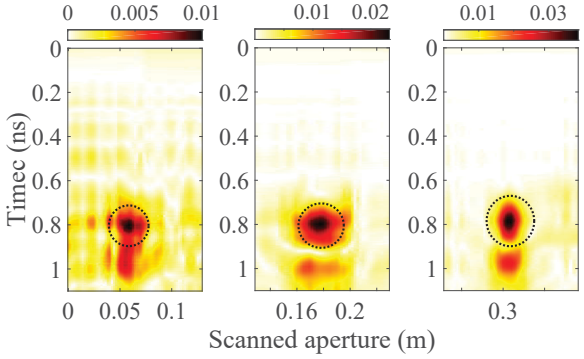
0 0.005 0.01
0.01 0.02
0.01 0.03
0
0.2
0.4
0.6
0.8
1
Timec (ns)
0 0.05 0.1
0.16 0.2
0.3
Scanned aperture (m)

(c)

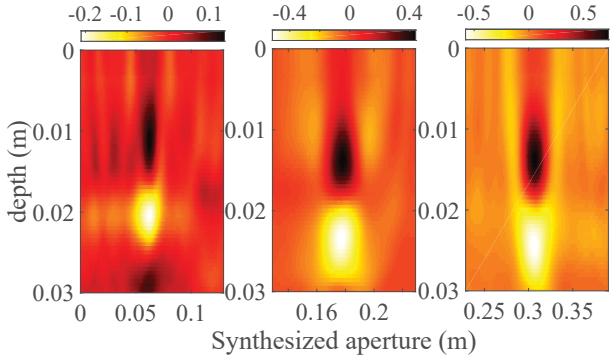
-0.2 -0.1 0 0.1
-0.4 0 0.4
-0.5 0 0.5
0
0.01
0.02
0.03
depth (m)
0 0.05 0.1
0.16 0.2
0.25 0.3 0.35
Synthesized aperture (m)

(d)

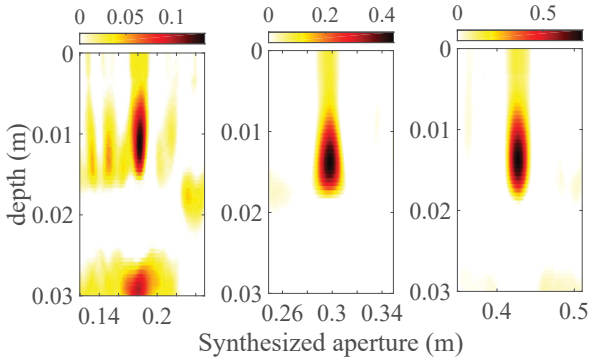

(e)

Figure 5.11: Measurement setup in diesel for pipe perforation imaging; (b) calibrated raw data, (c) envelope of the calibrated raw data, (d) real image (e) positive image.

The study and results show the ability of UWB radar to detect and image perforations as small as $1cm$ in a metal-cased oil well. In the next section, corrosion detection and imaging are deliberated.

5.5 Corrosion Detection and Imaging

Corrosion in metal-cased oil wells can create serious problems for the wells [100]. Oil well corrosion costs the oil and gas industry hundreds of millions of dollars each year [101]. Regular monitoring of corrosion in oil wells is required to assess the problem and take timely action. Different logging techniques have been developed to detect corrosion in an oil well. These techniques include ultrasound [102] and pulsed eddy current [93] techniques.

We proposed a UWB radar system to detect and image the corroded area in a metal-cased oil well. The electrical properties of metal changes after corrosion. This change can be detected by a radar. To conduct the experiment, the electric property of metal rust was measured using an Agilent dielectric probe, shown in Fig. 5.12(a). The metal rust is a lossy material which introduces losses to the EM waves. The procedure for detecting a small area of corrosion, that is $1cm \times 1cm \times 0.5cm$ shown in Fig. 5.12(b), in a metal background is explained in the following. The reflected pulse with the presence of the corroded area is compared to the reflected pulse by a non-corroded metal. The reflected pulse from the

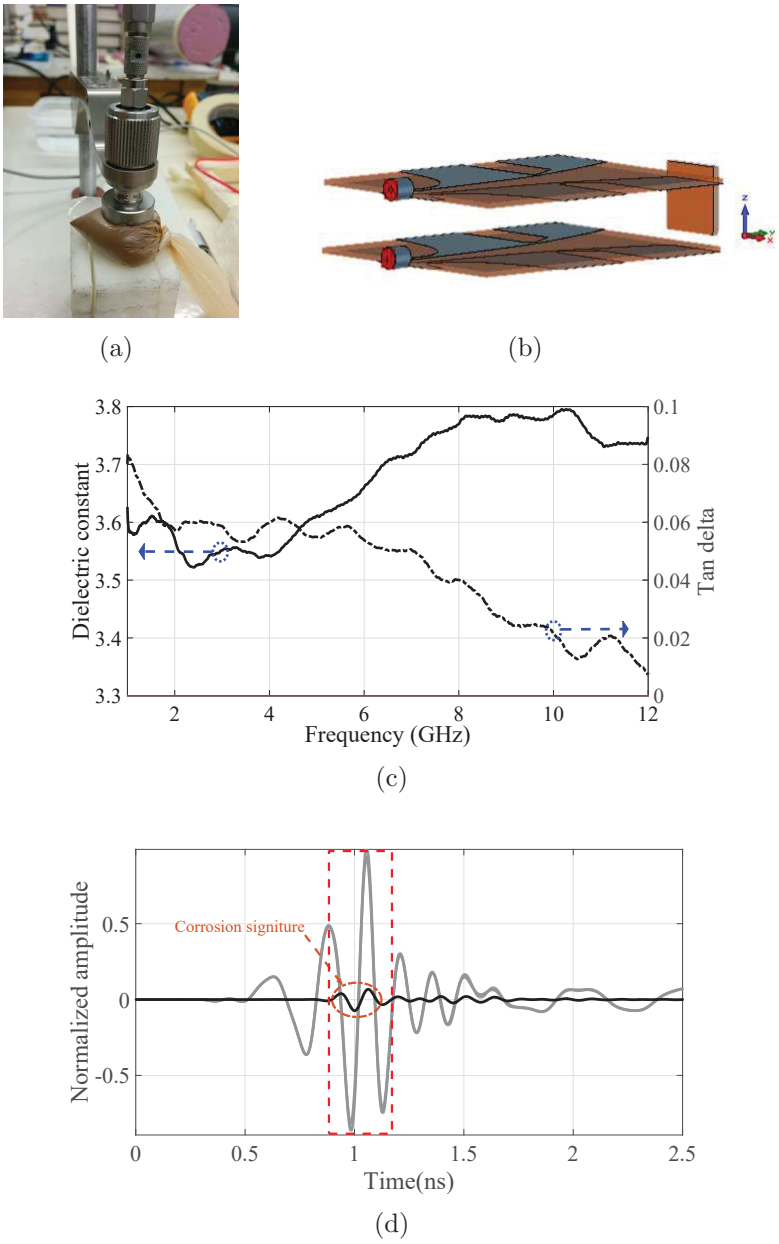

Figure 5.12: (a) Rust dielectric properties measurements setup, (b) simulation setup for detection of the corroded area, (c) rust dielectric properties, (d) calibration procedure for corrosion detection, $1cm \times 1cm \times 0.5cm$, in a metal back ground within crude oil as medium.

corroded area is delayed in time and attenuated. The difference between these two pulses is the signature of the corroded area.

The pipe perforation imaging experiment in air, with the same setup configuration shown in Fig. 5.9(a), with a small amount of rusted metal powder shown in Fig. 5.9(d) is repeated. The rust material was packed in a plastic bag with dimensions of $1cm \times 1cm \times 0.5cm$.

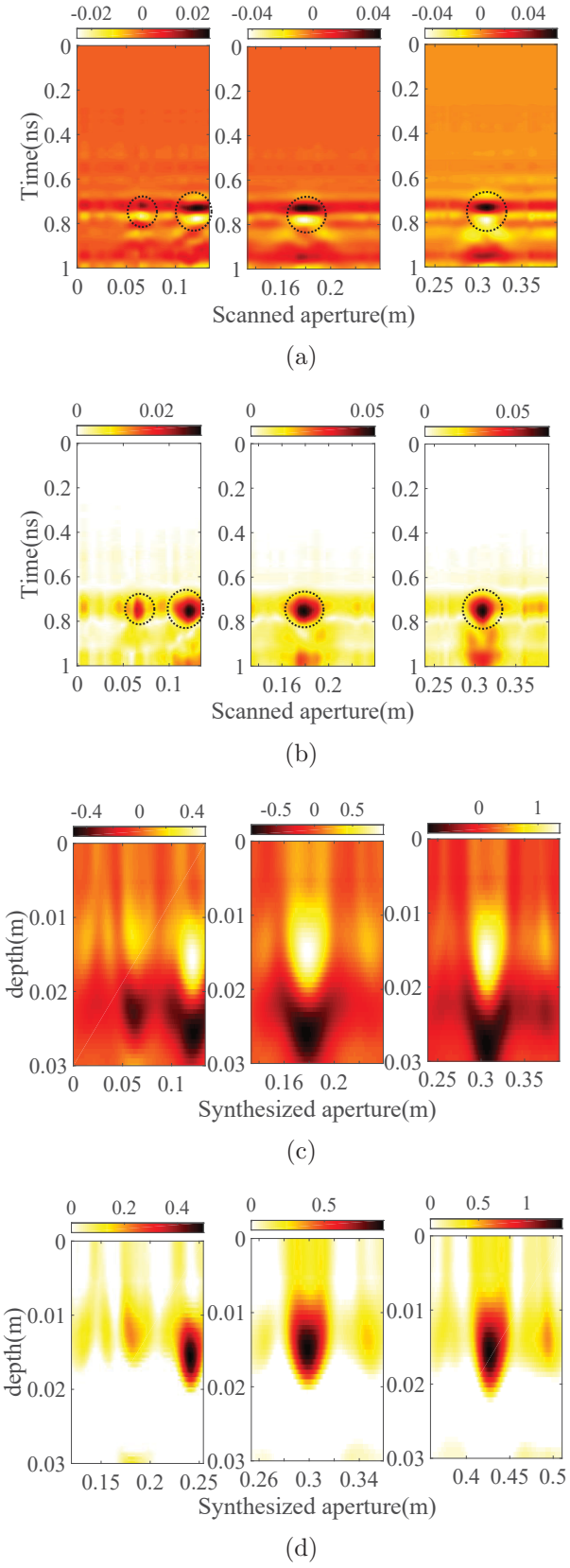

Figure 5.13: Pipe perforation and corrosion imaging in air: (a) calibrated raw data, (b) envelope of the calibrated pulse, (c) real image, (d) positive image.

The rust material was located between the first and second perforations in the metal pipe. The pipe was moved and the reflected pulses were recorded at $5mm$ intervals. The calibrated raw data and its envelope are shown in Fig. 5.13(a)-5.13(b), respectively. The signature of the corroded area is clearly captured between the first and second perforation. The reconstructed images are shown in Fig. 5.13(c) and Fig. 5.13(d). The location of rust and perforations is clearly imaged. The size and depth of the corroded area changes the reflected pulse shape and time delay. Therefore, the reconstructed images have higher intensity where the corroded area is bigger. These images can be used to estimate the size of the rusted area.

5.6 Conclusion

This chapter discussed the application of UWB-SAR to detect and image perforations and corrosion in metal-cased oil wells. Various measurement and simulation scenarios were performed to develop understanding about the characteristics of the reflected pulse from metal surface with and without anomalies. The effect of the metal surface, perforation and the radar distance to the target were also studied. The optimum radar distance to effectively detect a perforation as small as $1cm$ was determined. Three different measurement scenarios for the detection and imaging of perforation in air, oil and corrosion on metal surface were performed. The radar data were processed with $LSAR$ to reconstruct the images. All measurements confirmed the capability of UWB radar to monitor metal-cased oil wells.

Chapter 6

SAGD Process Monitoring in Heavy Oil Reservoir Using UWB Radar Techniques

6.1 Introduction

Heavy oil reservoir management using automated sensors and control techniques to monitor oil well production has been introduced and developed as a new concept in the oil and gas industry [103–105]. In particular, having sensors capable of capturing the dynamics of the reservoir in the proximity of an oil well would provide necessary feedback to enhance the production [4, 106].

Oil from heavy oil reservoirs cannot be recovered by the conventional methods, those used in light crude oil extraction, due to the high viscosity of bitumen. Generally, heavy oil is recovered by the SAGD process, which is one of the leading methods for oilsand reservoir extraction [107–112]. This method is realized by drilling a pair of horizontal wells into the reservoir in which the upper pipe injects high pressure steam to reduce the viscosity of the bitumen, while the lower pipe collects the liquefied bitumen. Since the SAGD process has an

impact on the environment, close monitoring of the steam chamber development is required. Water consumption in the SAGD process can be optimized by mapping the reservoir through radar scanning; it also determines the reservoir volume and locations of the impermeable rocks. Furthermore, real-time monitoring of reservoir conditions and steam flow patterns may help to prevent the occurrence of an uneven stunted steam chamber and provide better control of the steam flow [110, 113]. Considering the huge impact of the oilsand industry on the Canadian economy, developing advanced monitoring technologies would significantly reduce the cost of oil extraction and provide more protection to the natural environment. The SAGD process has been traditionally monitored and imaged by microseismic monitoring techniques [114–116]. These methods need a huge number of geophones, on the order of tens of thousands, placed at different locations in or over the top of the reservoir. Furthermore, processing the enormous amount of recorded data produced by geophones makes real-time monitoring impossible or very difficult. Also, this method may not be able to monitor the shallow depth reservoirs due to the interference by mechanical waves from the surface, which significantly reduces the SNR.

EM waves are much more sensitive than seismic waves to changes in reservoir fluid saturation; therefore an EM sensor is potentially more suitable to monitor fluid movement such as the steam chamber growth. Hence, radar techniques can be used to monitor the SAGD process. The feasibility of employing radars as down-hole sensors has been studied through simulations in [4, 106, 117]. The applications of UWB radar system for imaging of oil well perforations is demonstrated in the chapters 4-5. In this chapter, we study the experimental feasibility of employing an UWB radar system as a buried sensor for monitoring oilsand reservoirs. A UWB radar system tailored for monitoring the SAGD process requires UWB antennas capable of radiating within the reservoir medium, whose permittivity is higher than free space.

Miniaturization of the antennas is essential as it makes installation and infrastructure design in the reservoir easier and inexpensive. Different types of UWB antennas, such as

bow-tie, antipodal, spiral, double ridged, and transverse electromagnetic horns have been in use for different radar applications [34, 55, 56, 118–120]. A miniaturized antipodal antenna modified for radiating into the oilsand is designed and used as a sensor for the radar system in these experiments. Antipodal antennas have been in use for various applications, especially for pulse based systems, due to characteristics including broadband impedance matching, unidirectional radiation, low pulse distortion, compact size, and ease of fabrication [55, 56, 118].

In this chapter, first the details of the SAGD process monitoring for heavy oil extraction, measurement setup, and miniaturized antenna design is presented. The EM pulse characterization in dry and wet sand and in the vicinity of metal pipes is presented in the next section. Power budget analysis for oilsand reservoir imaging, inhomogeneity of the reservoir medium and imaging of the emulated steam chamber growth and using LSAR are explained and demonstrated afterwards. The last section discusses the importance, applicability, and economic feasibility of the proposed method.

6.2 SAGD Process Monitoring and Radar System Design

Heavy oil reservoir and SAGD process monitoring using a radar system are shown in Fig. 6.1(a). The heavy oil reservoir is a heterogeneous medium, which is an intrinsic aspect of any reservoir, filled with oilsand, rocks and fractures [108]. Reservoir mapping can help in effective steaming in terms of controlling the direction and pressure of steam injectors. Once steaming starts, steam chamber growth can be monitored on a near real-time basis, which can result in efficient reservoir management in terms of water usage and oil extraction [121]. In general, steam is continuously injected into a heavy oil reservoir for several months which grows the steam chamber up to $20m$ [108]. Steaming of the reservoir increases the dielectric constant of the steamed area, which makes this region electrically discernible. Hence, the

discontinuity in electrical properties between dry and wet regions of the reservoir might be distinguished by radar principles. Steam propagation in the SAGD process can be monitored by having an array of antennas on top of the reservoir and over the injector pipe [4,106,117] or any other locations in the reservoir in vertical and horizontal configurations. The sensor array over the injector pipe can be mounted on the pipe before installing it inside the borehole. However the borehole diameter has to be wider to accommodate the antennas. The radars on the injector pipe are used only in the initial scanning, i.e., before steaming begins. Definitely, having more arrays of sensors inside the reservoir provides more information about the SAGD process and steam chamber growth.

6.2.1 Radar monitoring system and measurement setup

The UWB radar system is capable of detecting the contours of the steam chamber in the reservoir based on the reflections and transmission of the electromagnetic pulses at the interfaces. The feasibility of using a UWB radar system for SAGD process monitoring is experimentally investigated in this chapter. To develop the concept and its validation, several simulations and measurements have been conducted in this study. The measurement setup contains a UWB radar system, and a wooden box filled with dry and wet sand, where the wet

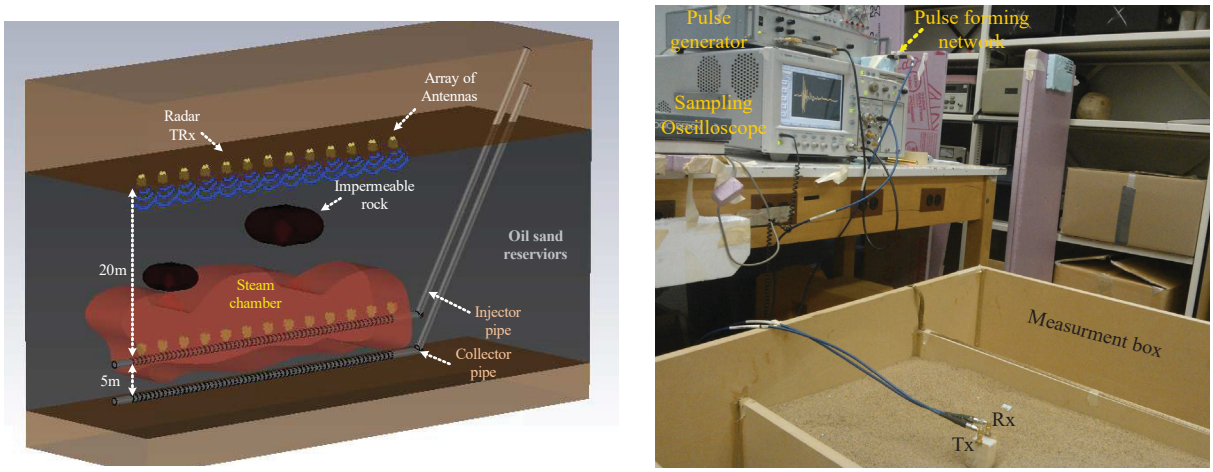

(a) (b)

Figure 6.1: (a) SAGD process monitoring and sensor arrangements, (b) radar measurement setup.

sand emulates the steamed region. The UWB measurement setup introduced in Chapter. 1, shown in Fig. 1.6(b), is employed to perform the measurements.

6.2.2 Miniaturized antipodal antenna as EM sensor

The UWB radar system for SAGD process monitoring requires antennas capable of radiating within the oilsand, unlike conventional antennas, due to the fact that the sensor system is buried in the oilsand. An antipodal Vivaldi antenna or TEM horn antennas are good candidates for UWB radar applications for moderate-to-high power applications respectively [34, 55, 56, 118–120]. In this study, a miniaturized antipodal Vivaldi antenna capable of radiating within the oilsand is designed and tested. The antipodal Vivaldi antenna is a printed circuit device and is capable of handling several Watts of electromagnetic power. Bitumen and dry sand in the oil reservoir have a dielectric constant of 2.5 and 2.56, respectively [27]. Therefore, the antenna is designed to efficiently radiate in a medium of dielectric constant 2.5. The dielectric constant of oilsand varies from 2.5 to 3.5 [122]. The antenna is fabricated using a Rogers' substrate ($RO4003$) laminate of dielectric constant 3.38 and thickness of $0.8mm$. The overall dimensions of the antenna are limited to $36mm \times 46mm$. More details of the antenna dimensions are shown in Fig. 6.2(a). The fabricated antenna is shown in Fig. 6.2(b). The antenna is fed by a 50 Ohm coaxial line. The quasi mono-static radar transceiver is realized by bundling two Vivaldi antennas, one as the transmitter and the other as the receiver, separated by a 3 cm-thick Teflon insulator. The simulated and measured S_{11} of the antenna in dry sand is shown in Fig. 6.2(c). As can be seen, antenna return loss is acceptable up to $20GHz$. Dry sand is used for measurements as its dielectric constant is very close to the oilsand. The simulated radiation patterns of the antenna in dry sand at various frequencies are shown in Fig. 6.2(d). The antenna's realized gain at each frequency is illustrated by the color bar.

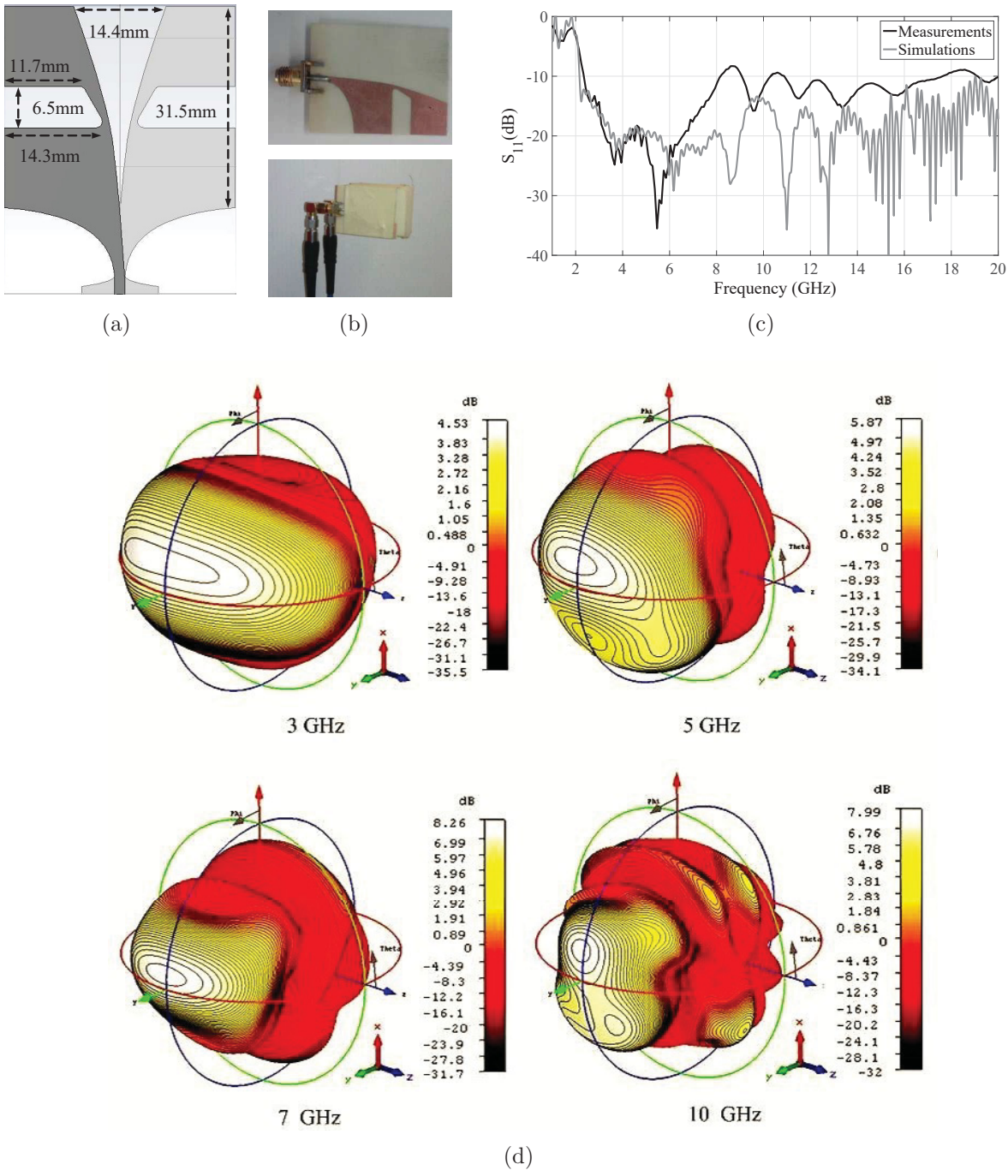

Figure 6.2: (a) Simulated antenna structure, (b) fabricated antenna [top], radar transceiver [bottom], (c) antenna return loss simulation and measurement in dry sand, (d) simulated antenna radiation pattern in dry sand at different frequencies.

6.3 Pulse Characteristics in Dry and Wet Sand in the Vicinity of Metal Pipes

Several experiments are conducted to understand the EM pulse propagation and distortion in the heavy oil reservoir medium, particularly in the vicinity of metal pipes. In these experiments, both transmitting and receiving antennas were buried in dry and wet sand, and the received pulses were studied. To study the effect of metal pipes on the pulse characteristics, a rectangular metal plate and pipe as reflectors were placed behind the Tx and Rx antennas.

It is a known fact that the water contents in oilsand increases the dielectric constant and loss tangent of the medium and affects the radar signal propagation. The dielectric constant of sand with various moisture contents are shown in Table. 6.1.

Table 6.1: Dielectric constant of sand

[123]	Moisture %	0	2.7	4.9	10.4	13.3
	Dielectric constant	2.32	3.2	4.77	5.83	7.46
This measurement	Moisture %	0		Saturated		
	Dielectric constant	2.7		10		

In this investigation, we also studied the dielectric properties of the saturated sand and the antenna performance in it. The dielectric properties of sand are measured using the time domain radar cross section (RCS) method [51]. A measurement error of 5% to 10% is associated with the time domain RCS method. Play sand with a porosity of about 10% is used in the experiments. Simulation and measurements show that the dielectric losses increase significantly as moisture content increases. The antenna return loss and radiation patterns became severely degraded in the saturated sand. However, the reflection at the boundary of dry and saturated sand is very strong, due to the big difference in wave impedance, which makes the wet sand visible to the radar. The designed antenna has acceptable performance in terms of return loss and radiation efficiency for a medium with a dielectric constant up to 5. It implies that using the same antenna, the measurements can be carried out in sand that has a moisture content of up to 5% [123]. The measurement scenarios are explained in

the following subsections.

6.3.1 Pulse characteristics in dry and wet sand

The experimental setup for these measurements is illustrated in Fig. 6.3(a). During the measurements, antennas were fully buried in sand. The effect of the medium on the pulse shape and path loss was measured by facing Tx and Rx antennas at each other, with a 21cm distance in both air and sand. The measurements were carried out at short distances due to low power equipment available in the lab. The shape and pulse width of the received pulse is affected by the antenna's and medium's impulse responses. For comparison, the received pulses were measured in all air and dry and wet sand, and are shown in Figs. 6.3(b)-6.3(c). A piece of foam was used to hold the antennas for measurement in air. The same distance was maintained between the antennas for measurements inside sand as shown in Fig. 6.3(a). For measurements in sand, antennas were buried in sand at about 15cm depth. Amplitudes of the received pulses are normalized to the peak value of the received pulse in air. To detect the right location of peak of the received pulse, an to find the time delay, the envelope of the pulse is generated. Chapter. 2 includes thorough information about envelope detection for radar imaging and detection.

The received pulses in dry sand, shown in Fig. 6.3(b), are plotted in gray lines, whereas their envelopes are plotted in black lines. The received pulse in sand is delayed and attenuated due to the higher dielectric constant and loss tangent of the sand. A higher dielectric constant implies a lower speed of wave propagation in sand. Moreover, as shown in Fig. 6.3(b), the shape of the received pulse in sand and air is different from the input pulse, which was a first derivative Gaussian pulse. The received pulses more closely resemble the second derivative Gaussian pulse with some distortions. The time differentiation of the input pulse occurred during transmission [36], and pulse distortion and attenuation occurred while in propagation. The measurement errors could be due the drifting of pulse generator and sampling oscilloscope, however our measurement records show that the error is trivial, and

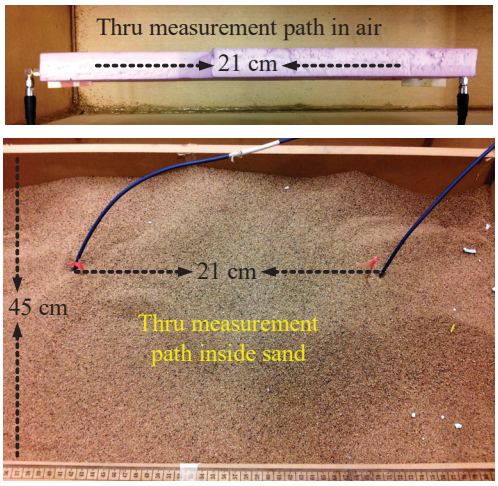

(a)

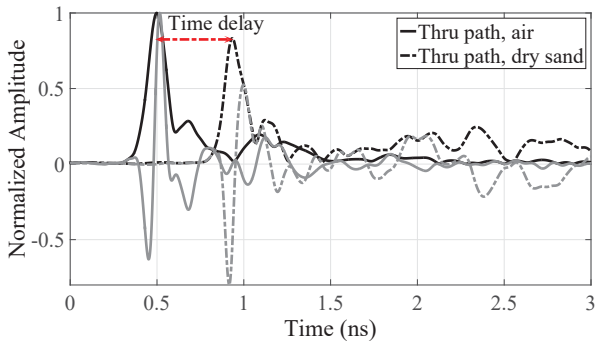

(b)

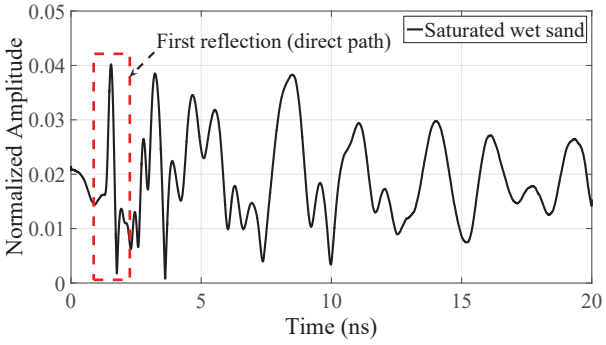

(c)

Figure 6.3: (a) Measurement configuration for through path, (b) through measured pulses in free space and dry sand, note: gray lines are received pulses and back lines are their corresponding envelopes, (c) through measured pulse in saturated wet sand. Note: pulses amplitude is normalized to pulses amplitude in air.

is within 1%.

Pulse propagation in saturated wet sand was also investigated through measurements

and is shown in Fig. 6.3(c). Again, the signal amplitude is normalized to the received pulse in air. As can be seen the received pulse through wet sand experienced more attenuation and distortion compared to the one in dry sand. The received pulse in wet sand is received at multiple times. The reasons for these discrepancies can be: impedance mismatch at antenna aperture, which results in radiation at different times, and heterogeneity of the wet sand. Here the received pulse is captured up to $20ns$. Even though the received pulse in wet sand arrives at different times, the time delay for the direct path is associated to the dielectric constant of wet sand, which is about 10.

6.3.2 Reflected pulse characterization with reflector plates

Since the injector and collector pipes in the SAGD process are made of metal, and antennas might be installed close to them, pulse propagation and its characteristics in the vicinity of metal pipes were investigated using metal plates and pipes as reflectors. Three experiments were conducted to study the pulse characteristics in the presence of metal pipes. First, a metal plate was placed in front of the radar transceiver as shown in Fig. 6.4(a) to study the received pulse in the sand medium. The distance between the radar transceiver and the metal plate was $30cm$. The pulse was transmitted through the Tx antenna and received by Rx antenna after it was reflected by the metal plate. The received pulse is analyzed to probe the effect of the metal reflector on the pulse characteristics. In the second and third experiment, the effect of the nearby metal pipe on the received pulses was studied by introducing a square metal plate and a pipe ,with corresponding dimensions of $20cm$ width and $4cm$ diameter, respectively, as reflector at a distance of $4cm$ behind the radar transceiver, as shown in Figs. 6.4(b)-6.4(c).

For a quasi-mono-static radar system, the antenna mutual coupling affects target's signature significantly. In order to reveal the effect of metal pipe/reflectors on the received pulse, the medium and antenna effect on the pulse have to be removed. The ambient pulse was measured by sending and receiving a pulse inside the sand with no metal reflectors. The

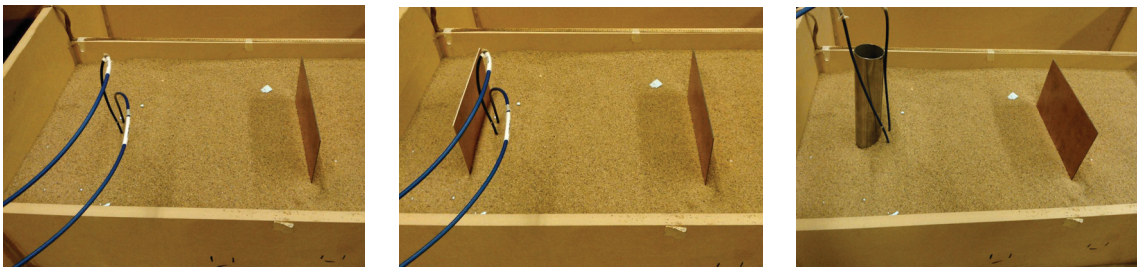

(a) (b) (c)

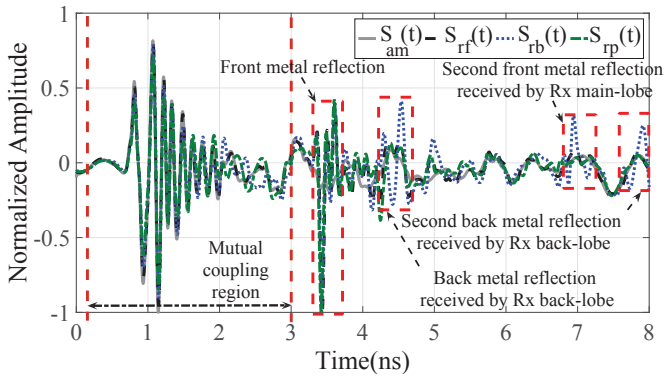

(d)

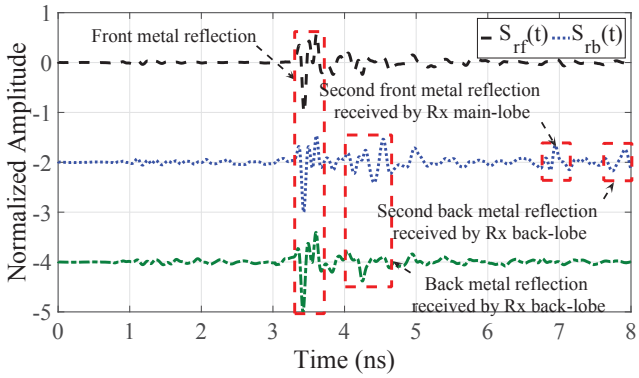

(e)

Figure 6.4: Measurement setup; (a) front metal plate reflector, (b) front and back metal plate reflector, (c) front and back metal pipe reflector, (d) received pulses, (e) calibrated received pulses.

ambient pulse contains all the other effects, including the medium, antennas, cables, and also the finite size of the experimental setup. By subtracting the ambient pulse from the received pulse, the signature of the target, the metal plates/pipe, is extracted.

Reflected pulses by the front metal plate with and without the presence of the back metal plate and pipe, as reflector, are called $s_{rf}(t)$, $s_{rb}(t)$ and $s_{rp}(t)$ respectively. The uncal-

ibrated received pulses corresponding to experiments described in Figs. 6.4(a)-6.4(c), and the recorded ambient pulse, $s_{am}(t)$, are illustrated in Fig. 6.4(d). Up to $3ns$ is the antenna mutual coupling, and there is no information about the metal reflectors. The received pulses after calibration are shown in Fig. 6.4(e). The upper graph, black solid line, is the received pulse reflected by the front metal plate. A UWB pulse undergoes an extra time differentiation every time the pulse hits a metal plate [51]. The received pulse resembles the third derivative Gaussian pulse with some distortions. Dotted blue and dotted-dashed green lines in Fig. 6.4(e) are the received pulses of the measurements described in Fig. 6.4(b)-6.4(c), respectively. As can be seen in the dotted blue line, several reflections appeared due to the effect of the back metal reflector. The pulse bounces between the front and back reflectors until the energy level is dissipated due to spreading factor and dielectric loss of the sand. The received pulse was recorded up to $8ns$ and shows four reflections in Fig. 6.4(e). The pulse was first reflected by the front reflector, and received by the transceiver main lobe at $3.4ns$. The reflected pulse by front reflector hit the back reflector, a portion of the pulse reflected by the back plate was received by transceiver back and side lobes at $4.3ns$, and the rest again hits the front reflector and is received by the transceiver main lobe at $6.9ns$. The fourth reflection was received by the side lobes and back lobe at $7.8ns$ once it was reflected by the back reflector. As can be seen, the pulse amplitude decreases after every bounce.

The metal pipe was used as the back reflector in the third experiment. Similar to the second experiment, the pulse started bouncing between the front reflector and the pipe. However, due to the smaller RCS of the metal pipe, its reflection from pipe, appeared at $4.2ns$, has lower amplitude. The third and fourth reflections did not appear at all. This shows that metal pipes do not have much effect on the nearby transceiver performance. Extra reflections caused by metal pipes can be removed by time-gating of the received pulses. From these experiments, it is very clear that the shape of the reflected pulse changes due to the presence of the metal plate or pipe. The above analysis of the received pulses in different conditions shows the ability of UWB radar to distinguish the reflection from the metal pipes

based on the time delay and pulse shape.

6.4 Power Budget Analysis for Oilsand Reservoir Imaging Application

Power requirement for scanning the proposed oilsand reservoir mainly depends on the (I) attenuation of the electromagnetic signal in oilsand, which depends on the conductivity of the oilsand medium; (II) path loss due to energy spreading in the reservoir, which depends on the scanning range of the reservoir; and (III) the level of mismatch in electrical properties between steamed and dry reservoir areas. Considering the introduced losses, the required power for the transmitter can be calculated. In addition, signal processing techniques such as pulse integration/averaging can be adopted to reduce the transmitted power by enhancing SNR [99]. Signal attenuation has been calculated based on the measured electrical properties of oilsand samples of different grades from the Athabasca reservoir at $2.45GHz$ [122]. A full-wave simulation model, using CST Microwave Studio, was developed based on the measured dielectric constant and loss tangent at $2.45GHz$. The first order Debye model was applied to consider the frequency variation of electrical properties of the oilsand. Table. 6.2 shows the measured electrical properties of different grades of Athabasca oilsand. Table. 6.3 shows the simulation results for attenuation of pulse peak power for different ranges in the reservoir. Power losses of the pulse over different distances are acquired for mediums' properties according to Table. 6.3. The frequency content of the transmitted pulse in these simulations ranges from 1 to $11GHz$. This frequency bandwidth was used based on our pulse generator specification, which provides high range resolution. However, for a real field measurements scenario, high range resolution is not required and pulse bandwidth up to maximum of $500MHz$ would be satisfactory. Operating at lower frequencies results in lower losses and lower input power would be required. Simulations and calculations in this section can be applied to pulses of any bandwidth and frequencies. As shown in Table. 6.3, the

lowest grade oilsand has the highest signal attenuation.

As the pulse propagates into the oilsand, the high frequency content of the pulse atten-

Table 6.2: Athabasca oilsand samples

Bitumen grade	$\epsilon_r^{'}$	$\epsilon_r^{''}$	$tan\delta$
Lowest	2.8446	0.0569	0.002
Low	2.8702	0.0182	0.0063
High	3.217	0.0152	0.0047

Table 6.3: Dissipated loss in different oilsand grades

Distances	Lowest grade, loss(dB)	Low grade, loss(dB)	High grade, loss(dB)
1 m	13.95	5.97	4.2
2 m	23.13	9.85	8.2
4 m	32.26	17.31	14.83
8 m	39.19	26.34	23.48
16 m	44.8	34.46	32.05
32 m	49.52	41.15	39.09

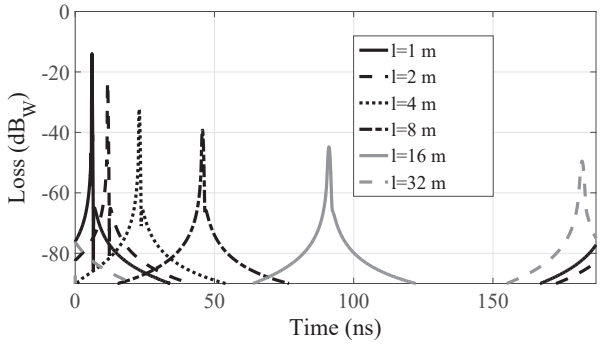

(a)

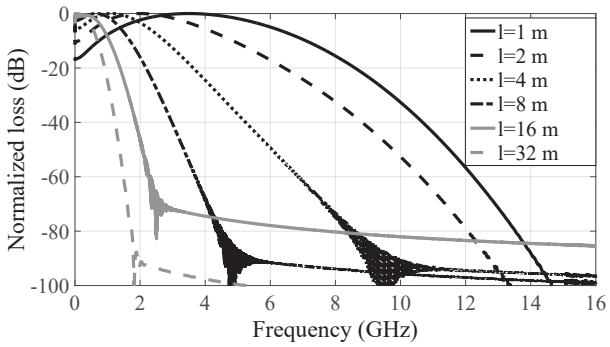

(b)

Figure 6.5: Simulation results of received pulses propagating in lowest grade Athabasca oilsand for different depths l; (a) time domain received pulses, (b) frequency spectrum of the received pulses.

uates at a higher rate than the low frequency content. Fig. 6.5(a)-6.5(b) show the pulse peak power of the received pulses and their frequency spectrum, respectively. The frequency bandwidth of the received pulse decreases as the probing range in the reservoir increases. For example, the $-20dB$ bandwidth attenuation of the received pulse for a range of $32m$ is limited to $1GHz$.

The receiver sensitivity, minimum detectable power, depends on the bandwidth of the received pulse, noise figure (NF) of the receiver, and minimum SNR requirements. The minimum power required at the receiver can be estimated by the following relationship:

$$P_{dB_m} = -174 + 10\log(BW_{Hz}) + NF_{dB} + SNR_{dB} \tag{6.1}$$

The power of the reflected pulse depends on the contrast between the dielectric constant of dry oilsand and the steam chamber. At the front face of the steam chamber, steam quickly condenses into water. The steamed area has the average dielectric constant of at least 6, which is double the dielectric constant of the dry reservoir. Based on this information, the power of the transmitted pulse for a typical steam chamber monitoring can be calculated. Here, the calculations are shown for the case of the lowest grade oilsand for $20m$ probing depth.

The minimum power required for the receiver of bandwidth $1GHz$, NF of $7dB$, with a minimum SNR of $10dB$, is $-67dBm$. According to Table. 6.3, the attenuation of pulse peak power for $20m$ propagation can be estimated as $45dB$. The reflectivity of the pulse is $-15.3dB$. The path loss due to the energy spreading is $37.5dB$. Since the boundary between the dry reservoir and steamed area is very large and continuous, the signal loss due to spreading is not required to be considered in the return path. The total loss of the signal for $20m$ down range probing is $143dB$. Therefore, the peak power of the transmitted pulse should be greater than $76dBm$.

Since the dynamics of the reservoir would not change in the time span of few seconds,

pulse averaging/integration can be applied to reduce the power requirement. Here, the received pulses can be treated as periodic pulses. If 1000 pulses are considered for integration, the required peak power of the transmitted pulse can be reduced by $30dB$. Therefore, the required peak power of the transmitted pulse is $46dBm$ i.e., $39.8W$. For a 50Ω system, the peak voltage of the pulse should be $44.6V$. The average power of the pulse will be much lower than the peak power. For example, for a pulse with pulse-width of $0.5ns$, and a pulse repetition frequency (PRF) of $1MHz$, the average power is as low as $20mW$. The limitation of the pulse integration concept is the delay that occurs during integration. For example the time delay for 1000 pulses integration with $1MHz$ PRF is $1ms$. The dynamics of the target (reservoir) should not change during this time. Hence, the reservoir monitoring can be called near real-time monitoring. The power requirements of the transmitted pulse can be further reduced by using directional antennas and pulse with lower frequency contents as discussed above.

6.5 Inhomogeneity of the Reservoir Medium

The typical height of the steam chamber growth is around $20m$. Therefore, the scanning distance, down range, of the proposed radar system is maximum $20m$ vertical from the steam injection pipe. The question here is how many inhomogeneous layers can present in the space of $20m$ that can potentially mask the steam flow imaging. In the calibration process, before steam injection, few layers of inhomogeneity can be determined. Even though boundaries of the inhomogeneity can be arbitrary in shape, in the boresight of the transceiver the boundary can be approximated as a straight line. The distance between the arrays of the transceivers, installed at the top and bottom, is always known. The medium (reservoir) electrical parameters at the location of transceiver and receiver can be measured at the time of installation.

Here, we present a simple full wave simulation to illustrate the capability of the radar

to characterize up to three layers of inhomogeneity present in the reservoir, without solving any inverse scattering problem. The simulated structure is shown in Fig. 6.6(a). To reduce the simulation time and computer resources, a scaled-down model was considered. Similar to the proposed scheme of SAGD monitoring in Fig. 6.1(a), a set of transceivers was located at the top and bottom of the reservoir for simulation. Antennas *no.*1 and *no.*3 transmitted the pulse, and the reflections were recorded at antennas *no.*2 and *no.*4, titled P_{21} and P_{43}, respectively. The received pulses are shown in Fig. 6.6(b), dashed lines. The pulse envelopes are also plotted, in solid lines, to find the right arrival time of received pulses. The oilsand

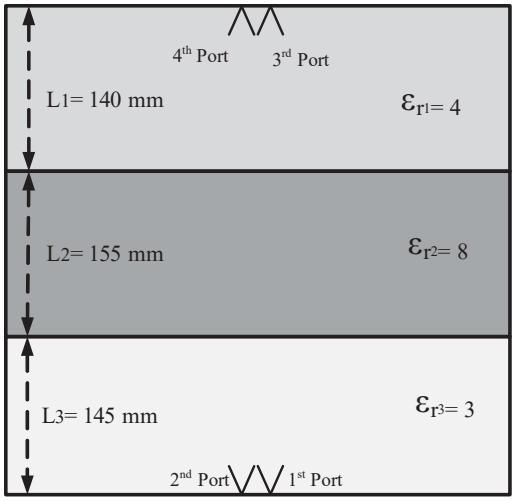

(a)

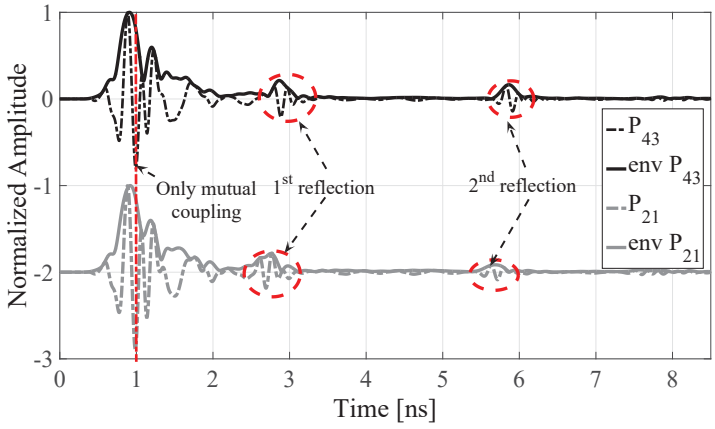

(b)

Figure 6.6: Simulation for acquiring the depth and materials in a three layered reservoir; (a) simulated structure, (b) simulated reflected pulses.

Table 6.4: Reflection time and depth of the layers

$T_1(ns)$	$T_3(ns)$	$L_1(mm)$	$L_3(mm)$
1.866	1.719	139.9	148.9

properties in the first and third layers are determined by acquiring samples during the time of installation. The depth of the first and third layers can be calculated based on the oilsand dielectric constant and round trip time of the reflected pulses. The depth of first and third layers based on the time of the reflected pulses at ports $no.2$ and $no.4$ are calculated as follows:

$$L_n = \frac{T_n.c_o}{2\sqrt{\epsilon_r}} \tag{6.2}$$

where T_n and ϵ_r are time of the reflection and medium permittivity, respectively. The time of reflections for the first and third layers is acquired from Fig. 6.6(b). The antenna mutual coupling is used as a time reference, and has to be subtracted from the time duration of the received reflection. The reflection time of the pulse and calculated depth of the layers are tabulated in Table. 6.4.

The total length is known, then by having L_1 and L_3, L_2 can be calculated. The value of L_2 is calculated to be $151.2mm$, which shows a 0.08% error. Eq. 6.2 is used again to calculate the dielectric constant of the middle layer. However, T_n is the time difference between the first and second reflections. Either P_{21} or P_{43} can be used for the dielectric constant estimation. Here, the estimated dielectric constant of 8.4 and 8.007 are the results from P_{21} and P_{43}, respectively. The average value of 8.2 is considered for the dielectric constant of the middle layer, which indicates an error of 1%. For more numbers of inhomogeneity in the reservoir, the layer thickness and dielectric constant can be estimated based on parameter optimization [38].

6.6 Mapping of Steam Chamber in SAGD Process using UWB Radar

The experiment aims at demonstrating the feasibility of mapping and localizing the steamed area, emulated steam chamber, using a UWB radar system. These experiments were done on a simplified lab prototype which is built based on dry and moisturized sand, shown in Figs. 6.7(a)-6.7(b). It is impractical to have a large oilsand sample and steaming process in our lab setting. So we used dry sand to mimic the oilsand before steam injection, and wet sand to mimic the steamed area.

In the first part of the experiment, a scaled down steam chamber shown in Fig.6.7(a) was emulated by curved shaped wet sand covered with dry sand in a plastic container. The purpose of this experiment was to see whether the shape of the emulated steam chamber can be detected by the radar. At the boundary, wet sand moisturizes the dry sand and creates a small transition zone. The height of the wet sand varied between $12cm$ to $18cm$ from the bottom of the container, and was covered with dry sand up to $30cm$ in depth, as shown in Fig. 6.7(b). To map the wet sand surface, the emulated chamber was scanned from the top over the measurement path defined in Fig. 6.7(b). Measurement was performed over the length of $45cm$, from $10cm$ to $55cm$, using UWB radar at each $5cm$ interval. However, in the actual oilsand reservoirs, the steaming pipe length may extend to $1000m$ [108], so in practical systems, scanning over the pipe length can be done at different intervals depending on required resolution.The calibrated raw data based on reflected pulses from the wet sand surface, shown in Fig. 6.7(a), was acquired along the measurement path shown in Fig. 6.7(b). The first derivative Gaussian pulse was used as an input pulse. To find the peak location of reflected pulses, the envelope of the reflected pulse is generated. Envelope detection improves the radar image resolution and its quality as it was [99]. The advantage of envelope detection for improving radar range resolution, and pulse averaging to improve the pulse SNR are discussed in Chapter. 2.

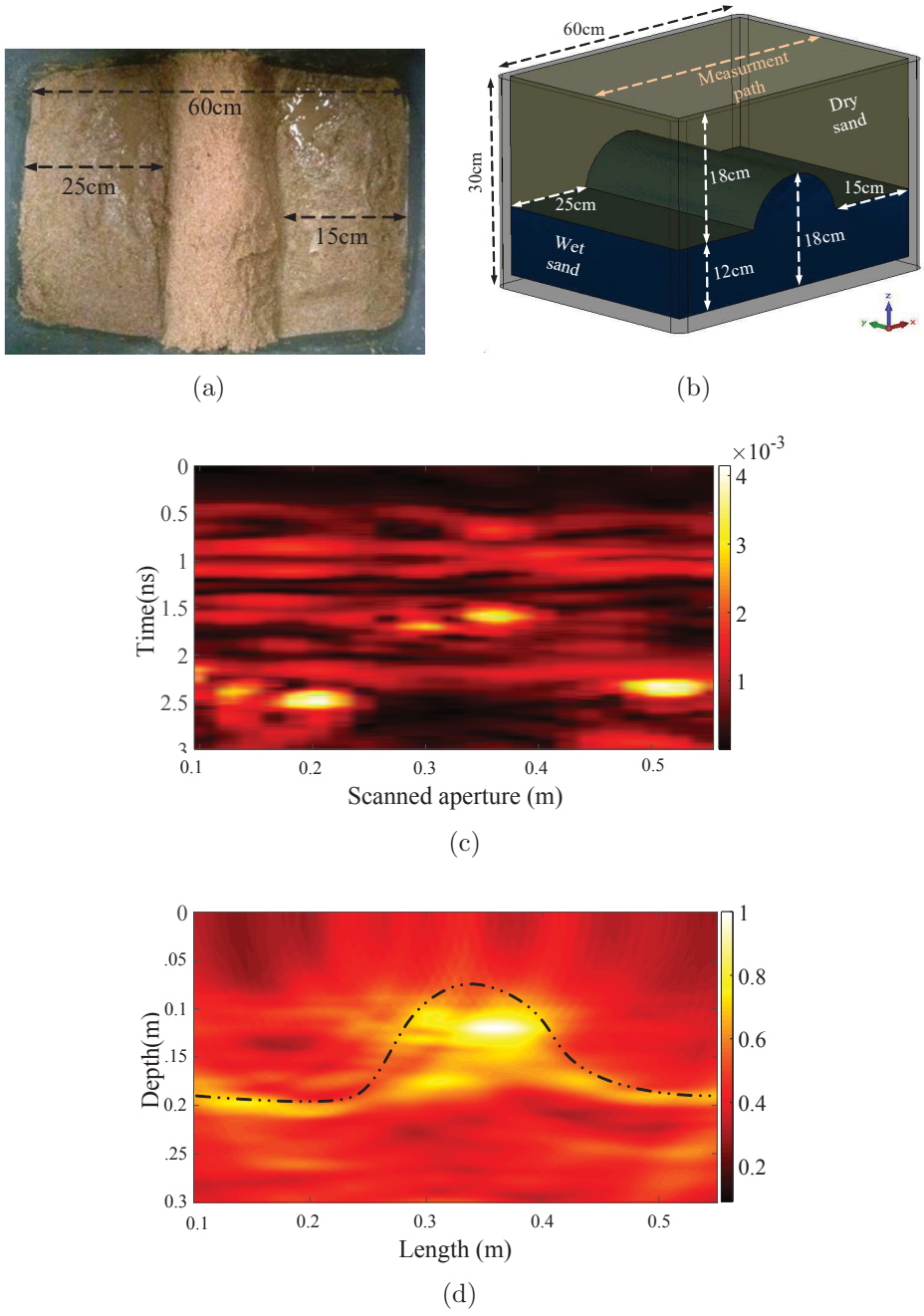

Figure 6.7: Steam chamber detection and imaging from top; (a) emulated steam chamber for measurement, (b) 3D drawing of the emulated steam chamber, (c) calibrated raw data, unit: voltage, (d) reconstructed image of the emulated steam chamber, normalized intensity.

Envelope detected raw data is shown in Fig. 6.7(c), which matches with the shape of the saturated wet sand contour shown in Figs. 6.7(a)-6.7(b). In the next step, the data is processed to reconstruct the image of the emulated steam chamber contour, i.e., wet

sand plateau. To reconstruct the image, LSAR processing is applied [27, 28, 44] which is explained in Chapter. 1. Considering the dielectric constant of 2.5, for sand, the velocity of $1.897 \times 10^8 m/s$ is used for SAR processing. The reconstructed image is shown in Fig. 6.7(d). As can be seen after SAR processing, time is translated to depth (down range), which localizes the wet sand contour.

In the first experiment, the contour of the emulated steam chamber was imaged by scanning the reservoir from the top. The purpose of the second part of the experiment is to acquire more information about the emulated steam chamber by scanning the reservoir in different lateral cuts, using reflected and through pulse propagation. The second part of the experiment is shown in Fig. 6.8(a). As demonstrated in Fig. 6.8(a), the area in the middle of the wooden box was filled with a plateau of wet sand covered by dry sand to roughly emulate the reservoir and steam chamber. To facilitate antenna movement in the sand for scanning, the TRx and Rx were enclosed in cardboard boxes filled with dry sand. In practical scenarios, an array of antennas will be arranged to acquire the data instead of moving TRx and Rx. The area was scanned by moving the TRx and Rx boxes along the wooden box length, from $10cm$ to $84cm$, at every $2cm$ in a face-to-face positions as shown in Fig. 6.8(a). To have the reference data for comparison in through mode and also for pulse calibration in reflection mode, the experiment was completed with dry sand first. The plateau of wet sand (5% moisture) is built in the middle of the dry sand, and was covered by dry sand up to the edges of the wooden box. The dimensions of the plateau are shown in Fig. 6.8(a). The plateau has a length of $40cm$ and width of $20cm$. The measurement results of the second experiment are shown in Figs. 6.8(b)-6.8(e). The measured through pulses in dry sand and the emulated chamber (dry sand including the wet sand plateau) are shown in Fig. 6.8(b)-6.8(c). By comparing these two figures, it can be concluded that the received pulses in between point $A = 21cm$ and $B = 61cm$ are delayed and attenuated due to the high dielectric constant and loss associated with the wet sand.

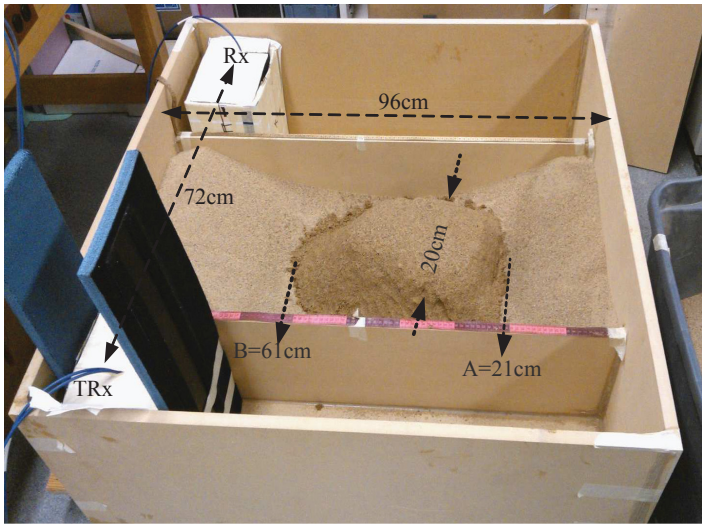
Rx
96cm
72cm
20cm
B=61cm
A=21cm
TRx

(a)

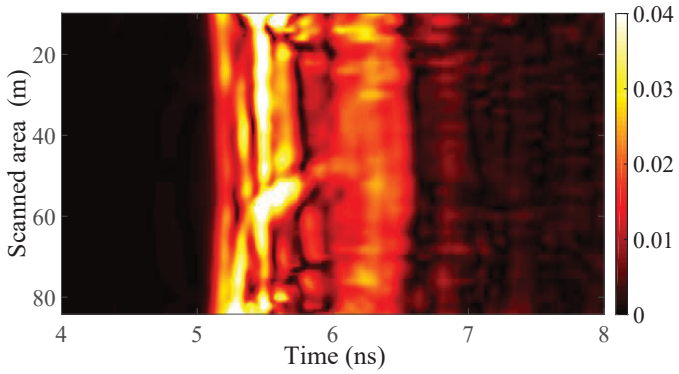
Scanned area (m)
20
40
60
80
4
5
6
7
8
Time (ns)
0.04
0.03
0.02
0.01
0

(b)

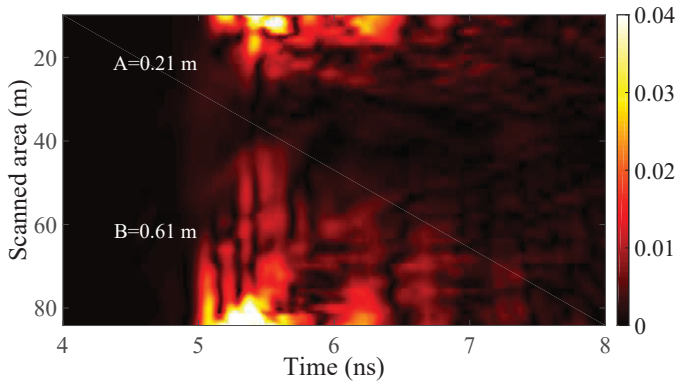
A=0.21 m
B=0.61 m
Scanned area (m)
20
40
60
80
4
5
6
7
8
Time (ns)
0.04
0.03
0.02
0.01
0

(c)

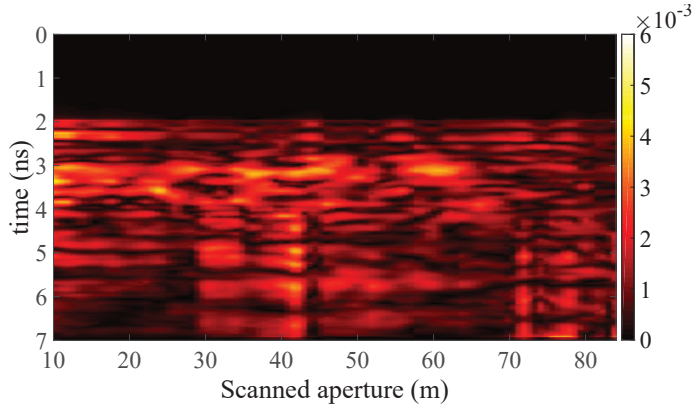

(d)

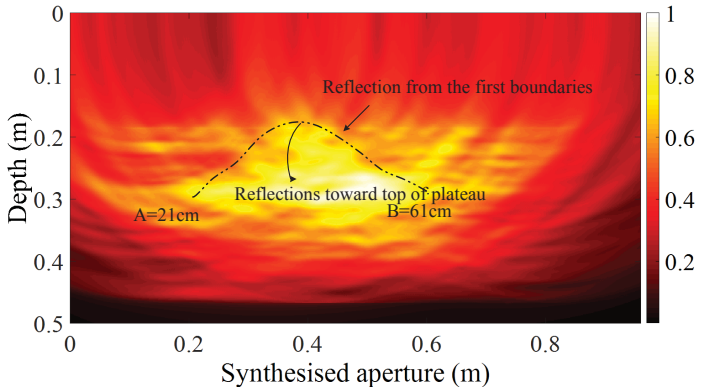

(e)

Figure 6.8: Steam chamber detection and imaging in lateral cuts; (a) emulated steam chamber, (b) measured through pulses in dry sand, unit: voltage, (c) measured through in wet sand, unit: voltage, (d) calibrated raw data of reflected measured pulse, unit: voltage, (e) reconstructed image of -d-, normalized intensity.

Hence, linking the through data attained from the reservoirs before and after steam injection can provide the information of chamber growth in the reservoir. The radar transceiver also records the reflected pulses, which can provide more information about the emulated steam chamber contours. The calibrated reflection raw data is shown in Fig. 6.8(d). Since the dielectric constant of sand in the wooden box increases gradually from dry to wet sand, several reflections occur over this transition which make the raw data very complicated to understand. Thus, we refocused the spread energy using LSAR processing. The reconstructed image is shown in Fig. 6.8(e). As can be seen, the image shows the location of the wet region clearly. It can be seen from the reconstructed images, Fig. 6.7(d) and Fig. 6.8(e), that UWB radar along with SAR processing techniques, can provide high resolution

images. The experiment results with the simplified lab prototype suggest that UWB radar techniques can be used as a method to detect and monitor the contour of steamed area.

6.7 Importance, Applicability, and Economic Feasibility of the Proposed Method

In the SAGD process, two horizontal parallel wells, with a $5m$ vertical distance, are drilled into an oilsand reservoir. Steam injected into the reservoir through the injector pipe expands in vertical and lateral directions into the reservoir to form a steam chamber. An efficient SAGD process depends on the optimal utilization of steam and creation of a uniform steam chamber along the well length. Because of the reservoir heterogeneity and its characteristics such as geometry, component distribution, porosity, permeability and the well bore undulations, preferential flow paths of steam will be formed, and the heated fluids tend to flow through the preferential paths. Therefore, a non-uniform or stunted steam chamber is inevitable in a SAGD process [124]. It should be noted that the heterogeneity in physical characteristics of an oilsand reservoir may not affect the radar signal propagation. However, heterogeneity in dielectric permittivity of the reservoir affects the speed of the signal propagation. If the steam chamber development is properly monitored and evaluated, the development of a non-uniform steam chamber can be mitigated. For example, steam splitters can be installed at underdeveloped locations of the steam chamber to enhance the development. Technologies available for monitoring the steam chamber at early stages of the SAGD process are limited. For optimizing the SAGD process, an effective technique is needed to evaluate the SAGD performance and monitor the steam chamber development. The proposed imaging method using radar principles is well suited for monitoring the steam chamber growth in near real-time. Electrical signals are transparent to physical heterogeneity, and provide contrast to the water saturation of the reservoir. Synthetic aperture radar techniques provide high resolution imaging with a minimum number of sensors. Pulse in-

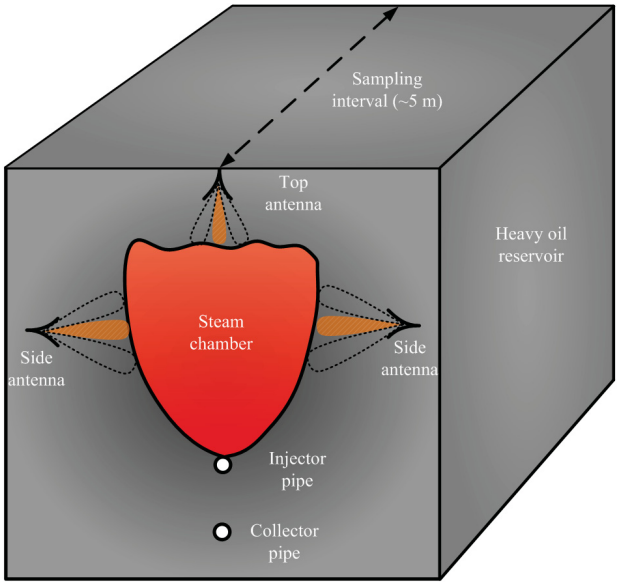

Figure 6.9: Sensor arrangement for steam chamber monitoring

tegration/averaging concepts of UWB radars are amenable for low power operations. The typical shape of the steam chamber is shown in Fig. 6.9. The steam chamber can be monitored using three arrays of sensors. One array is installed at the top of the chamber and two on the lateral sides. An additional array is installed along the injector pipe for reservoir calibration purposes. Electrical beam steering of the electromagnetic sensors, which is well understood and developed, can be used to improve the resolution of the image on the top and lateral side, as shown in the Fig. 6.9. The typical cost of a sensor would be on the order of few hundred dollars. It is expected that four sensors, one for the top, two for the lateral planes, and one along the injector pipe, will be installed for each $5m$ length of the well. For high resolution imaging, the number of sensors can be higher than what has been specified.

6.8 Conclusion

Practical considerations for utilizing UWB radar to monitor the SAGD process were comprehensively investigated. Power budget calculations and a method to characterize the lower order reservoir heterogeneity were also studied. A customized Vivaldi antenna capable of

efficiently radiating inside the oilsand was designed and used as a sensor in the measurements. Several measurement scenarios have been considered to develop the understanding of pulse propagation and characteristics in heavy oil reservoirs. Two measurement scenarios were conducted for SAGD process monitoring in horizontal and lateral cuts of the reservoir, based on reflected and through pulses. Measurement results demonstrated that UWB radar can be used to detect and image a steam chamber in the SAGD process. Monitoring the SAGD process can provide valuable feedback to optimize the consumption of water and energy.

Chapter 7

Breast Tumor Detection using UWB Circular-SAR Microwave Tomographic Imaging

7.1 Introduction

Early detection of breast cancer is the key to reducing the risk of mortality. For that reason, different imaging modalities have been developed to detect tumors in the human breast. X-ray mammography is the most commonly used method for early screening of breast cancer, as it is relatively inexpensive [125,126]. However, X-ray mammography is limited in sensitivity and in many cases fails to detect cancerous tissues in the breast [127]. In addition, the use of ionizing radiation in mammography can be harmful to patients [128]. The American Cancer Society (ACS) recently recommended reducing the frequency of mammographies for women due to drawbacks such as false detection and ionized radiation. The ACS also pointed out the necessity of having other early stage screening methods [129].

Magnetic resonance imaging (MRI) using contrast agents provides more distinctive images of the breast, especially in the case of dense breasts [130]. MRI is a safe modality

(non-ionizing). However, it is very expensive and time consuming. Therefore, MRI cannot be used as an early stage screening method. Computed tomography (CT) is a faster imaging modality. However, it uses X-rays, with a much higher dosage compared to X-ray mammography, and hence is unsafe for frequent use screening. In addition, even though CT is able to provide high spatial resolution it does not provide good soft tissue contrast [131], which is a key element for detecting tumors.

Considering the high cost, complexity, and safety aspects of current methods, microwave imaging can be a suitable candidate as an early diagnostic tool. Microwave imaging is simple, cost effective, and at the same time capable of providing a reasonable image resolution for tumor detection. The contrast in microwave imaging is based on the differences between the dielectric constant of various tissues. Extensive research has been performed, numerically and experimentally, to study the possibility of using microwave imaging for detection and localization of breast tumors. Several approaches and algorithms have been proposed. These approaches, which use active UWB microwave techniques, include methods such as confocal microwave imaging [132–135], inverse scattering [136–140], and microwave tomographic imaging [141–146]. Confocal microwave imaging focuses only on identifying the presence and location of strong scatters in the breast rather than using all the reflections to completely reconstruct the breast image. Therefore, it might lead to false detection in some cases as breast is a very complex medium. Reconstructing the breast image by solving the inverse scattering problem using iterative methods is computationally intensive and time consuming. Microwave tomographic imaging can be a supplemental method to the current modalities for breast tumor detection and imaging. Microwave tomographic imaging can also be used to study the acute and chronic functional and pathological conditions of soft tissue.

In this chapter, a combination of UWB radar techniques with CSAR processing is adopted as a tomographic imaging method for breast cancer detection. CSAR is a modified version of GBP in time domain for circular data acquisition [32]. This method is very fast and easy to implement, compared to frequency domain tomographic methods [137, 138, 146]. Since

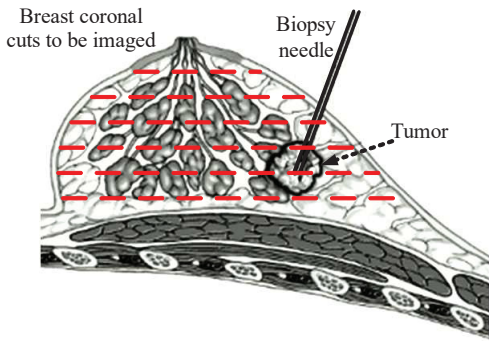

Figure 7.1: Tumorous breast with biopsy needle

both measurements and processing are done in time domain, no artifacts due to fast Fourier transform (FFT) or inverse fast Fourier transform (IFFT) are produced. The suitability of this method is experimentally demonstrated through different measurements using basic and advanced 3D printed breast phantoms. The 3D advanced breast phantom is built based on the human breast MRI and filled with liquids mimicking dielectric properties of breast tissues. The UWB-CSAR method is also applied to track a biopsy needle in a breast. Guiding a biopsy needle to the right location to acquire a tissue sample is very important since the needle samples a tiny region as shown in Fig. 7.1.

This chapter is organized as follows. First, the design of breast phantoms used in the experiments is described. The data acquisition method and the radar specifications are outlined. A discussion on group velocity is presented afterwards. The experimental results and reconstructed images of phantoms are demonstrated in the last section.

7.2 Breast Model and Phantom

Having an appropriate phantom is the key to validate the imaging technique before it can be applied to a human subject. Generally, the human breast, as shown in Fig. 7.2(a), consists of three different tissues: adipose, glandular, and fibro connective tissues [3]. Every breast consists of different percentages of each of these tissues. However, the breast tissues can be categorized in three groups, which are shown in Table. 7.1 [2]. The dielectric constant of a

Table 7.1: Electrical properties of breast tissues in different categories [2].

	$5GHz$		$10GHz$	
Electrical properties	ϵ_r	$\delta(S/m)$	ϵ_r	$\delta(S/m)$
0-30% adipose tissue 100-70% glandular I	44	4	36	12
31-84% adipose tissue 70-16% glandular II	36	3	30	7.5
85-100% adipose tissue 0-15% glandular,III	4.5	0.2	4.1	0.48
Malignant tissue	55	5.5	44	14.5

breast tissue has a direct relationship to the percentage of glandular tissue. The dielectric constant of the malignant tissue is also shown in the Table. 7.1. The contrast between malignant tissue and other tissues in a breast in terms of the dielectric constant can be detected by electromagnetic waves. Different measurement scenarios are considered to evaluate the merit of UWB-CSAR method. The data in this table is used to prepare two different breast phantoms, called basic and advanced, which are explained in the next two subsections.

7.2.1 Basic phantom: pork fat

The basic breast phantom is built using pork fat, and is shaped by a plastic cup as shown in Fig. 7.3(a). The basic phantom emulates the third group of the breast category, shown in Table. 7.1, as the dielectric constant of this group is very close to that of the pork fat ($\epsilon_r = 3.82$ at $5GHz$). In order to model the tumor, for the basic phantom, an orange lobe is placed inside the phantom. Due to high water content, the orange lobe has approximately the same dielectric properties as cancerous tissue. We also investigated the possibility of detecting and tracking a biopsy needle inside a breast using UWB-CSAR. The biopsy needle was represented by a copper wire with a diameter of $1.3mm$, as shown in Fig.7.3(b).

7.2.2 Complex phantom: 3D printed phantom

The advanced breast phantom is printed by 3D technology using acrylonitrile butadiene styrene (ABS) plastic ($\epsilon_r = 2.25$) based on the real MRI images of a patient's breast [147]. The interior distribution of tissues for a real breast is mimicked accurately in this phantom

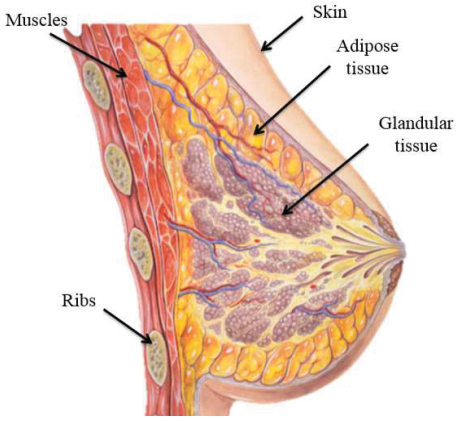

(a)

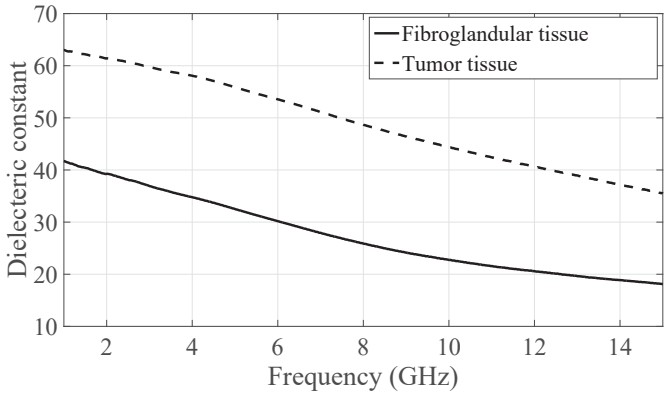

(b)

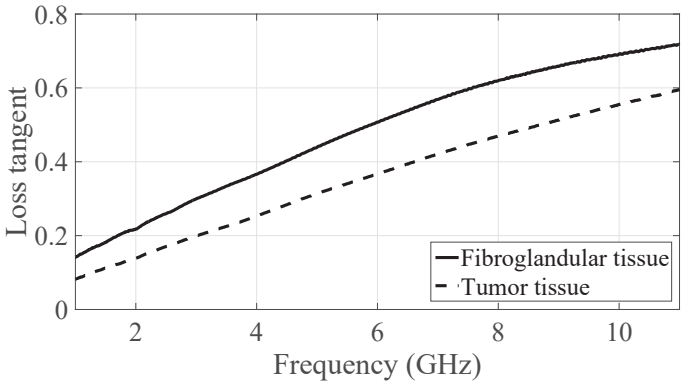

(c)

Figure 7.2: (a) Sagittal slices of the human breast anatomy, the original image is taken from: West Coast Surgical Oncology. (b) Measured dielectric constant, (c) loss tangent, versus frequency for mimicking solutions used for breast phantom.

as the phantom is filled with solutions emulating glandular tissues. The solution consists of polyethylene glycol mono phenyl ether (Triton X-100) and deionized water, which was first

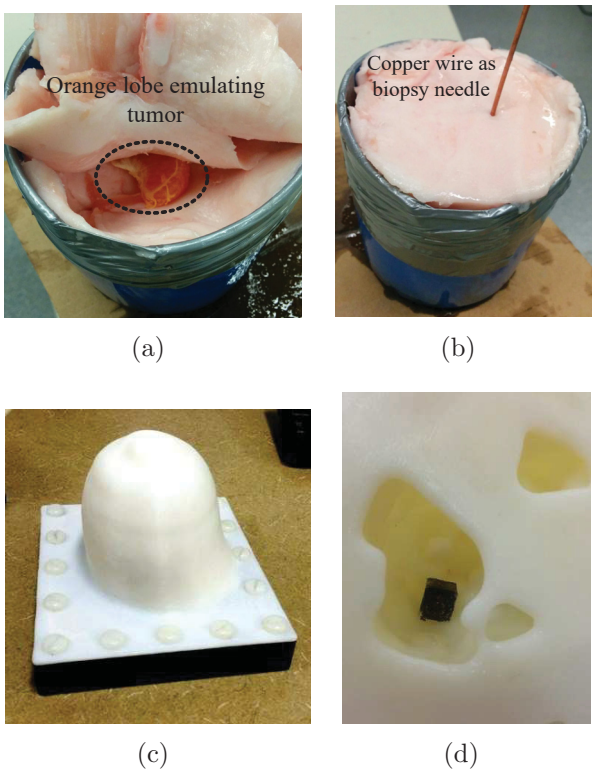

Figure 7.3: Breast phantoms to perform measurement scenarios: (a) simple breast phantom with pork fat and orange lobe, $2cm \times 1cm \times 1cm$, emulating tumor, (b) measurement set-up for simple phantom, (c) 3D printed phantom, (d) emulated tumor using a $1cm^3$ plastic container filled with mimicking solution.

used in [3]. In this study, we considered the second group in Table. 7.1 due to the fact that more patients fall into this category. The mixing solutions to emulate breast tissues are a mixture of deionized water and Triton X-100. The mixing ratios for the second group, glandular and malignant tissues, are summarized in Table. 7.2. The solution emulating tumor was enclosed by a thin plastic container as shown in Fig. 7.3(c). The dielectric properties of the simulated breast solutions were verified using a dielectric probe ($85070E$) from Keysight Technologies, and are plotted in Fig. 7.2(b)-7.2(c).

Table 7.2: Mimicking solutions for tissues inside the 3D printed phantom [3].

Mixture	Deionized water	Triton X-100
Glandular tissue, Type II	60 %	40 %
Malignant tissue	80 %	20 %

7.3 UWB Radar System Specifications and Raw data Acquisition

The radar system and Gaussian pulse demonstrated in Fig. 1.6(b) and Fig. 1.6(c) were employed used as input pulses during the measurements. A pair of Vivaldi antennas, shown in Fig. 1.7(b), are used as TRx antennas for this experiment. The antennas are capable of efficiently radiating within the matching liquid, which is vegetable oil with a dielectric constant of 3. The radar transceiver was immersed in vegetable oil during the experiment as shown in Fig.7.4. The transmitted pulse has $125ps$ pulse width and $10mW$ peak power. Pulse averaging was used to increase the pulse SNR. In these measurements, we used 64 pulses for averaging at $1MHz$ PRF. The average power for each measured pulse is $1.25\mu W$, which is significantly below the power level radiated by cell phones ($0.1 - 2W$ according to World Health Organization, Fact sheet $N°193$). The safe power levels and specific absorption rate have been extensively studied in [148], which confirms the safety of the microwave imaging technique.

7.3.1 Raw data acquisition and calibration

The first step is to acquire raw data. To do that, the breast phantom is placed in the middle of a plastic container inside the matching liquid, as shown in Fig. 7.4(b). The raw data, for a slice, is collected by rotating the radar and recording the received pulses at every 5°, covering 360°. Increasing the number of angle steps enhances the image quality however it increases the data acquisition and image reconstruction time. The 5° angle increment found to be a good trade-off for this measurement setup. In order to do 3D image reconstruction for a clinical system, the measurements should be done faster by employing more number of transverses to cover all slices and angles.

The raw data has to be calibrated before the image reconstruction procedure is performed. To calibrate the raw data, the ambient pulse which captures the effects of antennas

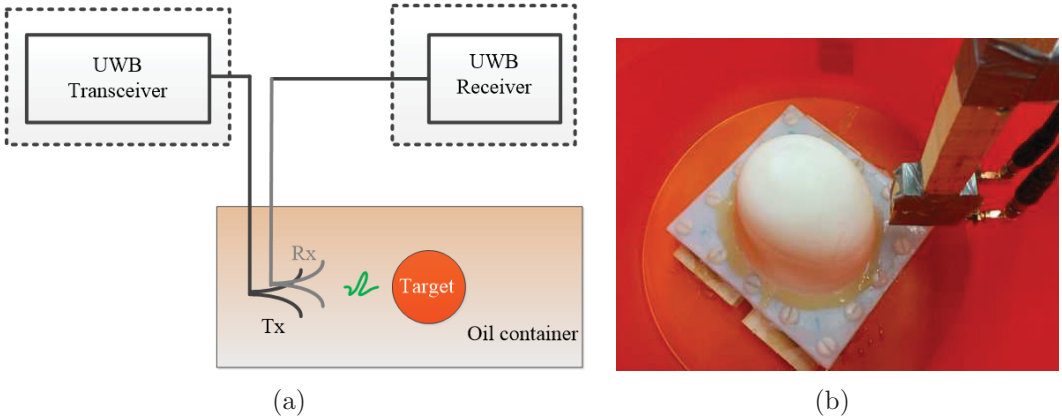

Figure 7.4: (a) UWB radar system schematic, (b) measurement setup.

and container, has to be removed from the received pulse. Here, the ambient pulse was measured by sending and receiving a pulse into the matching liquid container in the absence

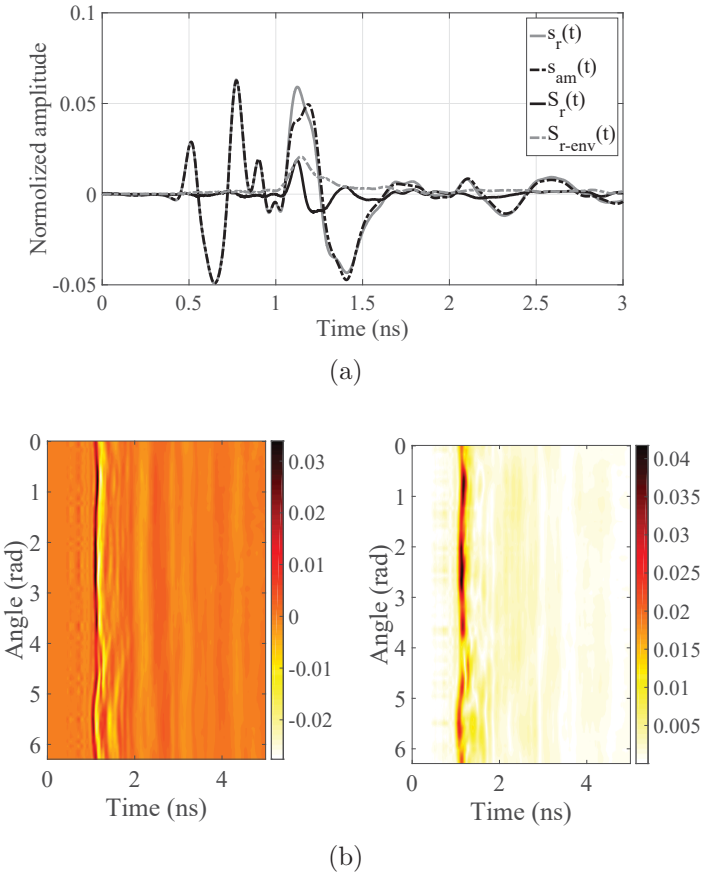

Figure 7.5: (a) Calibration procedure, (b) calibrated measured raw data sinogram, left: received pulses, right: envelope of the received pulses.

of the breast phantom. By subtracting the ambient signal from the received pulse, all effects including nearby objects and antenna mutual coupling are removed. The calibration procedure for the basic phantom, without a tumor, at a location is shown in Fig. 7.5(a). As can be seen, up to $1ns$, the received and ambient pulses are almost the same, which is due to the mutual coupling of the antenna. After this point there are changes in the pulse shape, between these two pulses, which are due to the presence of the breast phantom. The solid gray line is the target signature and the dashed gray line is its envelope. The sinogram of the calibrated raw data and its envelope are shown in the left and right illustrations in Fig. 7.5(b), respectively. The same dataset was also generated for each phantom, for different cases, in this study.

7.4 Group Velocity Estimation in a Multilayer Dielectric Medium

Group velocity plays a very important role in time domain image reconstruction methods. To reconstruct the image of a complex medium like a human breast, the group velocity considered in signal processing has to be as close as possible to the effective group velocity in the medium to minimize errors. Generally, image reconstruction is done with the effective group velocity of the complex breast medium. However, in the reconstructed image, the dimensions of high and low dielectric constant regions appear larger and smaller, respectively. To understand this phenomenon more specifically the pulse propagation, interlayer reflections, and image reconstruction for a simplified breast model are numerically studied here. The model is built based on three concentric cylindrical layers as shown in Fig. 7.6(a). Each layer has a different dielectric constant, simulating the breast tissues in this case, and the whole structure is enclosed in a container with oil. The dielectric constants of different materials are shown in Fig. 7.6(b). The same Vivaldi antennas used to conduct the measurements were also used for simulations. The locations of reflections at different layers in

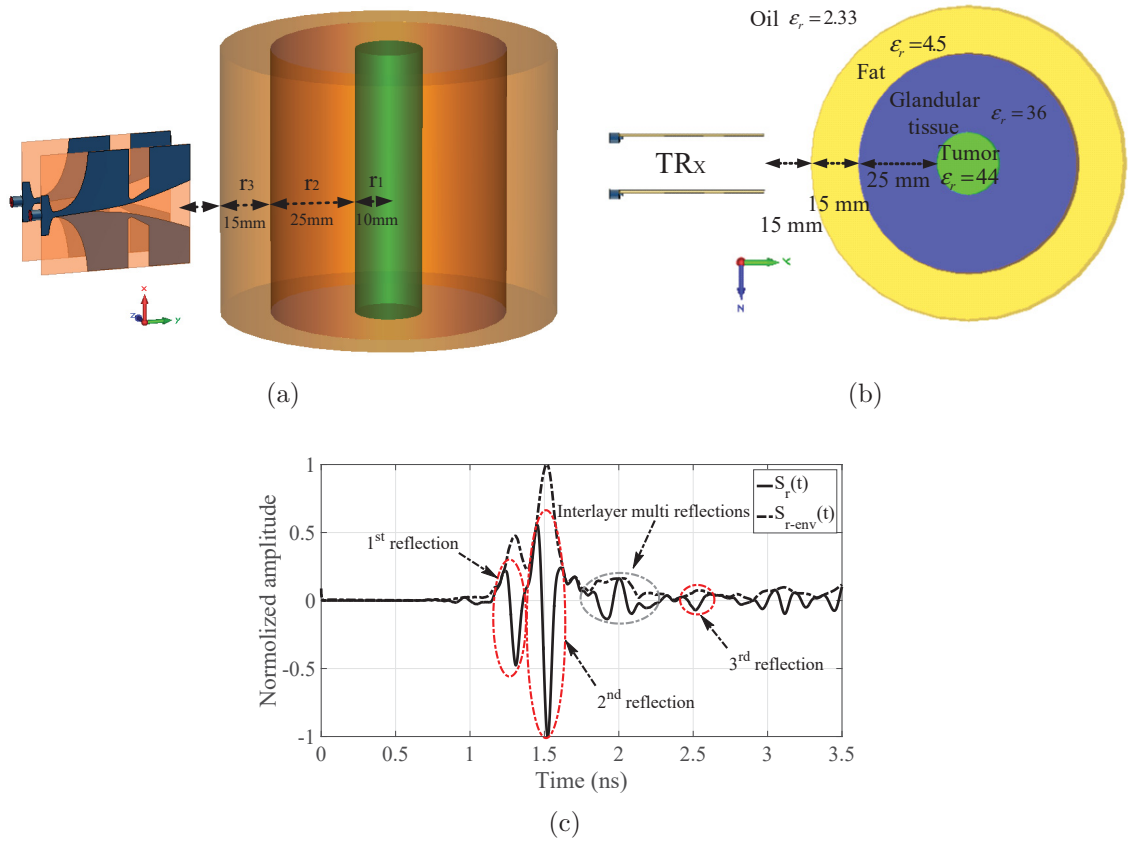

Figure 7.6: (a) simulated structure for evaluating group velocity of a multilayer structure, (b) top view, (c) calibrated pulse and its envelope at angle of 0°.

raw data are marked in Fig. 7.6(c). The first and second reflections are due to oil/fat and fat/glandular tissue interferences, respectively. The last reflection is due to the boundary between the glandular and tumor tissues. The reflections located between the second and third reflections are due to internal layers, which are highlighted by the dark dotted circle.

The shape of the received pulse depends on the antenna transfer function, material of the target, and the number of reflections that the pulse undergoes [36, 51]. In our case, as the input pulse is the first derivative Gaussian pulse, the received pulse should be the second derivative Gaussian pulse. This knowledge is helpful for identifying the interlayer reflections. The interlayer reflections do not provide any additional information to the reconstructed image; however, they might degrade the image quality. Therefore time gating shall be applied to remove the undesired effects.

To reach the tumor, the pulse goes through three different group velocities: oil, fat, and glandular tissues. The image can be reconstructed using the effective group velocity in the medium. In this case the average group velocity is calculated relative to the cylinders' radii as follows:

$$\epsilon_{r-ave} = \frac{\epsilon_{r_1} r_1 + \epsilon_{r2} r_2 + \epsilon_{r_3} r_3}{r_1 + r_2 + r_3} \tag{7.1}$$

where ϵ_r and r are the permittivity and thickness of the internal layers. In this case, the average permittivity is 18.2. The reconstructed images of the model are shown in Fig. 7.7. As shown, the shapes of concentric cylinders are reconstructed in the image. It should be noted that in the reconstructed image, the radius of the outer cylinder and the thickness of the fat layer are smaller than the actual dimensions in the model. This is due to the effective group velocity is slower that the actual group velocities in those regions. Similarly, the second cylinder, simulating the glandular tissue region, appeared larger than its actual dimensions. To obtain the actual dimensions in the reconstructed image, the group velocity in processing has to be the same as the actual group velocity in each regions. However, this is very complicated with human breast as the target, as it is a very complex medium.

The CSAR image can be reconstructed by using other combinations of the group velocity and reconstructed image size. For example, if we want the size of the reconstructed image to be larger than the actual size of the phantom, the group velocity considered in processing has to be higher than the effective group velocity in the medium which magnifies the image [41]. Here the image of the cylinders is reconstructed by setting the image size to $15cm$ instead of $6cm$ as was defined in the simulations. The reconstructed images shown in Fig. 7.8 are reconstructed with a group velocity 2.5 times faster than the effective group velocity. This technique can be used to magnify the reconstructed images if required.

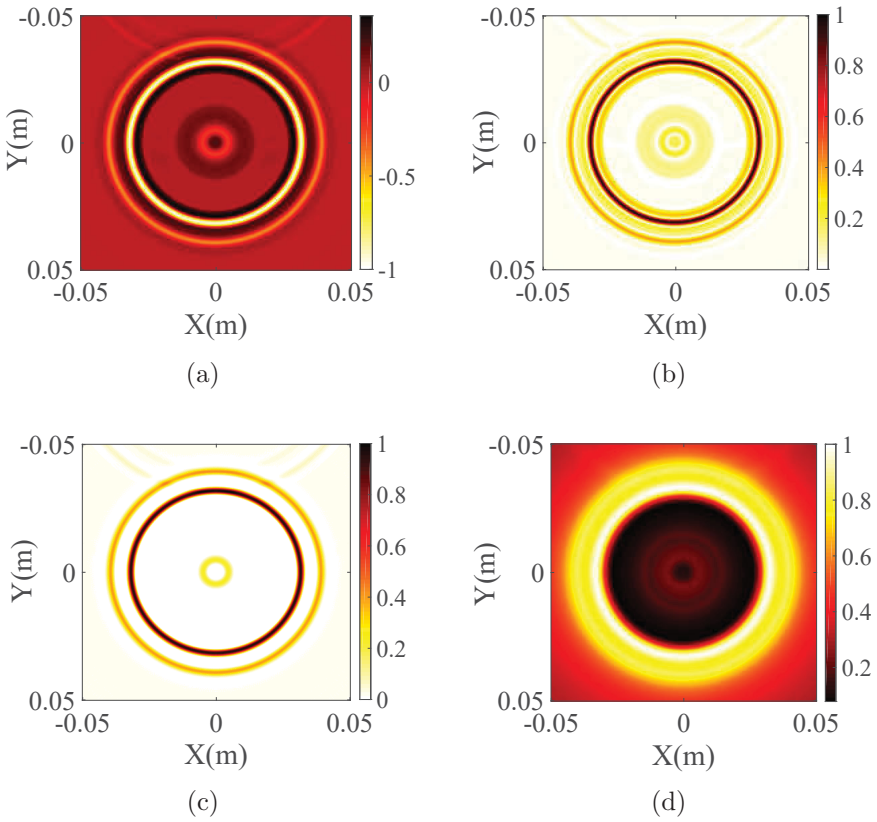

Figure 7.7: Reconstructed images of the multilayer dielectric structure with $6cm \times 6cm$ image size; (a) real image, (b) absolute image, (c) positive image, (d) envelop image.

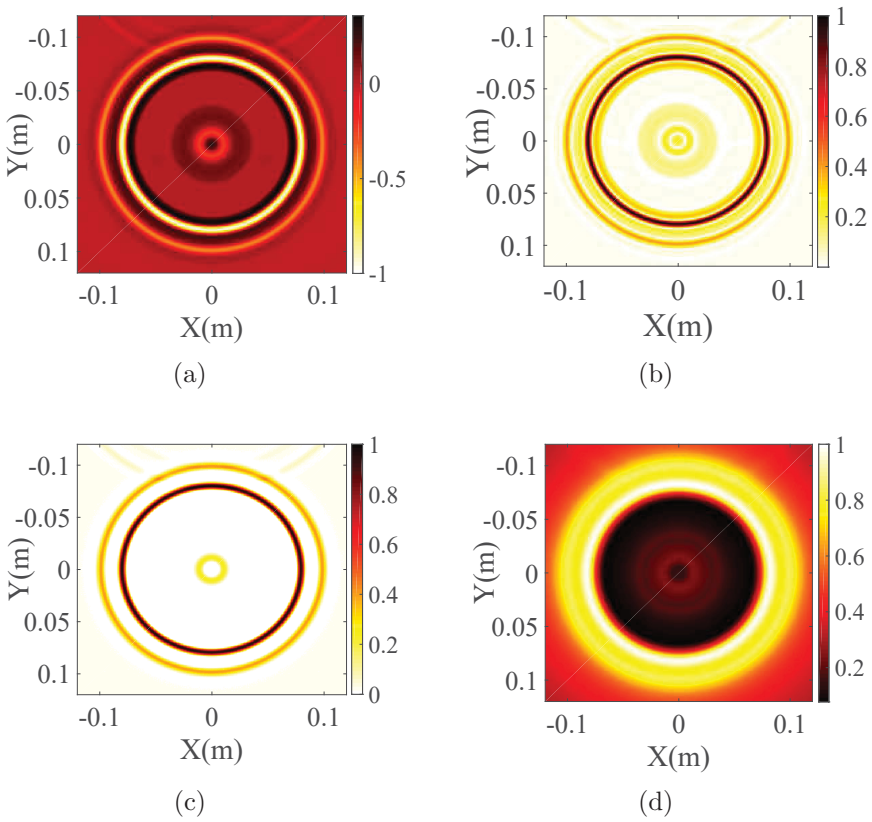

Figure 7.8: Reconstructed images of the multilayer dielectric structure with $15cm \times 15cm$ image size; (a) real image, (b) absolute image, (c) positive image, (d) envelope image.

7.5 Reconstructed Images of Phantoms

In this section, the reconstructed images of the basic and advanced phantoms are presented and discussed. The experiments are done for different scenarios. The basic phantom is scanned in both healthy and cancerous conditions and also with a biopsy needle inserted in the breast phantom. In the last experiment, the advanced phantom, which contains a $1cm^3$ emulated tumor, was scanned. Similar to the simulation results, real, absolute, positive, and envelope images are reconstructed.

7.5.1 Basic phantom: healthy and tumorous conditions

The reconstructed images of the basic phantom in healthy and cancerous conditions are shown in Fig. 7.9 The images are reconstructed in the area of $14cm \times 14cm$ ($7cm$ radius). Time gating was applied to the raw data to remove the reflection due to the first boundary between oil and pork fat. The images shown in Fig. 7.9(a)-7.9(d) show the healthy phantom with hot spots in the reconstructed images. The hot spots are due to layers of pork fat and pieces of flesh connected to the fat inside the phantom. This image is considered as a reference for comparison. The reconstructed images of the cancerous phantom are shown in Fig. 7.9(e)-7.9(h). As shown, everything is the same except for another hot spot, which is marked on the figures. Information can be extracted from the different image formats (real, absolute, positive, and envelope). The tumor is detected more clearly in the positive image, shown in Fig. 7.9(g). The tumor location can also be seen as a dark spot in the envelope image.

7.5.2 Basic phantom: biopsy needle imaging

During a breast examination, if an abnormality is detected, a biopsy of the abnormal mass is performed using a biopsy needle. As part of the biopsy process, a small sample of tumor tissue is removed to be inspected by a pathologist in order to determine the tumor type and

grade, as well as the hormone receptor status. Missing the tumor in a biopsy procedure will lead to false results; hence it is critical to visualize the location of the needle inside the breast. Typically, a biopsy needle is guided by either ultrasound or X-ray guided stereotactic technology which is difficult to visualize correctly [149, 150].

The introduced UWB-CSAR can be used to detect a biopsy needle inside a breast as well [151] which provides a microwave imaging package for both screening and biopsy needle tracking. The contrast between a metallic needle and human breast tissues is ideal for electromagnetic pulses.

The reconstructed images of the phantom with copper wire, as biopsy needle, are shown in Figs. 7.10(a)-7.10(d). As can be seen, the wire is localized in all images. The contrast in the positive images is superior compared to the other three images. For the purpose of tracking the needle, the exact location of the needle can be found by finding the maximum intensity along a profile in the envelope image.

7.5.3 Advanced phantom with tumor

The reconstructed images of the advanced phantom are presented in this section. The phantom structure in different views is shown in Fig. 7.11(a). A $1cm^3$ plastic thin container, filled with solution emulating a tumor, was located in the middle of phantom affixed to the ABS wall as shown in the 3D view. The tumor container is made of a thin plastic, half a millimeter thickness, with negligible affects on the operating frequency bandwidth. The phantom is also shown at different cuts, the bottom view and a cut at tumor height. To acquire the raw data, the advanced phantom was also scanned in the same way as the basic phantom. The images are reconstructed in the $10cm \times 10cm$ area, ($5cm$ radius). The reconstructed images are shown in Fig. 7.11(b)-Fig. 7.11(e). The outline of the breast phantom appears as two dark and bright circles, since the pulse has negative and positive parts, and also because of the discontinuity between the matching liquid and ABS plastic. The tumor is detected as a dark rectangular spot in the top right of Fig. 7.11(b). Other

reflections and contours inside the circle are due to the discontinuity inside the phantom. To sharpen the image, the positive image, shown in Fig. 7.11(c), is generated by subtracting the real image from the absolute image. The tumor is detected as a rectangular shape which is marked in all images. The envelope image, Fig. 7.11(e), shows the tumor location in the breast phantom as well. Using UWB radar imaging can generate different types of images that provide sufficient information to specialists, which can help them to make accurate decisions. The precision of the reconstructed images of the advanced phantom using UWB-CSAR imaging demonstrates the proficiency of this technique.

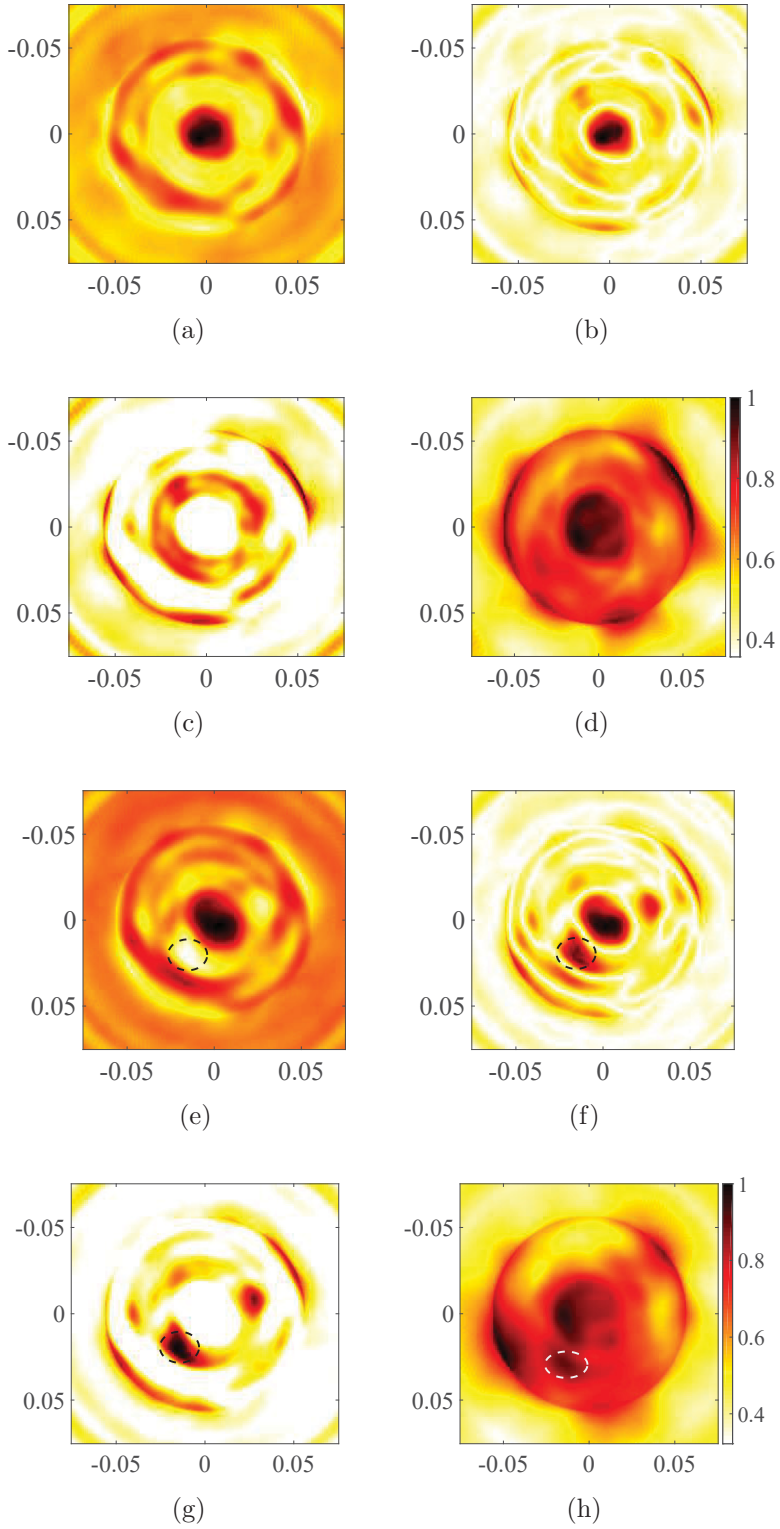

Figure 7.9: Healthy basic phantom; (a) real image, (b) absolute image, (c) positive image, (d) envelope image. Basic phantom with an emulated tumor; (e) real image, (f) absolute image, (g) positive image, (h) envelop image.

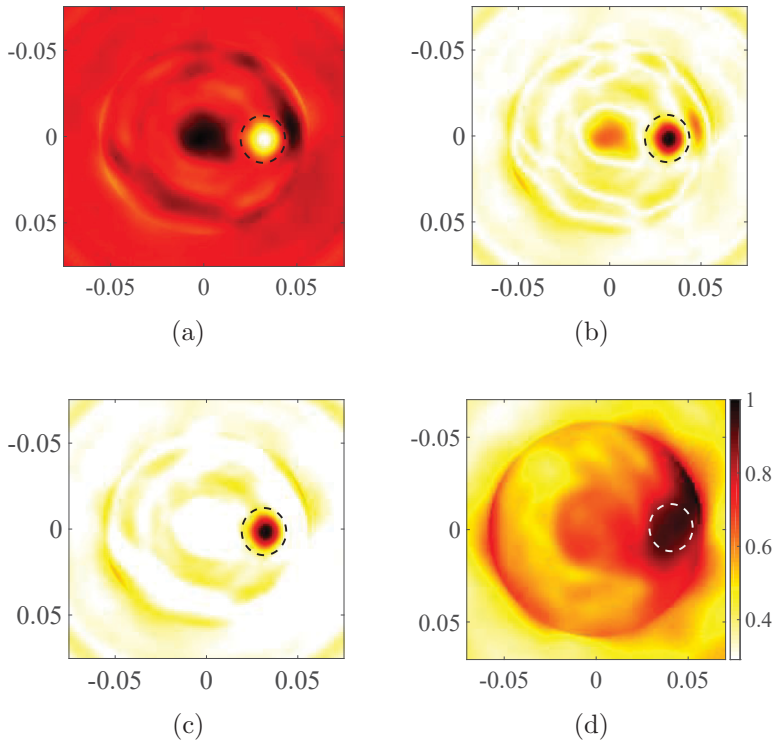

Figure 7.10: Biopsy needle inside the basic phantom reconstructed images; (a) real image, (b) absolute image, (c) positive image, (d) envelop image.

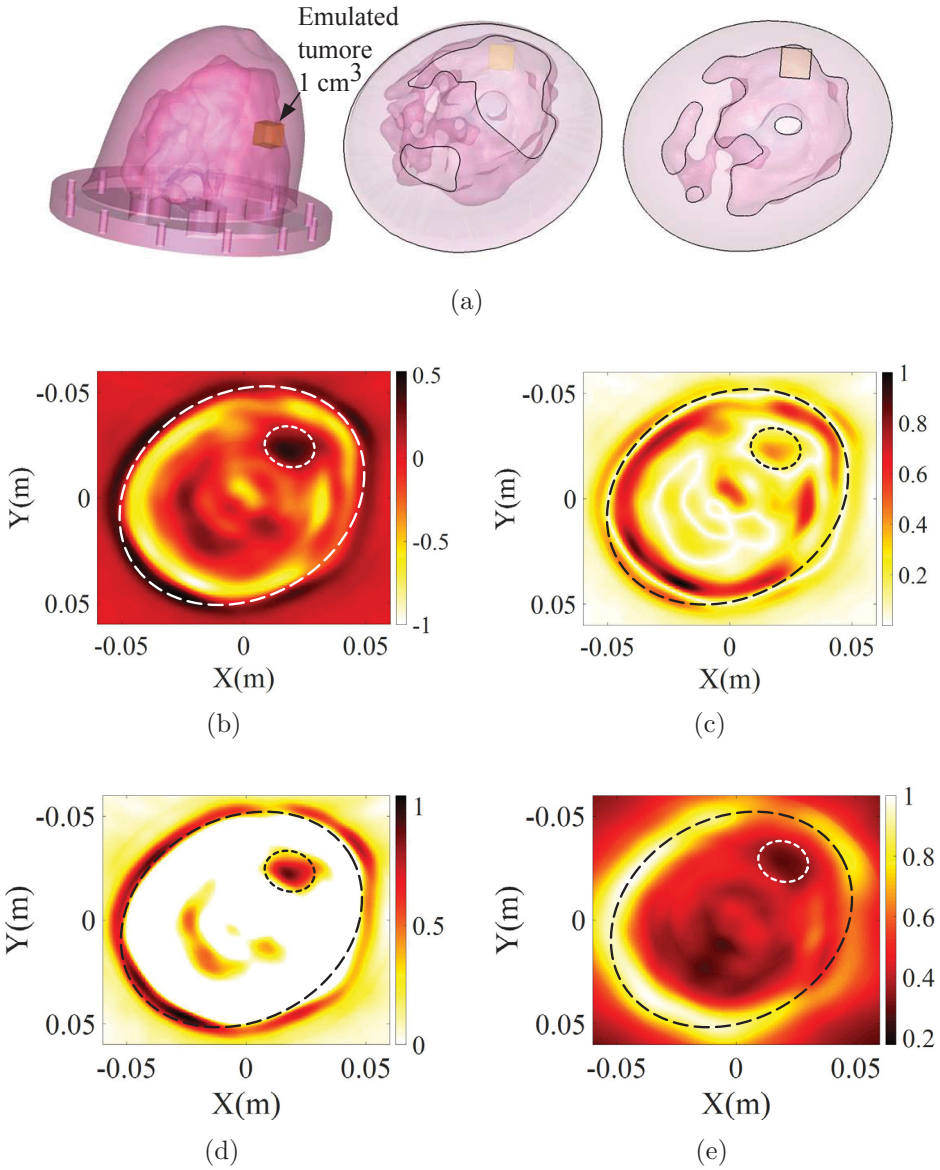

Figure 7.11: Cancerous advanced phantom; (a) transparent phantom in different views (the cube region is the simulated tumorous tissue), (b) real image (c) absolute image, (d) positive image, (e) envelop image.

7.6 Conclusion

Breast microwave imaging using UWB-CSAR was presented in this chapter. Breast phantom images were reconstructed with the time domain global back projection algorithm. Signal processing techniques such as envelope detection and positive image subtraction were used to improve image quality. The preliminary results from measurements demonstrated the potential of UWB-CSAR as a future method for human breast screening, yet more study and developments need to be done.

Moreover, detecting and imaging a biopsy needle using microwave imaging was investigated. Unlike the traditional breast imaging methods such as MRI and CT-scan, microwave imaging can be used in real-time monitoring to guide the biopsy needle toward the tumor using simple and inexpensive equipment. The simulation and measurement results proved the suitability of the presented UWB-CSAR method for imaging the human breast. This will significantly impact the medical field by enhancing early cancer detection, as UWB-CSAR is cost effective and safe.

Chapter 8

Conclusions and Future Works

8.1 Conclusion

In this thesis, theoretical and practical aspects of UWB radars for imaging applications, especially in the near-field, is systematically established and scrutinized. The capability of UWB radar systems for high resolution imaging of oil reservoir monitoring and breast cancer screening applications were specifically investigated through several simulations and measurements. It was shown that time domain UWB radars is an efficient imaging technique for oil reservoir monitoring and also a cheaper and safer imaging technique for early screening of breast cancer.

8.2 Future Works

8.2.1 UWB radar systems with varying bandwidth tailored to a specific application

Since our pulse generator operates from 1 to $11GHz$, all the aforementioned applications had to be performed with the same radar operational bandwidth and center frequency. However, the system performance will be optimal if the frequency bandwidth is assigned based on the

application requirements such as, resolution, path losses and size limitations. For instance, for SAGD process monitoring resolution is not as important as path losses since heavy oil reservoir has significant electrical loss and long probing range is required. As explained, in Chapter. 6, a radar system with $500MHz$ bandwidth with the highest frequency component below $1GHz$ would provide the required range resolution for steam chamber imaging with less required input power.

In order to detect and image small perforations, oil well monitoring systems have to be high resolution as well as compact size to be able to fit inside the borehole. Here, resolution is a very important factor to attain higher quality images with more details of the perforations. Since the required detection range in oil well is short, on the order of few centimeters, and crude oil is not as lossy as oilsand, millimeter wave UWB radar systems can be an ideal solutions for oil well perforation imaging.

8.2.2 UWB radar system with multiple receivers for detecting targets with low RCS and less pronounced dielectric contrast

Complex targets, e.g. breast tumor, in a complicated medium such as breast are very hard to detect. Most fatal breast tumors have intricate shapes and are located in the glandular tissues which results in low dielectric contrast for radar detection. The complex shape of the tumor and low contrast with background medium results in weak reflections at different angles and therefore detection failure. Multiple receivers located at different angles/locations around the breast collect weak signals reflected by the tumor for effective detection and imaging. To design a multiple receiver UWB radar system, several receiver configurations should be studied in order to obtain an optimal receiving function.

8.2.3 Industrialization of the developed UWB technologies for oil reservoir and breast cancer imaging

The ultimate goal of this research is the industrialization of the developed time domain UWB technology for oil reservoir and breast cancer imaging. To achieve this goal, the custom designed radar system has to be experimented in a real oil reservoirs. Moreover clinical trials are required to evaluate the practicality of the system for breast imaging applications.

Bibliography

[1] S. Thompson, B. Askildsen, and A. Gervasi, "Apparatus and method to identify targets through opaque barriers," Apr. 5 2011, US Patent 7,920,088. [Online]. Available: http://www.google.com/patents/US7920088

[2] M. Lazebnik, L. McCartney, D. Popovic, C. B. Watkins, M. J. Lindstrom, J. Harter, S. Sewall, A. Magliocco, J. H. Booske, M. Okoniewski *et al.*, "A large-scale study of the ultrawideband microwave dielectric properties of normal breast tissue obtained from reduction surgeries," *Physics in medicine and biology*, vol. 52, no. 10, p. 2637, 2007.

[3] S. Romeo, L. Di Donato, O. M. Bucci, I. Catapano, L. Crocco, M. R. Scarfi, and R. Massa, "Dielectric characterization study of liquid-based materials for mimicking breast tissues," *Microwave and Optical Technology Letters*, vol. 53, no. 6, pp. 1276–1280, 2011.

[4] M. Miorali, E. Slob, and R. Arts, "A feasibility study of borehole radar as a permanent downhole sensor," in *Geophysical Prospecting*, vol. 59, 2011, pp. 120–131.

[5] E. C. Fear and M. A. Stuchly, "Microwave system for breast tumor detection," *IEEE Microwave and Guided Wave Letters*, vol. 9, no. 11, pp. 470–472, Nov 1999.

[6] M. Skolnik, *Radar Handbook, Third Edition*. McGraw-Hill Education, 2008.

[7] M. Lazarus, "Radar everywhere," *IEEE Spectrum*, vol. 52, no. 2, pp. 52–59, February 2015.

[8] G. Angino, F. Impagnatiello, and C. Zelli, "High spatial resolution radar altimetry for global earth topography mapping," in *Geoscience and Remote Sensing, 1997. IGARSS '97. Remote Sensing - A Scientific Vision for Sustainable Development., 1997 IEEE International*, vol. 1, Aug 1997, pp. 15–17.

[9] M. Pieraccini, M. Fratini, F. Parrini, G. Macaluso, and C. Atzeni, "High-speed CW step-frequency coherent radar for dynamic monitoring of civil engineering structures," *Electronics Letters*, vol. 40, no. 14, pp. 907–908, July 2004.

[10] E. M. Staderini, "UWB radars in medicine," *IEEE Aerospace and Electronic Systems Magazine*, vol. 17, no. 1, pp. 13–18, Jan 2002.

[11] M. Yeary, B. L. Cheong, J. M. Kurdzo, T.-Y. Yu, and R. Palmer, "A brief overview of weather radar technologies and instrumentation," *IEEE Instrumentation Measurement Magazine*, vol. 17, no. 5, pp. 10–15, Oct 2014.

[12] F. Zhenhe, Z. Jun, and W. Yi, "The HAL-3 airborne navigation radar," *IEEE Transactions on Aerospace and Electronic Systems*, vol. 32, no. 3, pp. 1208–1211, July 1996.

[13] C. Fowler, J. Entzminger, and J. Corum, "Assessment of ultra-wideband (UWB) technology," *IEEE Aerospace and Electronic Systems Magazine*, vol. 5, no. 11, pp. 45–49, Nov 1990.

[14] K. K. M. Chan, A. E. C. Tan, and K. Rambabu, "Circularly polarized ultra-wideband radar system for vital signs monitoring," *IEEE Transactions on Microwave Theory and Techniques*, vol. 61, no. 5, pp. 2069–2075, May 2013.

[15] J. D. Taylor, *Ultra-wideband radar technology*. CRC press, 2000.

[16] J. Li, L. Liu, Z. Zeng, and F. Liu, "Advanced signal processing for vital sign extraction with applications in UWB radar detection of trapped victims in complex environ-

ments," *IEEE Journal of Selected Topics in Applied Earth Observations and Remote Sensing*, vol. 7, no. 3, pp. 783–791, March 2014.

[17] K. K. M. Chan, A. E. C. Tan, L. Li, and K. Rambabu, "Material characterization of arbitrarily shaped dielectrics based on reflected pulse characteristics," *IEEE Transactions on Microwave Theory and Techniques*, vol. 63, no. 5, pp. 1700–1709, May 2015.

[18] J. Park and C. Nguyen, "An ultrawide-band microwave radar sensor for nondestructive evaluation of pavement subsurface," *IEEE Sensors Journal*, vol. 5, no. 5, pp. 942–949, Oct 2005.

[19] A. Scuderi, E. Ragonese, and G. Palmisano, "24GHz ultra-wideband transmitter for vehicular short-range radar applications," *IET Circuits, Devices Systems*, vol. 3, no. 6, pp. 313–321, December 2009.

[20] K. Chan, "Robust contactless sensor for real-time vital signs monitoring," Ph.D. dissertation, University of Alberta. Department of Electrical and Computer Engineering, 2014.

[21] I. Immoreev and J. Taylor, "Ultrawideband radar special features and terminology," *Aerospace and Electronic Systems Magazine, IEEE*, vol. 20, no. 5, pp. 13–15, May 2005.

[22] Y. J. Ren, C. P. Lai, P. H. Chen, and R. M. Narayanan, "Compact ultrawideband UHF array antenna for through-wall radar applications," *IEEE Antennas and Wireless Propagation Letters*, vol. 8, pp. 1302–1305, 2009.

[23] *FCC First Report and Order: In the matter of Revision of Part 15 of the Commission's Rules Regarding Ultra-Wideband Transmission Systems.* FCC, April 2002.

[24] C. Balanis, *Antenna theory: Analysis and design, 3rd Ed.* Wiley India Pvt. Limited, 2009.

[25] Y. K. Chan and V. C. Koo, "An introduction to synthetic aperture radar (SAR)," *Progress In Electromagnetics Research B*, vol. 2, pp. 27–60, 2008.

[26] A. Kak and M. Slaney, *Principles of Computerized Tomographic Imaging*, ser. Classics in Applied Mathematics. Society for Industrial and Applied Mathematics, 2001. [Online]. Available: https://books.google.ca/books?id=Z6RpVjb9_lwC

[27] D. Oloumi, "Oil Well Monitoring by Ultra-wideband Ground Penetrating Synthetic Aperture Radar," Master's thesis, Blekinge institute of technology, Karlskrona, Sweden, 2012.

[28] L.-E. Andersson, "On the determination of a function from spherical averages," *SIAM Journal on Mathematical Analysis*, vol. 19, no. 1, pp. 214–232, 1988.

[29] M. Soumekh, *Synthetic Aperture Radar Signal Processing with MATLAB Algorithms*, ser. Wiley-Interscience publication. Wiley, 1999.

[30] J. A. Parker, R. V. Kenyon, and D. E. Troxel, "Comparison of interpolating methods for image resampling," *IEEE Transactions on Medical Imaging*, vol. 2, no. 1, pp. 31–39, March 1983.

[31] S. Tretter, *Communication System Design Using DSP Algorithms: With Laboratory Experiments for the TMS320C6713^{TM} DSK*, ser. Information Technology: Transmission, Processing and Storage. Springer Verlag, 2008.

[32] D. Oloumi, P. Boulanger, A. Kordzadeh, and K. Rambabu, "Breast tumor detection using UWB circular-SAR tomographic microwave imaging," in *IEEE Engineering in Medicine and Biology Society (EMBC), 2015 37th Annual International Conference*, Aug 2015, pp. 7063–7066.

[33] D. Oloumi, M. Pettersson, D. Elliott, and P. Mousavi, "A TEM horn antenna with non-uniform expansion for oil well monitoring," in *Antennas and Propagation Society International Symposium (APSURSI), 2012 IEEE*, July 2012, pp. 1–2.

[34] D. Oloumi, P. Mousavi, M. I. Pettersson, and D. G. Elliott, "A modified TEM horn antenna customized for oil well monitoring applications," *IEEE Transactions on Antennas and Propagation*, vol. 61, no. 12, pp. 5902–5909, Dec 2013.

[35] D. Oloumi, K. K. M. Chan, P. Boulanger, and K. Rambabu, "SAGD process monitoring in heavy oil reservoir using UWB radar techniques," *IEEE Transactions on Microwave Theory and Techniques*, vol. 64, no. 6, pp. 1884–1895, June 2016.

[36] K. Rambabu, A. E. C. Tan, K. K. M. Chan, and M. Y. W. Chia, "Estimation of antenna effect on ultra-wideband pulse shape in transmission and reception," *IEEE Transactions on Electromagnetic Compatibility*, vol. 51, no. 3, pp. 604–610, Aug 2009.

[37] J. Li, Z. Zeng, J. Sun, and F. Liu, "Through-wall detection of human being's movement by UWB radar," *IEEE Geoscience and Remote Sensing Letters*, vol. 9, no. 6, pp. 1079–1083, 2012.

[38] L. Li, A. E. C. Tan, K. Jhamb, and K. Rambabu, "Buried object characterization using ultra-wideband ground penetrating radar," *IEEE Transactions on Microwave Theory and Techniques*, vol. 60, no. 8, pp. 2654–2664, Aug 2012.

[39] V. Venkatasubramanian, H. Leung, and X. Liu, "Chaos UWB radar for through-the-wall imaging," *IEEE Transactions on Image Processing*, vol. 18, no. 6, pp. 1255–1265, June 2009.

[40] G. Charvat, L. C. Kempel, E. Rothwell, C. Coleman, and E. Mokole, "A through-dielectric radar imaging system," *IEEE Transactions on Antennas and Propagation*, vol. 58, no. 8, pp. 2594–2603, Aug 2010.

[41] D. Oloumi, M. Pettersson, P. Mousavi, and K. Rambabu, "Imaging of oil-well perforations using UWB synthetic aperture radar," *IEEE Transactions on Geoscience and Remote Sensing*, vol. 53, no. 8, pp. 4510–4520, Aug 2015.

[42] D. Winters, J. Shea, E. Madsen, G. Frank, B. Van Veen, and S. Hagness, "Estimating the breast surface using UWB microwave monostatic backscatter measurements," *IEEE Transactions on Biomedical Engineering*, vol. 55, no. 1, pp. 247–256, Jan 2008.

[43] E. C. Fear, J. Bourqui, C. Curtis, D. Mew, B. Docktor, and C. Romano, "Microwave breast imaging with a monostatic radar-based system: A study of application to patients," *IEEE Transactions on Microwave Theory and Techniques*, vol. 61, no. 5, pp. 2119–2128, May 2013.

[44] V. T. Vu, T. K. Sjögren, M. I. Pettersson, and A. Gustavsson, "Definition on SAR image quality measurements for UWB SAR," vol. 7109, Proc.SPIE Image and Signal Processing for Remote Sensing XIV, pp. 1–9, 2008.

[45] V. Vu, T. Sjogren, M. Pettersson, and H. Hellsten, "An impulse response function for evaluation of UWB SAR imaging," *IEEE Transactions on Signal Processing*, vol. 58, no. 7, pp. 3927–3932, July 2010.

[46] S. Azevedo and T. McEwan, "Micropower impulse radar," *IEEE Potentials*, vol. 16, no. 2, pp. 15–20, April 1997.

[47] A.-C. Tan, K. Jhamb, and K. Rambabu, "Design of transverse electromagnetic horn for concrete penetrating ultrawideband radar," *IEEE Transactions on Antennas and Propagation*, vol. 60, no. 4, pp. 1736–1743, April 2012.

[48] K.-M. Chan, A.-C. Tan, and K. Rambabu, "Decade bandwidth circularly polarized antenna array," *IEEE Transactions on Antennas and Propagation*, vol. 61, no. 11, pp. 5435–5443, Nov 2013.

[49] A. E. C. Tan, M. Y. W. Chia, and K. Rambabu, "Design of ultra-wideband monopulse receiver," *IEEE Transactions on Microwave Theory and Techniques*, vol. 54, no. 11, pp. 3821–3827, Nov 2006.

[50] M. Kanda, "Time domain sensors for radiated impulsive measurements," *IEEE Transactions on Antennas and Propagation*, vol. 31, no. 3, pp. 438–444, May 1983.

[51] L. Li, A.-C. Tan, K. Jhamb, and K. Rambabu, "Characteristics of ultra-wideband pulse scattered from metal planar objects," *IEEE Transactions on Antennas and Propagation*, vol. 61, no. 6, pp. 3197–3206, June 2013.

[52] B. Mahafza, *Radar Systems Analysis and Design Using MATLAB Second Edition*. Taylor & Francis, 2005.

[53] N. Pena, G. Garza, Y. Cao, and Z. Qiao, "Edge detection of real synthetic aperture radar images through filtered back projection," in *2012 International Conference on Systems and Informatics (ICSAI)*, May 2012, pp. 1910–1913.

[54] K.-M. Chan, K. Rambabu, A.-C. Tan, and M.-W. Chia, "Efficient passive low-rate pulse generator for ultra-wideband radar," *IET Microwaves, Antennas Propagation*, vol. 4, no. 12, pp. 2196–2199, December 2010.

[55] J. Bai, S. Shi, and D. W. Prather, "Modified compact antipodal vivaldi antenna for 4-50-GHz UWB application," *IEEE Transactions on Microwave Theory and Techniques*, vol. 59, no. 4, pp. 1051–1057, April 2011.

[56] P. Fei, Y.-C. Jiao, W. Hu, and F.-S. Zhang, "A miniaturized antipodal vivaldi antenna with improved radiation characteristics," *IEEE Antennas and Wireless Propagation Letters*, vol. 10, pp. 127–130, 2011.

[57] Computer simulation technology, "CST MICROWAVE STUDIO." [Online]. Available: https://www.cst.com/products/cstmws

[58] L. Wang, A. Kuzmich, and A. Dogariu, "Gain-assisted superluminal light propagation," *Nature*, vol. 406, no. 6793, pp. 277–279, 2000.

[59] S. Chu and S. Wong, "Linear pulse propagation in an absorbing medium," *Physical review letters*, vol. 48, no. 11, p. 738, 1982.

[60] D. Mugnai, A. Ranfagni, and L. Ronchi, "The question of tunneling time duration: A new experimental test at microwave scale," *Physics letters A*, vol. 247, no. 4, pp. 281–286, 1998.

[61] P. Balcou and L. Dutriaux, "Dual optical tunneling times in frustrated total internal reflection," *Physical review letters*, vol. 78, no. 5, p. 851, 1997.

[62] A. Ranfagni, D. Mugnai, P. Fabeni, and G. Pazzi, "Delay-time measurements in narrowed waveguides as a test of tunneling," *Applied physics letters*, vol. 58, no. 7, pp. 774–776, 1991.

[63] D. Mugnai, A. Ranfagni, and R. Ruggeri, "Observation of superluminal behaviors in wave propagation," *Physical review letters*, vol. 84, no. 21, p. 4830, 2000.

[64] I. Alexeev, K. Kim, and H. Milchberg, "Measurement of the superluminal group velocity of an ultrashort bessel beam pulse," *Physical review letters*, vol. 88, no. 7, p. 073901, 2002.

[65] J. Lloyd, K. Wang, A. Barkan, and D. M. Mittleman, "Characterization of apparent superluminal effects in the focus of an axicon lens using terahertz time-domain spectroscopy," *Optics communications*, vol. 219, no. 1, pp. 289–294, 2003.

[66] Z.-Y. Wang, Y. Guo, H. Yang, and Q. Qiu, "A heuristic explanation for the superluminal behaviors of evanescent waves," in *Photonics and Optoelectronics (SOPO), 2012 Symposium on*. IEEE, 2012, pp. 1–4.

[67] W. D. Walker, "Superluminal near-field dipole electromagnetic fields," *arXiv preprint physics/0001063*, 2000.

[68] ——, "Experimental evidence of near-field superluminally propagating electromagnetic fields," in *Gravitation and Cosmology: From the Hubble Radius to the Planck Scale*. Springer, 2002, pp. 189–196.

[69] J. C.-E. Sten and A. Hujanen, "Aspects on the phase delay and phase velocity in the electromagnetic near-field," *Progress In Electromagnetics Research*, vol. 56, pp. 67–80, 2006.

[70] D. Jones, I. Sneddon, S. Ulam, and M. Stark, *The Theory of Electromagnetism*. Elsevier Science, 2013. [Online]. Available: https://books.google.ca/books?id=9aBGBQAAQBAJ

[71] D. G. Long, "Comments on hilbert transform based signal analysis," 2004.

[72] N. A. Cartwright and K. E. Oughstun, "Pulse centroid velocity of the poynting vector," *JOSA A*, vol. 21, no. 3, pp. 439–450, 2004.

[73] D.-H. Kwon, "Effect of antenna gain and group delay variations on pulse-preserving capabilities of ultrawideband antennas," *IEEE Transactions on antennas and propagation*, vol. 54, no. 8, pp. 2208–2215, 2006.

[74] A. V. Oppenheim and R. W. Schafer, *Discrete-time signal processing*. Pearson Higher Education, 2010.

[75] F. Civan, *Reservoir Formation Damage*. Elsevier Science, 2015. [Online]. Available: https://books.google.ca/books?id=MO6cBAAAQBAJ

[76] H. Alboudwarej, K. Akbarzadeh, J. Beck, W. Y. Svrcek, and H. W. Yarranton, "Regular solution model for asphaltene precipitation from bitumens and solvents," *AIChE Journal*, vol. 49, no. 11, pp. 2948–2956, 2003.

[77] P. Cheung, A. Hayman, R. Laronga, G. Cook, G. Flournoy, P. Goetz, M. Marshall, S. Hansen, M. Lamb, B. Li *et al.*, "A clear picture in oil-base muds," *Oilfield Review*, vol. 13, no. 4, pp. 2–27, 2001.

[78] B. E. Hornby and D. J. Rossi, "Single well sonic imaging of near borehole structure," in *Multidimensional Signal Processing Workshop, 1989., Sixth.* IEEE, 1989, p. 45.

[79] J. Dudley *et al.*, "Quantitative fracture identification with the borehole televiewer," in *SPWLA 34th Annual Logging Symposium.* Society of Petrophysicists and Well-Log Analysts, 1993.

[80] L. E. San Martin, W. J. Schaecher, and M. L. Monroe, "Permittivity measurements with oil-based mud imaging tool," Feb. 15 2011, US Patent 7,888,941.

[81] D. J. Daniels, *Ground penetrating radar.* Wiley Online Library, 2005.

[82] H. Jol, *Ground Penetrating Radar Theory and Applications.* Elsevier Science, 2008. [Online]. Available: https://books.google.ca/books?id=y_uIi-5RvgC

[83] J. Huisman, S. Hubbard, J. Redman, and A. Annan, "Measuring soil water content with ground penetrating radar," *Vadose zone journal*, vol. 2, no. 4, pp. 476–491, 2003.

[84] D. L. Wright, R. D. Watts, and E. Bramsoe, "A short-pulse electromagnetic transponder for hole-to-hole use," *IEEE Transactions on Geoscience and Remote Sensing*, no. 6, pp. 720–725, 1984.

[85] M. Sato and R. Thierbach, "Analysis of a borehole radar in cross-hole mode," *IEEE Transactions on Geoscience and Remote Sensing*, vol. 29, no. 6, pp. 899–904, 1991.

[86] T. M. Habashy and J. Xia, "Borehole logging tools and methods using reflected electromagnetic signals," Jun. 25 1996, US Patent 5,530,359.

[87] W. C. Chew, "Modeling of the dielectric logging tool at high frequencies: theory," *IEEE Transactions on Geoscience and Remote Sensing*, vol. 26, no. 4, pp. 382–387, Jul 1988.

[88] S. Liu and M. Sato, "Electromagnetic logging technique based on borehole radar," *IEEE transactions on geoscience and remote sensing*, vol. 40, no. 9, pp. 2083–2092, 2002.

[89] S. Liu, M. Sato, and K. Takahashi, "Application of borehole radar for subsurface physical measurement," *Journal of Geophysics and Engineering*, vol. 1, no. 3, p. 221, 2004.

[90] I. M. Mason, A. J. Bray, T. G. Sindle, C. M. Simmat, and J. H. Cloete, "The effect of conduction on VHF radar images shot in water-filled boreholes," *IEEE Geoscience and Remote Sensing Letters*, vol. 5, no. 2, pp. 304–307, 2008.

[91] Y.-H. Chen and M. L. Oristaglio, "A modeling study of borehole radar for oil-field applications," *Geophysics*, vol. 67, no. 5, pp. 1486–1494, 2002.

[92] Y. Chen and M. Oristaglio, "Borehole radar for oil-field imaging: A study based on numerical modeling," *Schlumberger-Doll Res., Ridgefield, CT, USA, Int. Res. Rep*, 1998.

[93] C. Guo and R. C. Liu, "A borehole imaging method using electromagnetic short pulse in oil-based mud," *IEEE Geoscience and Remote Sensing Letters*, vol. 7, no. 4, pp. 856–860, 2010.

[94] M. Miorali, F. Zhou, E. Slob, and R. Arts, "Coupling ground penetrating radar and fluid flow modeling for oilfield monitoring applications," *Geophysics*, vol. 76, no. 3, pp. A21–A25, 2011.

[95] S. J. Wilburn, "Plugging formations with asphalt," Jul. 28 1959, US Patent 2,896,716.

[96] W. Renpu, *Advanced well completion engineering*. Gulf Professional Publishing, 2011.

[97] M. Miorali, *Borehole radar for oil production monitoring*. TU Delft, Delft University of Technology, 2012.

[98] D. Oloumi and K. Rambabu, "Studying the superluminal behavior of UWB antennas and its effect on near-field imaging," *IEEE Transactions on Antennas and Propgations*, vol. Accepted with Major revision, 2016.

[99] D. Oloumi, J. W. Ting, and K. Rambabu, "Design of pulse characteristics for near-field uwb-sar imaging," *IEEE Transactions on Microwave Theory and Techniques*, vol. 64, no. 8, pp. 2684–2693, Aug 2016.

[100] S. S. Prabha, R. J. Rathish, R. Dorothy, G. Brindha, M. Pandiarajan, A. Al-Hashem, and S. Rajendran, "Corrosion problems in petroleum industry and their solution," *European Chemical Bulletin*, vol. 3, no. 3, pp. 300–307, 2014.

[101] D. Brondel, R. Edwards, A. Hayman, D. Hill, S. Mehta, and T. Semerad, "Corrosion in the oil industry," *Oilfield review*, vol. 6, no. 2, pp. 4–18, 1994.

[102] G. Frisch, B. Mandal *et al.*, "Advanced ultrasonic scanning tool and evaluation methods improve and standardize casing inspection," in *SPE Annual Technical Conference and Exhibition*. Society of Petroleum Engineers, 2001.

[103] C. E. Robison *et al.*, "Overcoming the challenges associated with the life cycle management of multilateral wells: Assessing moves towards the" intelligent well"," in *Offshore Technology Conference*. Offshore Technology Conference, 1997.

[104] D. R. Brouwer, *Dynamic water flood optimization with smart wells using optimal control theory*. TU Delft, Delft University of Technology, 2004.

[105] F. Nyhavn, F. Vassenden, P. Singstad *et al.*, "Reservoir drainage with downhole permanent monitoring and control systems. real-time integration of dynamic reservoir

performance data and static reservoir model improves control decisions," in *SPE Annual Technical Conference and Exhibition*. Society of Petroleum Engineers, 2000.

[106] M. Miorali, E. Slob, and R. Arts, "Feasibility of borehole radar measurements to monitor water/steam fronts in eor applications," in *71st EAGE Conference and Exhibition incorporating SPE EUROPEC 2009*, 2009.

[107] R. Butler, *Thermal recovery of oil and bitumen*. Prentice Hall, 1991. [Online]. Available: https://books.google.ca/books?id=_6RTAAAAMAAJ

[108] Q. Chen, "Assessing and improving steam-assisted gravity drainage: Reservoir heterogeneities, hydraulic fractures, and mobility control foams," Ph.D. dissertation, Stanford University, Department Energy Resources Engineering, 2009.

[109] T. Cyr, R. Coates, and M. Polikar, "Steam-assisted gravity drainage heavy oil recovery process," July 2001, US Patent 6,257,334.

[110] P. Egermann, G. Renard, E. Delamaide *et al.*, "SAGD performance optimization through numerical simulations: Methodology and field case example," in *SPE International Thermal Operations and Heavy Oil Symposium*. Society of Petroleum Engineers, 2001.

[111] Q. Jiang, B. Thornton, J. Russel-Houston, S. Spence *et al.*, "Review of thermal recovery technologies for the clearwater and lower grand rapids formations in cold lake, alberta," *Journal of Canadian Petroleum Technology*, vol. 49, no. 9, pp. 57–68, 2010.

[112] G. R. Scott *et al.*, "Comparison of css and SAGD performance in the clearwater formation at cold lake," in *SPE International Thermal Operations and Heavy Oil Symposium and International Horizontal Well Technology Conference*. Society of Petroleum Engineers, 2002.

[113] P. Meum, P. Tøndel, J.-M. Godhavn, O. M. Aamo *et al.*, "Optimization of smart well production through nonlinear model predictive control," in *Intelligent Energy Conference and Exhibition*. Society of Petroleum Engineers, 2008.

[114] S. Maxwell, J. Rutledge, R. Jones, and M. Fehler, "Petroleum reservoir characterization using downhole microseismic monitoring," *Geophysics*, vol. 75, no. 5, pp. 75A129–75A137, 2010.

[115] M. Duncan Peter and L. Eisner, "Reservoir characterization using surface microseismic monitoring," *Geophysics*, vol. 75, no. 5, pp. 139–146, 2010.

[116] P. McGillivray, "Microseismic and time-lapse seismic monitoring of a heavy oil extraction process at peace river, canada," *CSEG Recorder*, vol. 30, no. 1, pp. 5–9, 2005.

[117] M. Miorali, E. Slob, R. Arts *et al.*, "A modeling study of a borehole radar system as a permanent down-hole sensor," in *2009 SEG Annual Meeting*. Society of Exploration Geophysicists, 2009.

[118] A. M. Abbosh, "Miniaturized microstrip-fed tapered-slot antenna with ultrawideband performance," *IEEE Antennas and Wireless Propagation Letters*, vol. 8, pp. 690–692, 2009.

[119] J. Malherbe and N. Barnes, "TEM horn antenna with an elliptic profile," *Microwave and Optical Technology Letters*, vol. 49, no. 7, pp. 1548–1551, 2007.

[120] C. M. d. J. van Coevorden, A. R. Bretones, M. F. Pantoja, F. J. G. Ruiz, S. G. Garcia, and R. G. Martin, "GA design of a thin-wire bow-tie antenna for GPR applications," *IEEE Transactions on Geoscience and Remote Sensing*, vol. 44, no. 4, pp. 1004–1010, 2006.

[121] L. E. Gonzalez, P. Ficocelli, T. X. Bostick *et al.*, "Real time optimization of SAGD wells," in *SPE Heavy Oil Conference Canada*. Society of Petroleum Engineers, 2012.

[122] L. Erdogan, C. Akyel, and F. M. Ghannouchi, "sands at 2.45 GHz with $TE_{1,0,11}$ mode determined by a rectangular cavity resonator," *Journal of Microwave Power and Electromagnetic Energy*, vol. 45, no. 1, pp. 15–23, 2011.

[123] J. Zou, R. Lu, T. Karumudi, A, and S. X, "Application of ultra-wide band (UWB) radar in detecting unexpected utility lines in open cut operations," in *Proceedings of the 30th ISARC*, 2013, pp. 1197–1207.

[124] L. Zhu, F. Zeng, and Y. Huang, "A correlation of steam chamber size and temperature falloff in the early-period of the SAGD process," *Fuel*, vol. 148, pp. 168–177, 2015.

[125] J. Elmore, K. Armstrong, C. Lehman, and S. Fletcher, "Screening for breast cancer," *JAMA*, vol. 293, no. 10, pp. 1245–1256, 2005.

[126] C. H. Lee, D. D. Dershaw, D. Kopans, P. Evans, B. Monsees, D. Monticciolo, R. J. Brenner, L. Bassett, W. Berg, S. Feig *et al.*, "Breast cancer screening with imaging: recommendations from the society of breast imaging and the acr on the use of mammography, breast mri, breast ultrasound, and other technologies for the detection of clinically occult breast cancer," *Journal of the American college of radiology*, vol. 7, no. 1, pp. 18–27, 2010.

[127] A. Nnewihe, E. Staroswiecki, N. Bangerter, and B. Hargreaves, "Dual tuned Helmholtz coil for breast cancer imaging," in *Proc. Intl. Soc. Mag. Reson*, 2008.

[128] E. J. Hall and D. J. Brenner, "Cancer risks from diagnostic radiology," *The British Journal of Radiology*, vol. 81, pp. 362–378, 2008.

[129] D. Grady, "American cancer society, in a shift, recommends fewer mammograms," *The New York Times*, Oct, 20th, 2015.

[130] G. I. Andreea, R. Pegza, L. Lascu, S. Bondari, Z. Stoica, and A. Bondari, "The role of imaging techniques in diagnosis of breast cancer," *Current health sciences Journal*, vol. 37, no. 2, pp. 241–248, 2011.

[131] S. P. Na and D. Houserkovaa, "The role of various modalities in breast imaging," *Biomed Pap Med Fac Univ Palacky Olomouc Czech Repub*, vol. 151, no. 2, pp. 209–218, 2007.

[132] S. C. Hagness, A. Taflove, and J. E. Bridges, "Two-dimensional fdtd analysis of a pulsed microwave confocal system for breast cancer detection: Fixed-focus and antenna-array sensors," *IEEE Transactions on Biomedical Engineering*, vol. 45, no. 12, pp. 1470–1479, 1998.

[133] ——, "Three-dimensional FDTD analysis of a pulsed microwave confocal system for breast cancer detection: Design of an antenna-array element," *IEEE Transactions on Antennas and Propagation*, vol. 47, no. 5, pp. 783–791, 1999.

[134] E. C. Fear, X. Li, S. C. Hagness, and M. A. Stuchly, "Confocal microwave imaging for breast cancer detection: Localization of tumors in three dimensions," *IEEE Transactions on Biomedical Engineering*, vol. 49, no. 8, pp. 812–822, 2002.

[135] E. C. Fear and M. A. Stuchly, "Microwave detection of breast cancer," *IEEE Transactions on Microwave Theory and Techniques*, vol. 48, no. 11, pp. 1854–1863, Nov 2000.

[136] J. D. Shea, P. Kosmas, S. C. Hagness, and B. D. Van Veen, "Three-dimensional microwave imaging of realistic numerical breast phantoms via a multiple-frequency inverse scattering technique," *Medical physics*, vol. 37, no. 8, pp. 4210–4226, 2010.

[137] M. Ostadrahimi, P. Mojabi, A. Zakaria, J. LoVetri, and L. Shafai, "Enhancement of Gauss Newton inversion method for biological tissue imaging," *IEEE Transactions on Microwave Theory and Techniques*, vol. 61, no. 9, pp. 3424–3434, Sept 2013.

[138] M. Ostadrahimi, A. Zakaria, J. LoVetri, and L. Shafai, "A near-field dual polarized (TE-TM) microwave imaging system," *IEEE Transactions on Microwave Theory and Techniques*, vol. 61, no. 3, pp. 1376–1384, March 2013.

[139] P. Kosmas and C. M. Rappaport, "Time reversal with the FDTD method for microwave breast cancer detection," *IEEE Transactions on Microwave Theory and Techniques*, vol. 53, no. 7, pp. 2317–2323, July 2005.

[140] T.Rubaek, P. M. Meaney, P. Meincke, and K. D. Paulsen, "Nonlinear microwave imaging for breast-cancer screening using gauss-newtons method and the cgls inversion algorithm," *IEEE Transactions on Antennas and Propagation*, vol. 55, no. 8, pp. 2320–2331, Aug 2007.

[141] P. M. Meaney, M. W. Fanning, D. Li, S. P. Poplack, and K. D. Paulsen, "A clinical prototype for active microwave imaging of the breast," *IEEE Transactions on Microwave Theory and Techniques*, vol. 48, no. 11, pp. 1841–1853, Nov 2000.

[142] S. Y. Semenov, A. E. Bulyshev, A. E. Souvorov, A. G. Nazarov, Y. E. Sizov, R. H. Svenson, V. G. Posukh, A. Pavlovsky, P. N. Repin, and G. P. Tatsis, "Three-dimensional microwave tomography: experimental imaging of phantoms and biological objects," *IEEE Transactions on Microwave Theory and Techniques*, vol. 48, no. 6, pp. 1071–1074, Jun 2000.

[143] A. E. Bulyshev, S. Y. Semenov, A. E. Souvorov, R. H. Svenson, A. G. Nazarov, Y. E. Sizov, and G. P. Tatsis, "Computational modeling of three-dimensional microwave tomography of breast cancer," *IEEE Transactions on Biomedical Engineering*, vol. 48, no. 9, pp. 1053–1056, Sept 2001.

[144] S. Y. Semenov, A. E. Bulyshev, A. Abubakar, V. G. Posukh, Y. E. Sizov, A. E. Souvorov, P. M. van den Berg, and T. C. Williams, "Microwave-tomographic imaging of the high dielectric-contrast objects using different image-reconstruction approaches,"

IEEE Transactions on Microwave Theory and Techniques, vol. 53, no. 7, pp. 2284–2294, July 2005.

[145] E. J. Bond, X. Li, S. C. Hagness, and B. D. V. Veen, "Microwave imaging via space-time beamforming for early detection of breast cancer," *IEEE Transactions on Antennas and Propagation*, vol. 51, no. 8, pp. 1690–1705, Aug 2003.

[146] A. H. Golnabi, P. M. Meaney, and K. D. Paulsen, "Tomographic microwave imaging with incorporated prior spatial information," *IEEE Transactions on Microwave Theory and Techniques*, vol. 61, no. 5, pp. 2129–2136, May 2013.

[147] M. J. Burfeindt, T. J. Colgan, R. O. Mays, J. D. Shea, N. Behdad, B. D. Van Veen, and S. C. Hagness, "MRI-derived 3D printed breast phantom for microwave breast imaging validation," *IEEE antennas and wireless propagation letters*, vol. 11, pp. 1610–1613, 2012.

[148] V. D. Santis, J. Bourqui, and E. C. Fear, "Safety assessment of microwave breast imaging techniques: A comparison between two different approaches," in *General Assembly and Scientific Symposium, URSI*, Aug 2011, pp. 1–4.

[149] L. Apesteguía and L. J. Pina, "Ultrasound-guided core-needle biopsy of breast lesions," *Insights into imaging*, vol. 2, no. 4, pp. 493–500, 2011.

[150] M. C. Mahoney and M. S. Newell, "Breast intervention: How i do it," *Radiology*, vol. 268, no. 1, pp. 12–24, 2013, pMID: 23793589. [Online]. Available: http://dx.doi.org/10.1148/radiol.13120985

[151] D. Oloumi, K. Rambabu, and P. Boulanger, "Tracking a biopsy needle inside a breast using UWB circular-SAR," in *2015 IEEE International Symposium on Antennas and Propagation USNC/URSI National Radio Science Meeting*, July 2015, pp. 534–535.